

INFORMATION TO USERS

This manuscript has been reproduced from the microfilm master. UMI films the text directly from the original or copy submitted. Thus, some thesis and dissertation copies are in typewriter face, while others may be from any type of computer printer.

The quality of this reproduction is dependent upon the quality of the copy submitted. Broken or indistinct print, colored or poor quality illustrations and photographs, print bleedthrough, substandard margins, and improper alignment can adversely affect reproduction.

In the unlikely event that the author did not send UMI a complete manuscript and there are missing pages, these will be noted. Also, if unauthorized copyright material had to be removed, a note will indicate the deletion.

Oversize materials (e.g., maps, drawings, charts) are reproduced by sectioning the original, beginning at the upper left-hand corner and continuing from left to right in equal sections with small overlaps.

Photographs included in the original manuscript have been reproduced xerographically in this copy. Higher quality 6" x 9" black and white photographic prints are available for any photographs or illustrations appearing in this copy for an additional charge. Contact UMI directly to order.

**Bell & Howell Information and Learning
300 North Zeeb Road, Ann Arbor, MI 48106-1346 USA
800-521-0600**

UMI[®]

Measurement of electrostatic fluctuations and particle transport in an improved-confinement RFP

by

Ching-Shih Chiang

A dissertation submitted in partial fulfillment of the

requirements of the degree of

Doctor of Philosophy

(Engineering Physics)

at the

University of Wisconsin-Madison

2000

UMI Number: 9982236

**Copyright 2000 by
Chiang, Ching-Shih**

All rights reserved.

UMI[®]

UMI Microform 9982236

Copyright 2000 by Bell & Howell Information and Learning Company.

**All rights reserved. This microform edition is protected against
unauthorized copying under Title 17, United States Code.**

**Bell & Howell Information and Learning Company
300 North Zeeb Road
P.O. Box 1346
Ann Arbor, MI 48106-1346**

A dissertation entitled

Measurement of electrostatic fluctuations and particle transport in an improved-confinement RFP

submitted to the Graduate School of the
University of Wisconsin-Madison
in partial fulfillment of the requirements for the
degree of Doctor of Philosophy

by

Ching-Shih Chiang

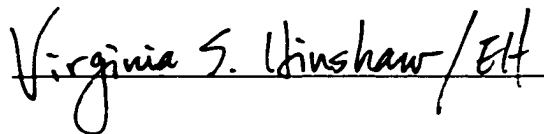
Date of Final Oral Examination: July 24th 2000

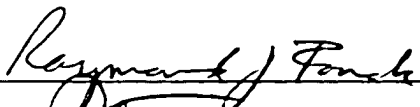
Month & Year Degree to be awarded: **December** **May** **August** 2000

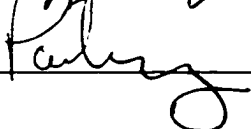
Approval Signatures of Dissertation Readers:

Signature, Dean of Graduate School









Measurement of edge electrostatic fluctuations and particle transport in the improved confinement of RFP

Ching-Shih Chiang

Under the supervision of Professor Stewart C. Prager and Dr. Gennady Fiksel
at the University of Wisconsin - Madison

Electrostatic fluctuations and particle transport have been measured in two types of improved confinement plasmas (induced by plasma biasing and pulsed poloidal current drive (PPCD)) in MST reversed-field pinch (RFP). The reduction of the electrostatic particle transport in plasma biasing is more significant than that in PPCD. The electrostatic particle transport is reduced by more than a factor of three at the entire edge region ($r/a \geq 0.90$) with plasma biasing. Significant decrease in electric field fluctuations and the correlation of density and potential fluctuations are responsible for the particle flux reduction in plasma biasing. Although shear-flow suppression induced by biasing is suggested by these features, no enhanced shearing rate is observed to support this speculation. In PPCD, particle transport decreases only at the outermost 4% of the plasmas, i.e. $r/a \geq 0.96$, even though global particle and energy confinement are significantly

improved. The electrostatic transport is not significantly impacted by current profile control. On the other hand, although significant reduction of the edge density suggests an enhanced inward motion of plasma boundary during PPCD, the reduced inward radial $E \times B$ velocity does not provide support for this speculation of plasma compression.

Acknowledgement

I am so glad that I have two kind and intelligent advisors who provide me the best assistance to pursuit the Ph.D. degree. I would like to thank my "academic" advisor in Department of Engineering Physics, Professor Raymond Fonck, who convinced me to study plasma physics in MST. Great appreciation should go to my "research" advisor, Professor Stewart Prager, who has been so patient and inspiring in physics research. I also greatly appreciate his regular availability for discussion. I also would like to express my appreciation to my prelim and thesis committee member, Professor Paul Terry, Noah Hershkowitz, Clint Sprott, and Gibert Emmert, for the useful and inspiring discussions during and before the presentation.

I have to name Gennady Fiksel for his first grade scientific mind that makes the Langmuir probe "robust" enough to collect reliable data. It is definitely impossible for me to wrap up my graduate student career without your intelligent design in probe diagnostic. Prabal Chattopadhyay, the excellent scientist whom God brought to Wisconsin from a country that is further away than ten thousand miles. Without your continuous effort and input in probe electronics and construction, I may never be able to collect the "clean " probe data. I would like to

acknowledge my mentor, Matt Stoneking and Han-Tau Ji, for their assistance about the probe hardware work and data analysis technology with IDL.

For countless experimental insight, diagnostic support, and useful discussion, thanks should go to many scientists and postdocs. These include John Sarff, Dan Den Hartog, Abdul Almagri, Miodrag Cekic, and Philip Andrew. I would like to thank Abdul Almagri for allowing me to use the biasing electrodes. These excellent electrodes never pollute plasmas.

I can not forget to mention some postdocs and my fellow graduate students, both current and previous, who have been so important in my intellectual and social life in MST, and so helpful in operating MST: Brett Chapman, James Chapman, Darren Craig, Nick Lanier, Paul Fontana, new Ph.D. Alex Hansen, Carl Sovinac, Edardo Fernandez, Jay Anderson, Ted Biewer, Neal Crocker, Art Blair, JianXin Lei, Uday Shah, Eric Spence, Johan Tabora, Derek Baver, Diane Demers, Steven Terry, and Jim Reardon. Special thanks go to Brett Chapman and Darren Craig for many inspiring discussion of improved confinement in MST, and Nick Lanier for collecting important FIR data during holiday.

I will never "overthank" the "hackers", Larry Smith and Paul Whilhite, who make the computer working and taking data everyday. Many works contributed by technical supporting staff have been so critical to make MST run more smoothly and efficiently. I would like to thank John Laufenberg, Tom Lovell, Mark

Thomas, Steve Oliva, Mikhail Reyfman, Paul Nonn, Don Holly, Dale Schutte, Kay Shatrawka, and Jean Liddicoat. I appreciate many works of the under graduate hourly, Nicos Savva, for his help in IDL code development, probe electronics installation and probe construction.

I have to say thank-you to my parents, Ming-Shiao Chiang and Chen-Pi Chiang, who have been so helpful and supporting to me in pursuing the advanced educational degree. Their unconditional love always surpasses ten thousand miles spatial separation and warms up my heart when things seem so cold and dark. Marrying to my wife Yueh-Hwa Huang is the greatest accomplishment in my graduate career and the greatest gift from God. I would like to dedicate this dissertation to her with all my heart since you participated in large part of this work. I can not forget the ceaseless prayers and encouragement of my brothers and sisters in Christ when I did not know when I am going to graduate. Your prayers have proved that our God is a living and loving God.

"And we know that God causes all things to work together for good to those who love God, to those who are called according to His purpose."

Romans 8:28

This work is supported by U.S. D.O.E.

Table of Contents

Abstract

Acknowledgements

Table of Contents

1. Introduction.....	1
1.1 Fluctuation driven transport in the RFP.....	4
<u>1.1.1 Review of transport equations.....</u>	<u>5</u>
<u>1.1.2 Review of the electrostatic fluctuations and transport</u> <u>in the RFP.....</u>	<u>7</u>
1.2 Review of the improved confinement in the RFP.....	10
<u>1.2.1 Improved confinement by current profile control.....</u>	<u>10</u>
<u>1.2.2 Improved confinement by plasma biasing.....</u>	<u>14</u>
1.3 Motivation and thesis outline.....	18
Reference.....	23
2. Experimental apparatus and diagnostics.....	25
2.1 Madison symmetric torus.....	25
2.2 Langmuir probe.....	30
<u>2.2.1 Summary of the probe sheath theory.....</u>	<u>31</u>
<u>2.2.2 Review of simple probe theory.....</u>	<u>35</u>
<u>2.2.3 Triple Langmuir probe.....</u>	<u>39</u>
<u>2.2.4 Discussion of simple probe theory.....</u>	<u>42</u>
<u>2.2.5 Error analysis of probe measurement.....</u>	<u>46</u>

2.2.6 <u>Probe design and construction</u>	50
2.3 Magnetic pickup coils.....	58
References.....	62
3. Data analysis techniques.....	63
3.1 Ensemble selection and signal processing.....	65
3.2 Review of statistical analysis.....	67
3.3 Equation of electrostatic particle transport.....	70
3.4 The wave-number frequency spectra.....	72
References.....	74
4. Electrostatic fluctuations and transport in improved confinement	
Plasmas.....	75
4.1 Measurement of electrostatic particle transport.....	78
4.2 Modenumber-frequency spectra and plasma rotation.....	89
4.2.1 <u>Modenumber-frequency spectra and plasma rotation in PPCD</u>	91
4.2.2 <u>Modenumber-frequency spectra and plasma rotation in plasma</u>	
<u>biasing</u>	97
4.3 The $m = 0, n = 1$ fluctuations induced by plasma biasing.....	104
4.4 Equilibrium profile of improved confinement.....	107
References.....	112
5. Summary and conclusion.....	113
5.1 electrostatic transport in improved confinement.....	114
5.2 mode spectra and propagation of fluctuations.....	115
5.3 Equilibrium profile.....	117

Chapter 1. Introduction

In addition to its attractiveness as a concept for the possible controlled nuclear fusion systems, the reversed field pinch (RFP) [1, 2] provides a good environment to understand the physics of turbulent plasmas. Unlike the tokamak with much stronger toroidal magnetic field than the poloidal magnetic field, the two components of the magnetic field in the RFP plasma are about the same order of magnitude. The toroidal magnetic field in the outer region is reversed with respect to the direction in the core region. Fig. 1.1 shows the profile of magnetic

field. The field line configuration in this toroidal system possesses large magnetic shear.

Understanding of the mechanisms of particle and energy loss has been a major research focus in Madison Symmetric Torus (MST) [3]. Previous measurements show that the magnetic fluctuations in MST govern particle and energy loss near the plasma core [4, 5], while in the edge of MST electrostatic fluctuations dominate the outward particle flux [6]. The mechanism of energy loss at the MST edge has not been identified. In order to achieve enhanced confinement, reducing fluctuation driven transport thus is a major goal in MST.

Improving plasma confinement has been a major program in the past a few years in MST. Two techniques have been applied to modify discharges and successfully achieved enhanced confinement. Pulsed poloidal current drive (PPCD) [7, 8] alters the current density profile and suppresses the magnetic fluctuations driven by the current density gradient. Energy and particle confinement time is improved by a factor of five and eight, respectively. The other technique to achieve enhanced confinement is plasma biasing [9]. Unlike PPCD, plasma biasing only tailors edge electrostatic fluctuations due to the localized flow induced by biased electrodes, whereas the global magnetic fluctuations remain the

same. Only modest improvement in particle confinement (50%) is accomplished, without changing energy confinement.

Although PPCD has successfully reduced core magnetic fluctuations and greatly improved the plasma confinement, how the edge electrostatic fluctuations respond to the flattened current density profile remains as a question because of the low coherence between edge electrostatic and core magnetic fluctuations. On the other hand, plasma biasing only modestly improves particle confinement. However the induced localized flow may have strong impact on the edge electrostatic fluctuations and transport [10]. Thorough understanding of improved confinement demands detailed research at the edge. In this thesis, the particle transport driven by electrostatic fluctuations is measured with electrostatic probe in both types of improved confinement. Mode-number spectra of electrostatic and magnetic fluctuations will be contrasted and different behavior is expected. The response of the equilibrium profile of plasma density, temperature, potential and parallel current due to improved confinement is also one of the major topics in this thesis.

In the following sections I review the current understanding of fluctuation driven transport in the RFP and the improved confinement achieved in MST. Motivation of this research and thesis outline will be presented in the last section.

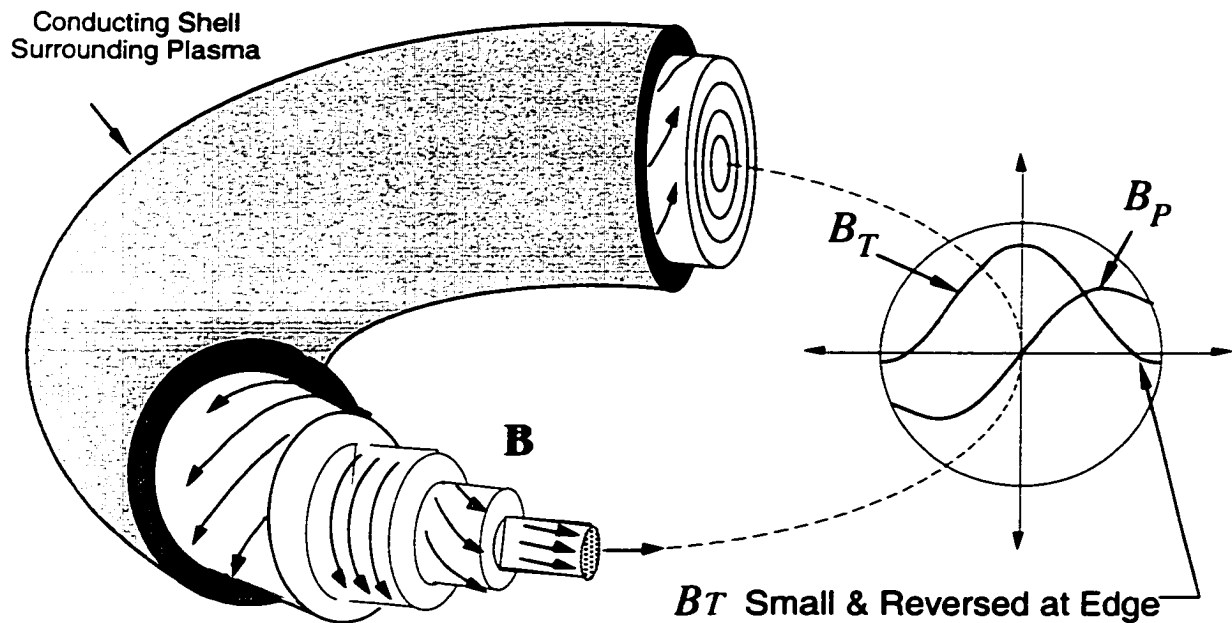


Fig. 1.1 Magnetic field configuration of reversed-field pinch

1.1 Fluctuation driven transport in the RFP

Cross-field particle and energy transport that greatly exceeds the prediction of classical diffusion theory has been observed in toroidal confinement devices, such as the reversed field pinch (RFP) and tokamak. Measurement in tokamak has shown that the total and electrostatic fluctuation driven particle flux generally

agree at the plasma edge [11, 12]. Previous measurements of Langmuir probes and electron energy analyzers in the RFP also demonstrate that the fluctuation driven transport is the most significant channel of particle and energy loss. Both particle [4] and energy [5] transport of the plasma core is governed by magnetic fluctuations, while the electrostatic fluctuations govern the particle loss in the edge [6, 13, 14]. These large outward particle and energy fluxes due to the fluctuations seriously degrade discharges and limit the improvement of plasma confinement. In this section I provide reviews of the transport equations and the previous measurement of electrostatic fluctuations and transport in the RFP.

1.1.1 Review of transport equations

Fluctuation driven transport always arises due to a correlated product of two fluctuating quantities. Suppose all quantities are represented by $x = x_0 + \bar{x}$, where x_0 is the mean value and \bar{x} is the fluctuation part. The radial particle flux due to fluctuations is given by $\Gamma = \langle \bar{n} \bar{v}_r \rangle$, where \bar{n} is the density, \bar{v}_r is radial flow velocity, and $\langle \rangle$ denotes the average over the flux surface. The amplitude of particle flux is determined by the amplitudes of fluctuations, the degree of coherence, and the relative phase relation of two fluctuating quantities, i.e.

$\Gamma = |\bar{n}|\bar{v}_r|\gamma_{nv} \cos\phi_{nv}$. Minimization of fluctuation induced transport may be accomplished with several ways, reducing either fluctuation amplitude, reducing the coherence or changing the phase relationship between the two fluctuating quantities.

The mechanisms responsible for fluctuation induced transport are roughly classified as either electrostatic or magnetic in origin [16]. If fluctuating flow velocity is driven by an $E \times B$ drift, i.e. $\bar{v}_r = \bar{E}_\perp / B_0$ where \bar{E}_\perp is the fluctuating electric field perpendicular to the local equilibrium magnetic field B_0 , then $\Gamma_{es} = \langle \bar{n}\bar{E}_\perp \rangle / B_0$ is classified as electrostatic particle transport. If the fluctuating radial flow velocity is due to parallel streaming along a radially fluctuating magnetic field, i.e. $\bar{v}_r = v_{||}\bar{B}_r / B_0$, then $\Gamma_{mag} = \langle \bar{j}_{||}\bar{B}_r \rangle / eB_0$ is classified as magnetic particle transport. In general, particle transport $\Gamma = \langle \bar{n}\bar{v}_r \rangle$ can be written as

$$\Gamma = \frac{\langle \bar{n}\bar{E}_\perp \rangle}{B_0} + \frac{\langle \bar{j}_{||}\bar{B}_r \rangle}{eB_0} \quad (1.1)$$

The first term in equation 1.1 is referred to as the electrostatic particle transport term because the electric field fluctuations induced by charge build-up (or $\bar{E}_{es} = -ik_\perp\bar{\phi}$) dominates electromagnetic E-field fluctuations at low frequency ($\bar{E}_{mag} = -\partial\bar{A}_\perp/\partial t$), and the second term is called the magnetic transport term.

1.1.2 Review of electrostatic fluctuations and transport in the RFP

Electrostatic fluctuations measured in the edge of RFP are relatively large (20% - 100%). Similar to that of tokamak, the results of $\frac{e\tilde{\phi}_{pl}}{T_{e0}} > \frac{\tilde{n}}{n_0}$ shows that the electrostatic fluctuations in RFP depart from the Boltzmann relation. The particle transport driven by electrostatic fluctuations is responsible for the total particle loss at the edge of RFP. I provide the the summary of electrostatic transport measurement of three RFP machine in this section.

1. *MST*

Electrostatic driven transport has been measured in the edge of the MST reversed-field pinch using triple Langmuir probes. Similar to the measurement in the tokamak, both the density and potential fluctuation amplitudes are large, with $\tilde{n}/n_0 \sim 30\% - 55\%$, and $e\tilde{\phi}_{pl}/T_{e0} \sim 40\% - 100\%$. Opposite to the measurement in tokamak, the temperature fluctuations in MST are relatively large, with $\tilde{T}_e/T_{e0} \sim 15\% - 40\%$ and play an important role in transport calculation. The contribution of

temperature fluctuations to the particle and energy transport thus can not be ignored.

The electrostatic fluctuation spectra are broad in both frequency and mode-number. In contrast to the power spectra of the magnetic fluctuations, the fluctuation power in electrostatic fluctuations monotonically decrease with frequency. No apparent peak at any particular frequency is observed. The mode number spectra are centered at toroidal mode number $n \sim 0$, instead of $n \sim 6$ of magnetic fluctuations.

The spectrum of particle transport is broad and no apparent peak at any frequency is observed. In the edge of MST ($r / a \geq 0.9$), the measured electrostatic fluctuation radial particle flux limits the particle confinement time to ~ 1 ms, which is comparable to the total particle confinement time. In contrast, the electrostatic energy transport contributes only $\sim 20\%$ to the observed global energy transport. In the interior region (inside the reversal surface), the particle flux driven by magnetic fluctuations dominates the flux driven by the electrostatic fluctuations and determines the global particle and energy confinement.

2. *REPUTE-1*

REPUTE-1 is a relatively smaller RFP, with major radius $R = 82$ cm, minor radius $a = 22$ cm, relatively low plasma current $I_p \sim 110$ kA and higher electron density $n_0 \sim 4.4 \times 10^{13} \text{ cm}^{-3}$, compared with MST. The measurement of electrostatic fluctuations and transport are qualitatively consistent with those of MST, with large normalized fluctuation levels, $\bar{n}/n \sim 20\% - 40\%$, $\bar{T}_e/T_{e0} \sim 15\% - 35\%$, and $e\bar{\phi}_{pl}/T_{e0} \sim 50\% - 100\%$, large electrostatic particle and small energy transport driven by the electrostatic fluctuations at the edge of REPUTE-1. However the electrostatic fluctuation driven particle transport can only account for 50% of the estimated total particle loss.

3. ZT-40M

ZT-40M is a toroidal RFP device with major radius $R = 1.14$ m, minor radius $a = 0.20$ m, plasma current $I_p \sim 120$ kA, and line average electron density $n_e \sim 1.3 \times 10^{13} \text{ cm}^{-3}$. Electrostatic fluctuations and transport have been measured in the edge. The normalized fluctuation levels are large, with $\bar{n}/n_0 \sim 40\%$, $e\bar{\phi}_{pl}/T_{e0} \sim 80\%$, and $\bar{T}_e/T_{e0} \sim 40\%$, where the electron motion does not satisfy the Boltzmann relation. They have broadband spectra, a reflection of their turbulent characteristics.

The measured particle flux induced by electrostatic fluctuations at the edge of ZT-40M is comparable to that obtained from the global confinement estimate. The associated electron energy flux, however, is less than 20% of the total energy flux. The loss of hot electrons thus becomes the most probable candidate for edge energy transport. These results described above bear similarities to those obtained in MST. There are two results in apparent contrast to those of MST. (1) Coherence between the electrostatic and magnetic fluctuations is found to be relatively high in ZT-40M, particularly at frequency lower than 50kHz (~ 70%), where the global MHD activities are strongest. (2) The contribution of the electrostatic particle flux from the frequency lower than 50 kHz is larger than that from high frequency.

1.2 Review of improved confinement

1.2.1 Improved confinement by Current profile control

As mentioned above, magnetic fluctuations are responsible for the particle loss near the core of the MST and their origin is better understood than that of electrostatic fluctuations. The reduction of magnetic transport becomes the primary focus of experimental and theoretical work with the goal of reducing the outward particle and heat fluxes and improving the plasma confinement. The

dominant magnetic fluctuations resonant inside the reversal surface (poloidal mode number $m = 1$, $n = 6 \sim 9$) in the RFP are driven by the gradient in parallel current density $\mu = \mu_0 J \cdot B / B^2$. A solution for reducing magnetic fluctuations is current density profile control. In MST the current profile is transiently altered with a series of five poloidal electric field pulses during the peak of plasma current (a technique referred as pulsed poloidal current drive, PPCD). The PPCD discharge is optimized by independently programming the trigger times as well as the voltage setup of 5 stages of capacitor banks, as shown in Fig. 1.2.

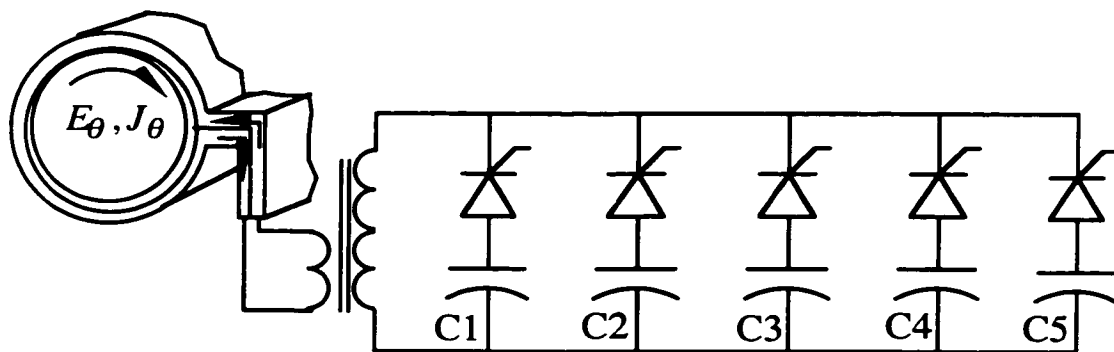


Figure 1.2 – The PPCD circuit. Current driven in the shell changes the toroidal magnetic field, thereby producing a poloidal electric field that works to flatten the edge parallel current density gradient.

Fig. 1.3 shows several global parameters of a typical PPCD discharge. The externally applied pulses of poloidal electric field during application of PPCD are clearly seen in Fig. 1.3 (a). Increased line-averaged electron density and reduced H_α emission during PPCD, shown in Figs. 1.3 (b), and 1.3 (c), is a good indication of enhanced confinement. The scenario is summarized as follows. An obvious increase in external parallel electric field is able to match parallel current $\eta j_{||}$, whereas the need of the dynamo fluctuations to balance the parallel ohm's law ($j_{||} = \sigma(E_{||} + \tilde{v} \times \tilde{B})$) may be obviated. The obviation of the dynamo electric field results in the reduction of magnetic fluctuations (Fig. 1.3 (d)). The suppressed transport and improved confinement then may be achieved due to the reduced magnetic fluctuations. With measurement of electron temperature and density profile, and ohmic input power estimated with modeling of magnetic field profile, a fivefold increase of the energy confinement time has been achieved [8]. The particle confinement time is increased by a factor of 8 as inferred from the profile measurement of the electron density and H_α emission [15].

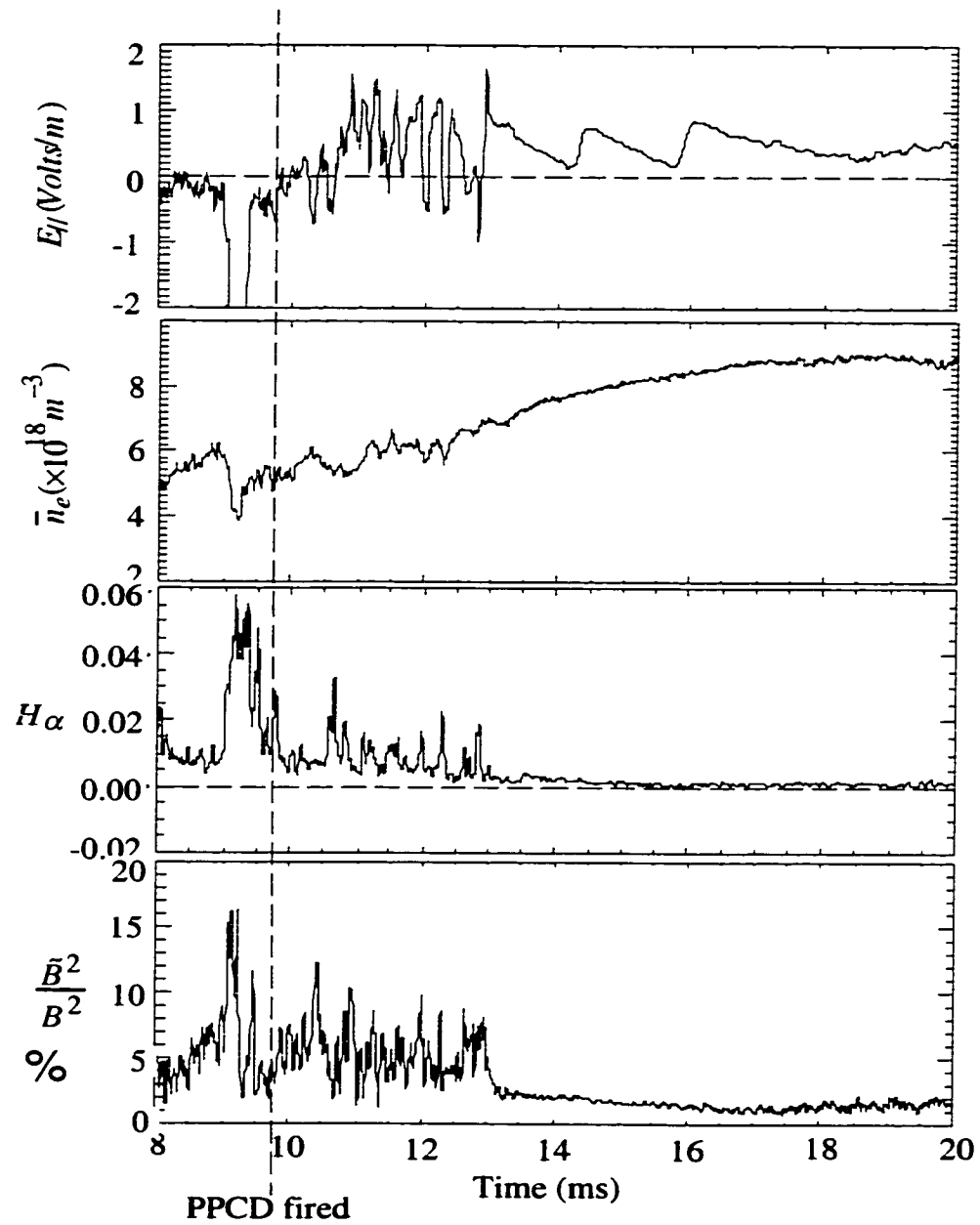


Fig. 1.3 Typical discharge wave form of PPCD (a) Parallel electric field, (b) line-averaged density, (3) line-averaged H_{α} radiation, (4) normalized magnetic fluctuation

1.2.2 Improved confinement by plasma biasing

Measurement in many magnetically confined plasma devices has shown that the gradient in electric field is able to reduce the transport driven by electrostatic fluctuations [17, 18]. A sheared radial electric field may be imposed in the edge with inserted electrodes. Enhanced confinement referred to as bias-induced H-mode in tokamaks and stellarators is triggered when the bias electrodes drive the radial electrical current greater than a critical value. The electrostatic fluctuations dominate the turbulence and transport in these cases. A strong $J \times B$ force can induce shear flow that then tailors the electrostatic fluctuations and changes the phase relations between fluctuations. This results in great improvement of particle and energy confinement.

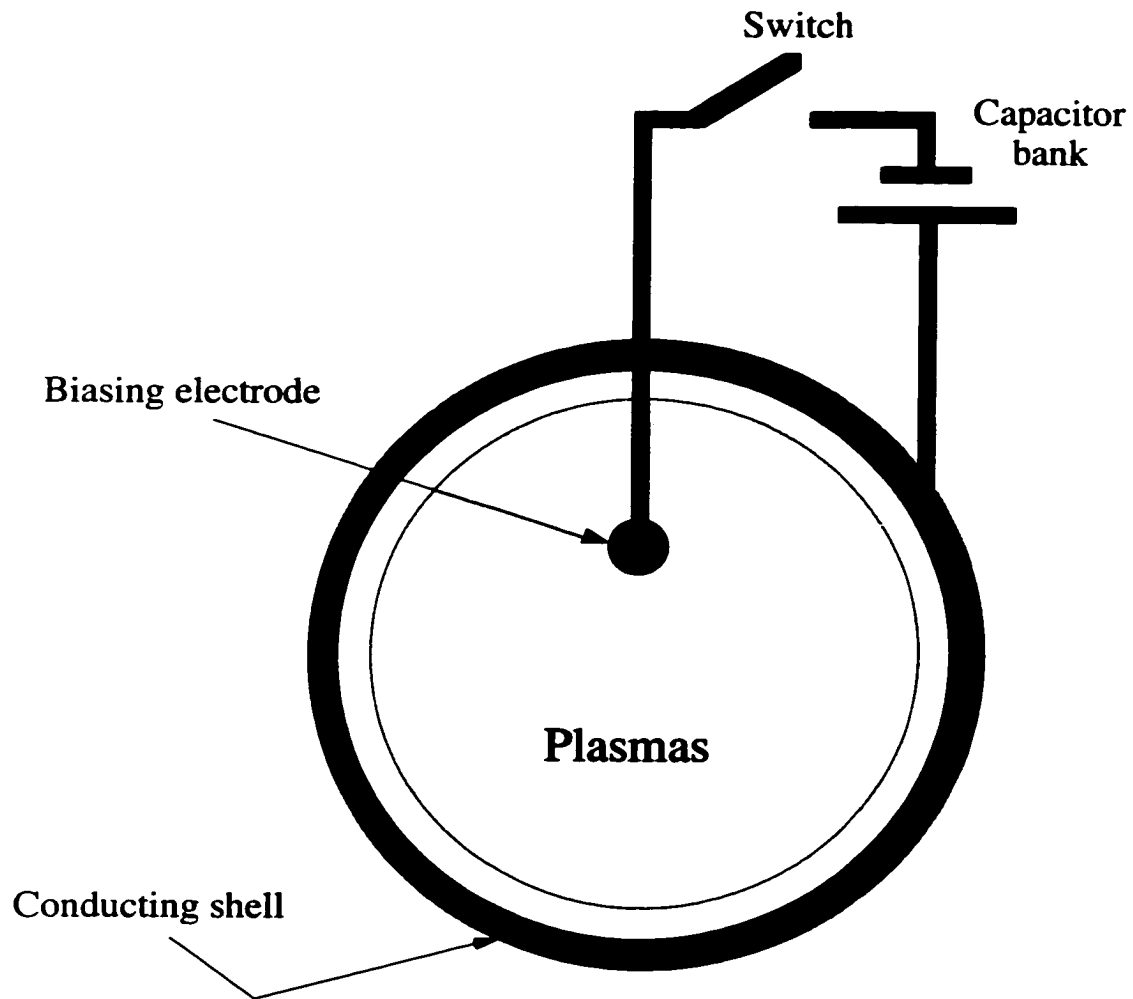


Fig. 1.4 Simplified circuit schematics of plasma biasing

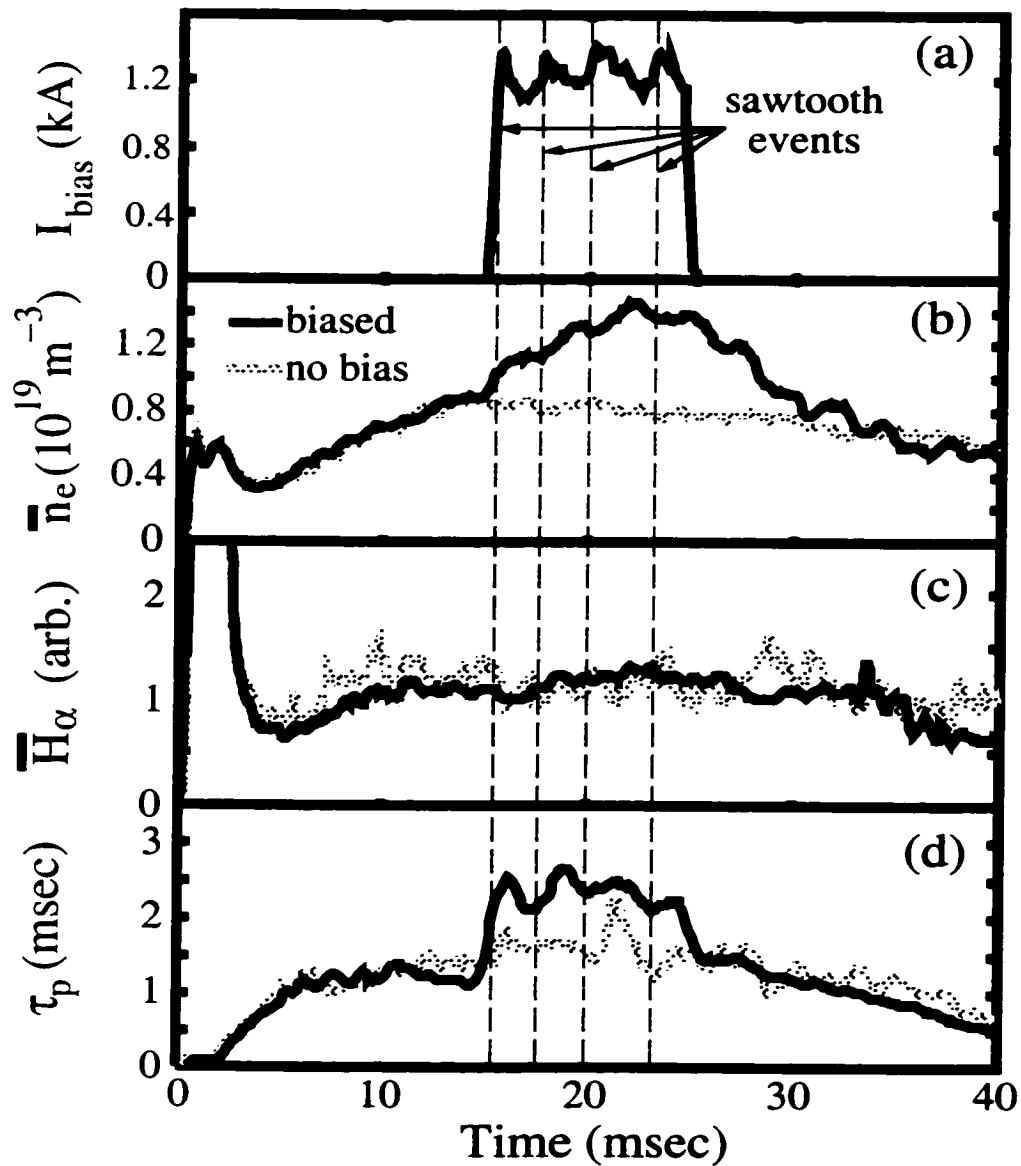


Fig. 1.5 Typical discharge waveform of plasma biasing (a) Biasing current, (b) line-averaged density, (c) line-averaged H_α radiation, and (4) particle confinement time

Unlike the cases in some tokamaks, experiments of edge plasma biasing in the reversed field pinch show improved particle confinement, but energy confinement remains the same. This difference may come from the fact that electrostatic fluctuations in RFP may only induce particle transport in the edge. The mechanism underlying the energy transport in the edge has not been established. The inserted electrodes in MST emit about 1 kA of radial electrical current at -400 bias voltage. The biasing is activated during the flattop of plasma current (15 - 25 ms). Fig. 1.5 shows global parameters of one typical discharge of plasma biasing in MST. The global particle confinement time (Fig. 1.5 (d)) increases by 50% due to the 50% increase of line-averaged density and although there is no change in the line-averaged H_α radiation. Fluctuation amplitudes in floating potential is shown in Fig. 1.6. Reduction of potential fluctuation due to plasma biasing is observed all over the edge plasmas.

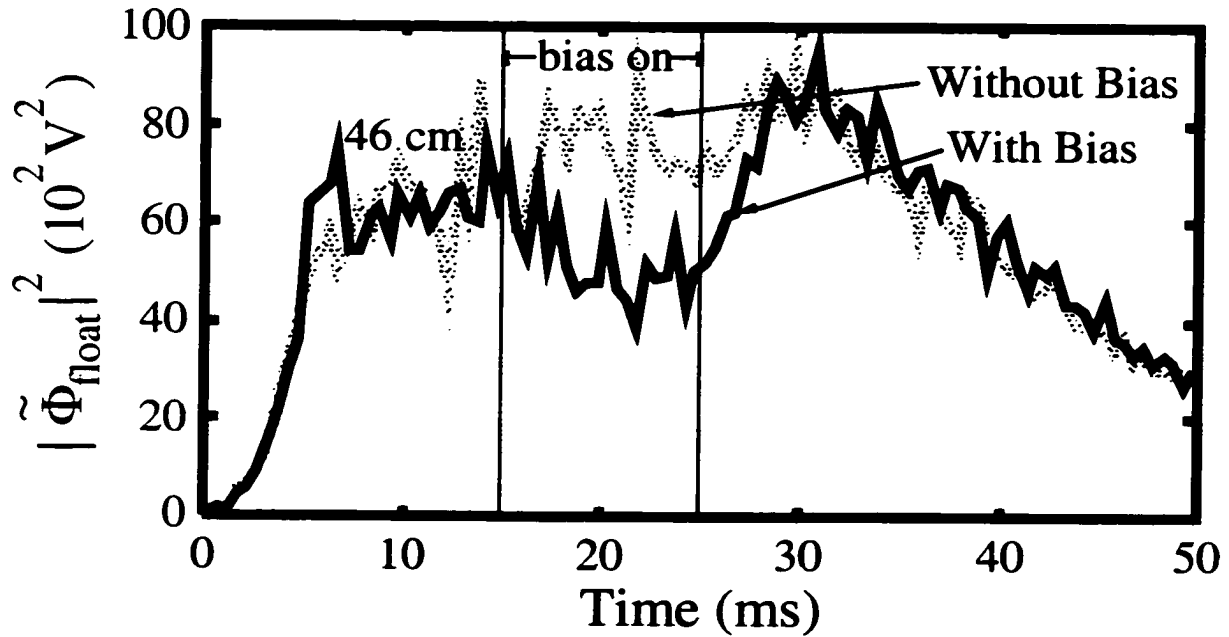


Fig. 1.6 Measured floating potential fluctuation power vs. time

1.3 Motivation and Thesis outline

Although the improved confinement times of PPCD and plasma biasing are estimated with several line-averaged diagnostics and modeling of profile, and the reduced transport has been proclaimed in these discharges, direct measurement of the electrostatic transport has never been reported. Careful edge measurements with probes are critical for more insight about the improved confinement of MST. In this thesis, several edge diagnostics are used to collect the data of equilibrium

and fluctuation quantities. We use triple Langmuir probes (TLP) to collect the data of plasma density, electron temperature, plasma potential and wavenumber of electrostatic fluctuations. Fluctuation induced particle transport is the primary quantity we would like to estimate from these data. Several factors contributing to the change of transport due to the improved confinement will be examined carefully. Assuming particle flux follows Fick's law, changes of diffusion coefficient due to PPCD and plasma biasing can be estimated with measured edge equilibrium density and particle flux profile. With the measurement of plasma potential profile, changes in phase velocity may be compared with changes in radial electric field that induces $E \times B$ drift. The toroidal magnetic coil array is used to obtain mode spectrum of magnetic fluctuations. Comparison of this with electrostatic fluctuation will be presented. The synopsis of the results are:

For plasma biasing:

- The electrostatic particle transport is reduced by a factor of larger than three at the entire edge region ($r/a \geq 0.90$) with plasma biasing.
- Significant decrease in electric field fluctuations and the correlation of density and potential fluctuations are responsible for the particle flux reduction in plasma biasing.
- No enhanced shearing rate is observed to support shear-flow suppression induced by biasing.

For PPCD:

- Particle transport decreases only at the outermost 4% of the plasmas, i.e. $r/a \geq 0.96$, even though global confinement are significantly improved.
- The electrostatic transport is not significantly impacted by current profile control.
- Significant reduction of the edge density and particle transport is not the result of an enhanced $E \times B$ inward motion of plasma boundary since the inward radial $E \times B$ velocity is reduced during PPCD.

In chapter II, I describe the experimental methods, including an overview of the MST machine and several diagnostics. The characteristics of the MST design and operational parameters will be given. Triple Langmuir probes are the diagnostics for measurement of particle transport driven by electrostatic fluctuations. Details in design and error analysis will be presented. Magnetic pickup coils and toroidal array are important to identify the similarity and difference between electrostatic and magnetic fluctuations. Magnetic pickup coils of three components are installed in the electrostatic probe for local coherence measurement of fluctuations in electrostatic and magnetic fields. Data of a toroidal array provides real time mode information by spatial Fourier decomposition. For example phase velocity of the dominating magnetic mode is an important phenomena to assure plasma rotation during the machine operation. On the other

hand, mode-number spectrum can be provided by data of coil array using 2-point method. Coil design and calibration will be discussed in this section.

Chapter III covers the fundamentals of Fourier spectrum analysis. Several key points to obtain reliable discrete data analysis will be discussed. I also present the algebra of calculating fluctuation power spectra, coherence, phase relation of two signals, wavenumber spectra, including two-point method with which the fluctuation mode spectrum can be derived. The fluctuation and transport results will be presented in chapter IV. In plasma biasing, the significant reductions of the potential fluctuations, wavenumber, and the phase between \tilde{n} and $\tilde{\phi}_{pl}$ are combined to significantly reduce the electrostatic particle flux at least by a factor of 3. On the other hand, the impact to the electrostatic particle transport due to the current profile control is only minor. The increase and decrease in diffusion coefficient derived with the Fick's law shows the consistent increase in PPCD and decrease in plasma biasing, which shows the qualitative consistency with the particle flux measurement. I discuss the change of the fluctuation propagation with the change of the equilibrium plasma potential profile, the mode number spectra, and the plasma flow measurement. In PPCD, there is no significant alteration about the global mode rotation and plasma flow, while the propagation of the edge electrostatic fluctuation is slowed down and remains in the same direction. In plasma biasing, both the global mode rotation and plasma flow are reversed. The

phase velocity of the edge electrostatic fluctuations and edge plasma flow which move in the opposite direction than the global plasmas are accelerated due to the imposed radial electric field. In Chapter V are a brief thesis summary, and some concluding remarks.

References

- H. A. Bodin and A. A. Newton, *Nuclear Fusion*, **19**, 1255 (1980)
- S. Ortolani and D. D. Schnack, *Magnetohydrodynamics of plasma relaxation*, World Scientific Publishing Co., Singapore (1993)
- R. N. Dexter *et al.*, *Fusion Technol.* **19**, 131 (1991)
- M. R. Stoneking *et al.*, *Phys. Rev. Lett.* **73**, 549 (1994)
- G. Fiksel, S. C. Prager, W. Shen, and M. Stoneking, *Phys. Rev. Lett.* **72**, 1028 (1994)
- T. D. Rempel *et al.*, *Phys. Rev. Lett.* **67**, 1438 (1991)
- J. S. Sarff, *et al.*, *Phys. Rev. Lett.*, **72**, 3670 (1994)
- M. R. Stoneknig *et al.*, *Phys. Plasmas* **4**, 1632 (1997)
- D. Craig *et al.*, *Phys. Rev. Lett.* **79**, 1865 (1997)
- V. Antoni, *Plasma Phys. Control. Fusion* **42**, 83 (2000)
- J. Wooton *et al.*, *Phys. Fluids* **B2**, 2879 (1990)
- W. L. Rowan *et al.*, *Nucl. Fusion* **27**, 1105 (1987)
- H. Ji, Toyama, K. Miyamoto, S. Shinohara, and A. Fujisawa, *Phys. Rev. Lett.* **67**, 62 (1991)
- H. Tsui *et al.*, *Nucl. Fusion*. **31**, 2371 (1991)

- N. Lanier, Ph.D. thesis, University of Wisconsin - Madison (2000)
- P. C. Liewer, *Nucl. Fusion* **25**, 543 (1985)
- R. J. Taylor, *et al.*, *Phys. Rev. Lett.* **63**, 2365 (1989)
- R. A. Moyer, *et al.*, *Phys. Plasmas* **2**, 2397 (1995)

Chapter II. Experimental apparatus and diagnostics

2.1 Madison Symmetric Torus

MST is a large toroidal device with circular poloidal cross section, major radius $R=1.5$ m, minor radius $a=0.52$ m, and maximum plasma current $I_p < 500$ kA, electron density $N_e < 2.0 \times 10^{13} \text{ cm}^{-3}$. Interested readers should refer to reference 1 for details of design and operation of MST. The vacuum vessel (VCV) of MST is made from 5cm thick aluminum. This aluminum shell serves as a stabilizing

conducting shell and close-fitting single winding of toroidal magnetic field. The VCV has two (1 poloidal, 1 toroidal) gaps to allow the magnetic fields to penetrate into the shell from the external circuit. They are individually insulated vertical and horizontal cut in the conducting shell. Two advantages are seen in this VCV design: (1) The ripples due to the multiple windings can be minimized. (2) Easier access for diagnostics is provided.

In order to minimize plasma-wall interaction and particle loss due to streaming out along the field, several feature in MST are designed to reduce the field error associated with portholes. (1) The VCV contains about 200 holes with $\sim 1 \frac{1}{2}$ inches in diameter for vacuum pumping. Field errors due to evacuating portholes may be minimized with multiple small holes compared with single large hole. (2) Most portholes (~ 175) for diagnostics access are $1 \frac{1}{2}$ inches diameter. Only four of them are $4 \frac{1}{2}$ inches. Diagnostics larger than this may cause unwanted large field errors.

Field errors in poloidal gap have been shown to cease rotation of magnetic fluctuations, grow to large amplitudes, then adversely affect plasma confinement. Great effort for measurement and reduction of field errors has been concerned and proposed. Control of field error in the poloidal gap is carried out by various sets of field error correction coils installed at this gap [2]. Optimized operation of these

coils either successfully eliminates growth of large field errors, or at least delays the onset of mode locking until late in discharge. Under this condition, field errors do not dominate the mechanism of plasma loss. The premature termination of plasmas is also greatly reduced

In addition to control of field error, plasma-wall interaction can be reduced by pulsed discharge cleaning (PDC). When the machine is not operated for RFP, this system runs unattended automatically so that the plasma-facing wall may be carefully conditioned. Table 1.1 shows some basic design and operational parameters of MST. Two side views of MST are shown in Fig. 2.1.

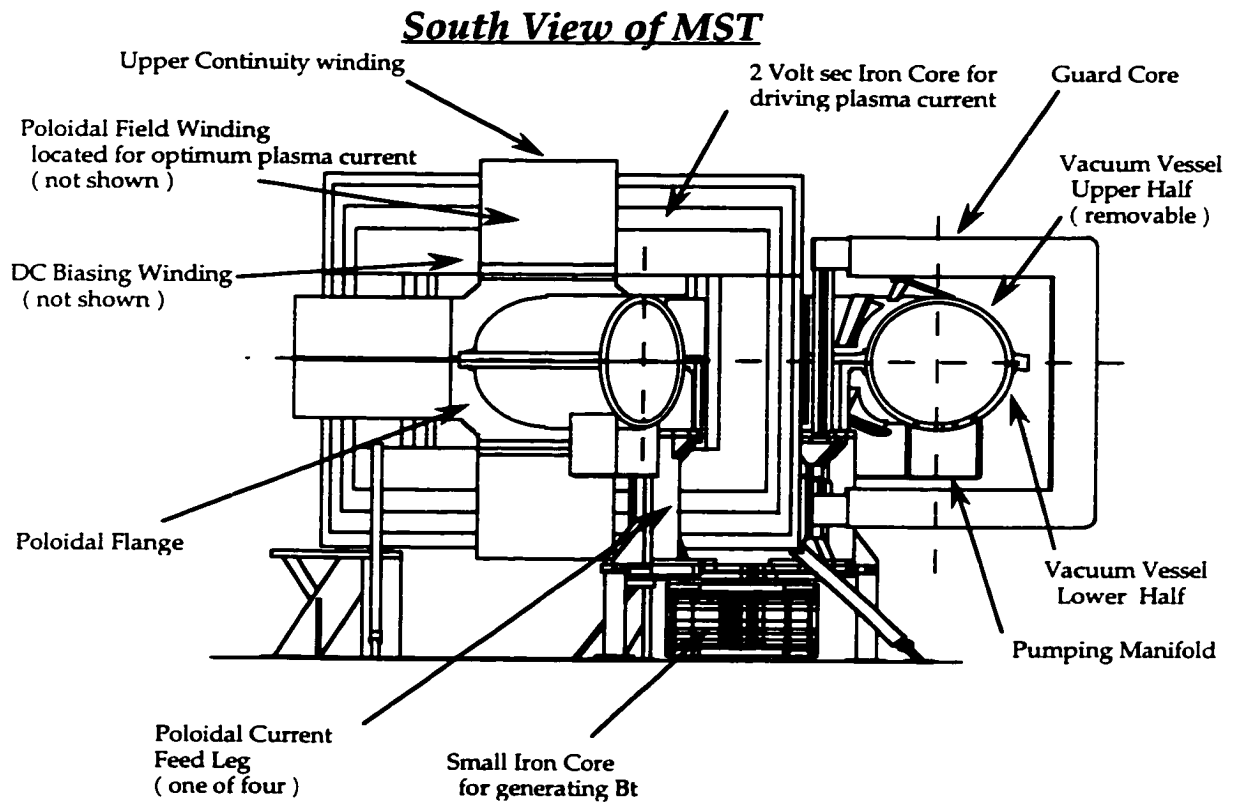


Fig. 2.1 South view of Madison Symmetric Torus

Table 1.1 MST parameters

Major radius	150 cm
Minor radius	52 cm
Wall thickness	5 cm
Plasma current	< 500 kA
Loop voltage	5 ~ 15 volts
Electron temperature	< 800 eV
Line-averaged density	< $2 \times 10^{13} \text{ cm}^{-3}$
Particle confinement time	1 ~ 8 ms
Energy confinement time	1 ~ 6 ms

2.2 Langmuir probe

An apparently simple structure and good spatial resolution have made Langmuir probe [3] extensively used as diagnostics of several plasma parameters. Although it is hard for Langmuir probes to survive in high temperature plasmas, they are still attractive diagnostics in the edge of fusion devices. Close relation between edge and core plasma behavior has made the prospects bright for continued use of such probes in fusion devices. Langmuir probe is nothing but a piece of conductor immersed in plasma, coupled with voltage power supply and resistors so that the measured electrical current is a function of bias voltage. Analysis of the current-voltage curve provides estimation of plasma density, electron temperature and plasma potential. In the following sections, I first summarize simple probe theory, including the sheath concept, I-V characteristics of single probe, and how plasma parameters are estimated by the I-V curve. Then double probe and triple probe methods that meet the request of measuring density and temperature fluctuations simultaneously in turbulent plasmas will be discussed. Thirdly several correction factors that do not exist in simple probe theory in different experimental conditions will be reviewed. I will discuss the measurement errors that arise from these corrections needed in MST.

2.2.1 Summary of the probe sheath theory

When a probe is immersed in plasmas, electrons, being more mobile, tend to flow to the probe much faster than ions. A strong electric field is then built up in order to balance the particle flux of these two species over a small region surrounding the probe. This strongly perturbed region is called the sheath. The relation between the space potential and the charge particle density in the sheath region can be expressed with the Poisson equation,

$$\nabla^2 \phi = \frac{-e}{\epsilon_0} (n_i - n_e) \quad 2.1$$

Assuming Boltzmann electrons $n_e = n_\infty \exp(e\phi/T_e)$ and $n_i \approx n_\infty$, with the condition $e\phi \ll T_e$, we are able to approximate $\exp(e\phi/T_e)$ by $1 + e\phi/T_e$ and rewrite the Poisson equation as,

$$\nabla^2 \phi = \frac{1}{\lambda_d^2} \phi ,$$

where

$$\lambda_d = \left(\epsilon_0 T_e / n_e e^2 \right)^{1/2} ,$$

is called the Debye length. The thickness of the sheath region is usually of the order of a few Debye lengths. In most fusion devices with large electron density, the Debye length is usually much smaller than the probe device dimensions. Thus the potential perturbation induced by the probe in the bulk plasmas can be well neglected.

Sheath thickness can be determined by solving Poisson's equation. In order to obtain a meaningful solution of potential in the sheath region, i.e. one in which potential drops monotonically across the probe sheath, ions must enter the sheath with a minimum velocity, i.e ion sound velocity. A presheath region with a potential drop $\Phi_{pre} = -T_e/2e$ exists outside the sheath where the quasineutrality holds, but a weak electric field is then required to accelerate the ions to reach the ion sound velocity. Assuming the case of low ion temperature ($T_i \ll T_e$), the ion sound velocity is determined by electron temperature, $v_s = (T_e/m_i)^{1/2}$. This is well known as the Bohm (or sheath) criterion. For details of the derivation of the Bohm sheath criterion, the interested readers should refer to reference 4 or 7.

Assuming the ion flux is constant through the sheath, the potential drop $\Delta\Phi$ between the sheath edge and the probe may be derived by balancing the electron and ion flux at the probe surface:

$$\frac{1}{4} n_e \bar{v}_e = n_i v_s ,$$

where the electron density $n_e = n_\infty \exp(\Delta\Phi/T_e)$, $n_i = n_\infty$ is the ion density at the sheath edge, $\bar{v}_e = (8eT_e/\pi m_e)^{1/2}$ is the mean electron speed, and $v_s = (T_e/m_i)^{1/2}$ is the ion sound velocity. Solving Eq. 2.1, we obtain

$$\Delta\Phi = -T_e \ln(m_i/2\pi m_e)^{1/2} ,$$

In hydrogen plasmas, $\Delta\Phi \sim -2.8T_e$.

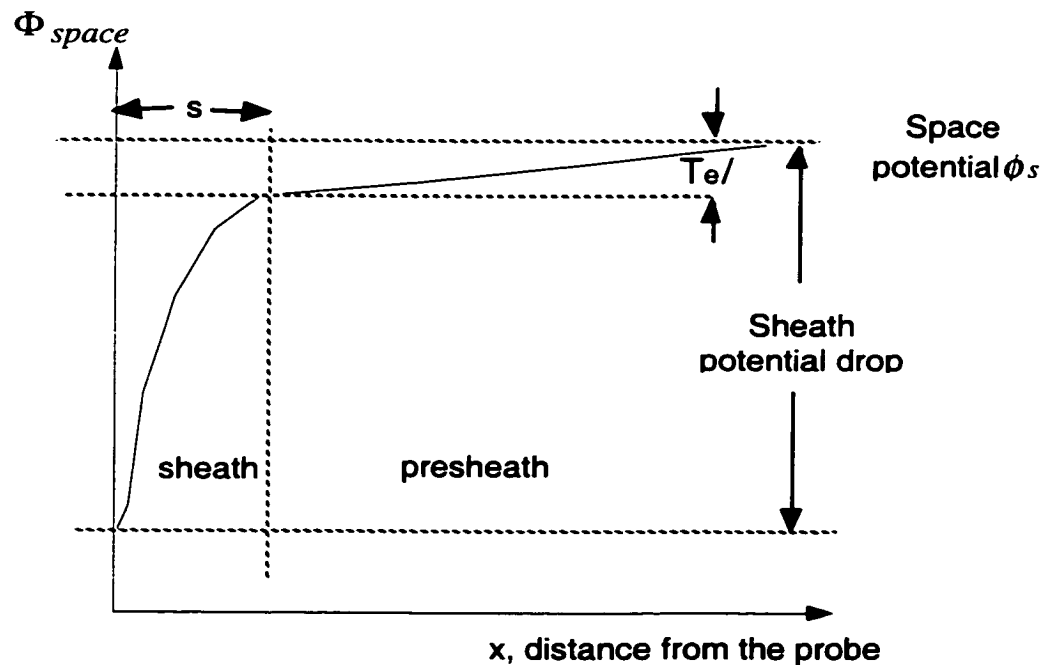


Fig. 2.2 Illustration of potential perturbation caused by a probe

Figure 2.2 shows the qualitative behavior of the sheath and presheath surrounding the probe. If a large negative bias is applied to the probe, neglecting the electron density in the sheath becomes a reasonable assumption (because $n_e \sim n_\infty \exp(e\phi/T_e) \rightarrow 0$ when ϕ is a large negative value and $|e\phi| \gg T_e$). The potential in the sheath as a function of the distance from the probe at large negative bias can then be determined by integrating the Poisson's equation, assuming electron density is negligible. If we define s as the distance where the sheath potential is equal to the space potential, and Φ_b as the probe bias voltage, the integrated Poisson equation may provide the approximate relationship between s and Φ_b as [4]

$$s = \lambda_d (\Phi_b / T_e)^{3/4} \quad 2.2$$

where s is equivalent to the sheath thickness. So the sheath thickness usually increases with the probe bias voltage. For typical operation of the triple Langmuir probe in MST discussed later, the probe bias voltage $\Phi_b \approx 4T_e$, which means that the probe sheath thickness is of the order of a few Debye lengths. Except in the condition of very large bias of the probe, probe sheath thickness is usually neglected compared with the probe or device dimension for fusion plasmas.

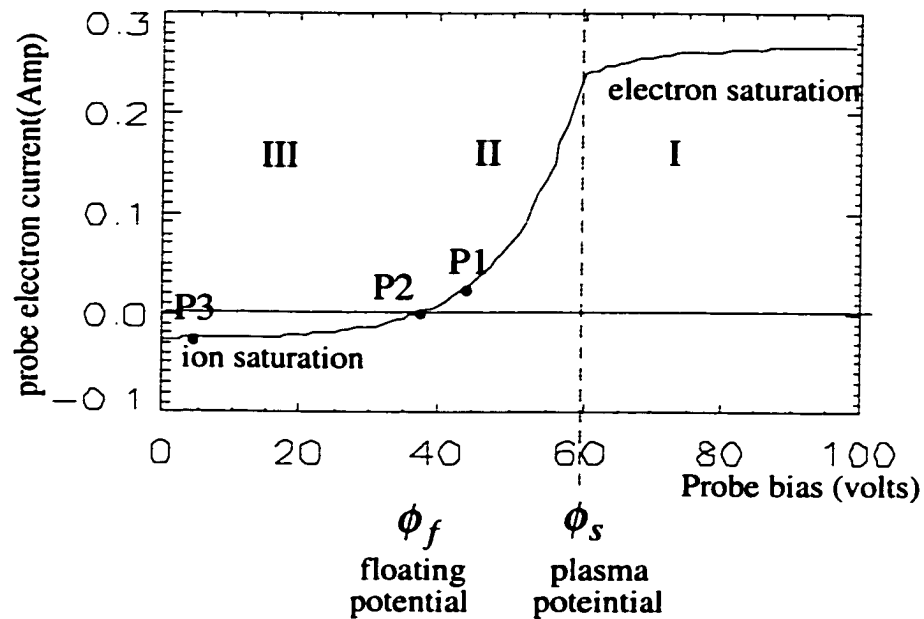


Fig. 2.3 I-V characteristics of single Langmuir probe: electron current versus bias voltage

2.2.2 Review of simple probe theory

If the probe is biased with respect to ground, probe current as a function of bias voltage may be obtained by going through the following discussion.

The electrical current is generally expressed as $I = qnAv$, where q is the particle charge, n is particle density, A is particle collecting area, and v is particle velocity. For electron saturation, the particle velocity is given by the average velocity of the Maxwellian electron distribution, i.e. $v_e = (1/4)\sqrt{8T_e/\pi m_e}$. In the case of low ion temperature ($T_i \ll T_e$), ion velocity used for ion saturation current

must satisfy the Bohm criterion, i.e. $v_i = \sqrt{T_e/m_i}$ at the sheath edge. Assuming Boltzmann electrons, the current-voltage equations of a single probe may be expressed as:

$$I_- = enA_- \sqrt{T_e/2\pi m_e} \quad 2.3$$

$$I_+ = \exp(-1/2) enA_+ \sqrt{T_e/m_i} \quad 2.4$$

$$I = \begin{cases} -I_- \exp\left(\frac{\phi_B - \phi_s}{T_e}\right) + I_+, & \phi_B < \phi_s \\ -I_-, & \phi_B > \phi_s \end{cases} \quad 2.5$$

The meanings of symbols are listed below:

- I_- is electron saturation current
- I_+ is ion saturation current
- A_- is electron probe area
- A_+ is ion probe area
- ϕ_s is plasma potential
- ϕ_B is probe Bias potential
- T_e is electron and ion temperature
- m_e, m_i are electron and ion mass

The $\exp(-1/2) \sim 0.61$ in ion saturation is due to the Bohm criterion that requires the existence of the presheath. The current collecting area of electrons and ions A_-, A_+ may change in magnetized plasmas, depending on the magnitudes of magnetic field. Discussion about this will be presented later.

Figure 2.3 shows the I-V curve based upon the Eq. 2.5. Notice that no zero is indicated on voltage axis because initially the plasma potential with respect to the vacuum vessel is still unknown. Electron saturation is located in region (I) where V_{bias} is larger than plasma potential ϕ_s . At this region large positive probe potential attracts all electrons and repels all ions, assuming low ion temperature. Probe current is only carried by electrons. Further increase in bias voltage simply adds kinetic energy to electrons, but does not increase the current drawn. Thus region I is called electron saturation. When the probe bias voltage decreases, the probe enters region II where the lower probe potential starts to repel electrons and attract ions.

The electron current decreases exponentially with decrease of probe potential in case of the Boltzmann electrons. When the probe potential approaches the floating potential ϕ_f , the electron current is reduced to a small fraction of its saturation value. At floating potential, the net probe current is zero because ion current is equal to electron current. Decreasing the potential further, entering region III, only ions are collected at constant rate. This is ion-saturation current.

Once the probe I-V current is obtained from experiment, one can calculate several important plasma parameters. The electron temperature is related to

derivative of logarithm of probe current with respect to bias potential in region II of the I-V curve:

$$T_e = (I - I_+) / \left(\frac{d \ln I}{d \phi_B} \right) \quad 2.6$$

Using the equation of the ion saturation with the electron temperature estimated from above, we are able to obtain the plasma density:

$$n_e = \frac{\exp(1/2) I_+}{A_+ e} \sqrt{\frac{m_i}{T_e}} \quad 2.7$$

When ϕ_B is equal to the floating potential ϕ_f , no net current is drawn, i.e. the ion saturation current I_+ is equal to the electron current $I_- \exp((\phi_B - \phi_s)/T_e)$. Without magnetic field, the areas of electron and ion collection are the same ($A_+ = A_-$).

This will provide the very useful relation:

$$\phi_f = \phi_s - \alpha T_e \quad 2.8$$

$$\alpha = \frac{1}{2} \left[1 - \ln \left(\frac{2\pi m_e}{m_i} \right) \right] \quad 2.9$$

For hydrogen plasmas, $\alpha \sim 3.3$.

2.2.3 Triple Langmuir probe

The theory described so far is for single probe that is biased with respect to ground. The technique of single probe has several disadvantages. (1) The voltage sweep is required to obtain the probe characteristic curve. This requirement limits the time resolution of measurement and makes them difficult to be used in time-varying plasmas. (2) Curve fitting is required to derive the plasma parameters. Real time measurement during experiment becomes less possible because fitting the I-V curve is time consuming. (3) In magnetized plasmas, electron saturation may deplete the electrons in the flux tube of magnetic field due to low cross-field electron diffusion, i.e. $D_{\parallel} \gg D_{\perp}$. This varies the probe I-V characteristics, making the interpretation of simple probe theory difficult.

Technique of triple Langmuir probe has been proposed to overcome these disadvantages of single Langmuir probe [5, 6]. I briefly review the fundamentals in this section. Three conductors are used simultaneously with fixed biased voltage on each of them. We assume that the same probe characteristic curve is applied to all probe tips. Two of them are biased with respect to each other, but are insulated from ground. The net current flowing through this pair of probes is zero because the system remains floating with the plasma. The current collected with the

negative biased probe is compensated by that collected with the other probe biased positively.

The third conductor is left floating to measure floating potential. Fig. 2.4 demonstrates the simplified triple-probe circuit and electric potential of each probe. Probes P1, P2, and P3 are inserted in to the plasma. As described above, P1 and P3 are biased with respect to each other with voltage ϕ_{d3} , while P2 is floating. The potential location in the I-V curve of each probe is shown in Fig. 2.4. Current flowing through P1 and P3, measured with a small resistor is I_1 . Voltage between P1 and P2, measured with a resistor large compared with plasma impedance, is ϕ_{d2} . The plasma potential is ϕ_s , and the floating potential is ϕ_f . Let ϕ_1 , ϕ_2 , and ϕ_3 represent the potential difference from the plasma potential ϕ_s in P1, P2, and P3. Then we have ϕ_{d2} and ϕ_{d3} defined as follows,

$$\begin{aligned} \phi_{d2} &= \phi_2 - \phi_1 \\ \phi_{d3} &= \phi_3 - \phi_1 \end{aligned} \quad , \quad 2.11$$

Writing the current-voltage equations of each probe, we have

$$\begin{aligned} -I_1 &= -I_- \exp(-\phi_1/T_e) + I_+ \\ 0 &= -I_- \exp(-\phi_2/T_e) + I_+ \\ I_1 &= -I_- \exp(-\phi_3/T_e) + I_+ \end{aligned} \quad , \quad 2.12$$

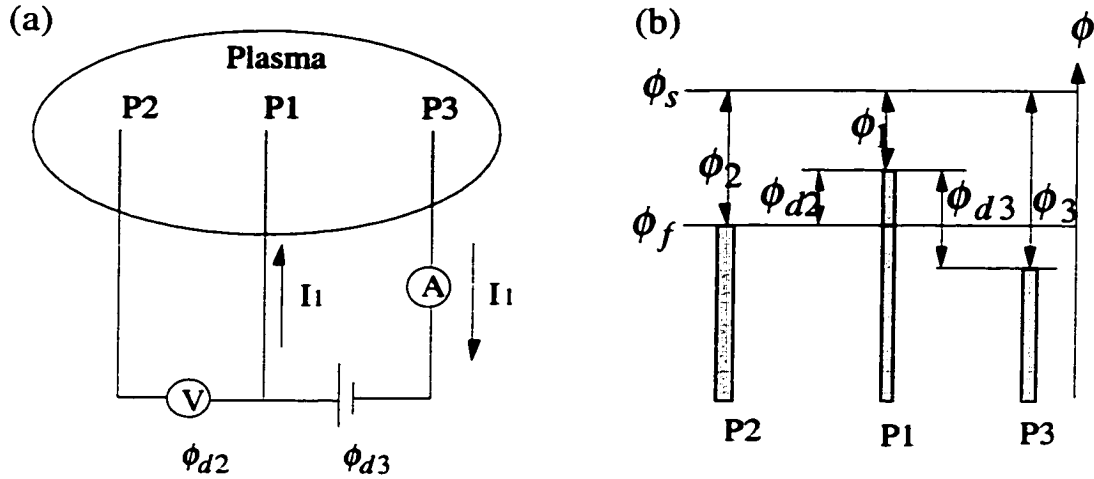


Fig. 2.4 (a) Simplified probe circuit (b) Potential of each probe

Combined with eqs. (2.11) we solve equations (2.12) with respect to T_e and I_+ :

$$\frac{1}{2} = \frac{1 - \exp(-\phi_{d2}/T_e)}{1 - \exp(-\phi_{d3}/T_e)}, \quad (2.13)$$

$$I_+ = \frac{I_1}{1 - \exp((\phi_{d2} - \phi_{d3})/T_e)}$$

In Eqs. (2.13), ϕ_{d3} is controlled by the external power supply. The Voltage difference between P1 and P2, ϕ_{d2} and probe current I_1 are determined with experimental measurement. Thus the electron temperature T_e can be determined

with the first equation of (2.13). Plasma density may be inferred with ion saturation determined by the second equation of 2.13 and Eq. 2.7. The time resolution of T_e and n measurement is only limited by the data sampling rate up to the ion plasma frequency.

A simple linear relation between T_e and ϕ_{d2} can be derived from the first equation of 2.13 if the bias voltage $\phi_{d3} \gg T_e$:

$$T_e \approx 1.44\phi_{d2} \quad 2.14$$

This is the triple probe method of measuring the electron temperature, from the voltages measured at the positively biased tip and the floating potential. Equation (2.14) is used to determine electron temperature in experiment by setting the bias voltage $\phi_{d3} \sim 4T_e$.

2.2.4 Discussion of simple probe theory

The simple probe theory presented above enabled us to measure electron temperature, density and plasma potential in a relatively easy way. Several assumptions had to be made which may not always be true in experimental conditions. First, it is assumed that the ions are cold, which is not true

experimentally and it would have to be taken into account in the calculation of the ion sound speed. For the plasmas of finite ion temperature, dependence of ion current upon ion temperature is shown by Laframboise's calculation [7, 8]. Only a slight change is needed in ion saturation current, i.e. the $\exp(-1/2) \sim 0.61$ in Eq. 2.4 is replaced with 0.53 under the condition of $T_i \leq T_e$. Previous measurement of ion temperature [16] shows that the condition above is satisfied in the plasmas of MST. So 0.53 is used in the formula of ion saturation Eq. 2.4 for density calculation throughout this thesis.

Second, the electron and ion collection areas are independent of the sheath thickness since we have assumed that the probe geometry is an infinite plane. If cylindrical or spherical probe are used, the particle collection area increases with the probe potential because the probe sheath thickness follows Eq. 2.2 [4]. In MST experiment, the probe dimension is usually much larger than the sheath thickness ($a_{\text{probe}} \sim 3 \text{ mm}$, sheath thickness $\sim 0.1 \text{ mm}$). The probe surface area is a good estimation for particle collection.

Third, the magnetic fields were neglected in simple probe theory. This is usually not correct in magnetically confining fusion devices. The magnetic field makes the charged particles gyrate about the field lines, slows down the cross field particle diffusion, and thus breaks down the space isotropy of plasmas. The

importance of the magnetic field is dependent on the ratio of Larmor radius ρ to the typical dimension a_{probe} of the probe [6, 7]. For the case of comparable ion and electron temperature ($T_i \sim T_e$), electron Larmor radius is much smaller than ion Larmor radius by the factor of $\sqrt{m_e/m_i}$. The electrons are more strongly affected than ions. The magnetic field can be classified into three regimes according to the ratio of Larmor radius to probe dimension: a weak field in which $\rho_{i,e} \gg a_{probe}$, a strong field in which $\rho_i \gg a_{probe} \gg \rho_e$, and a very strong field in which $a_{probe} \gg \rho_{i,e}$. Apparently no modification of I-V characteristics in simple probe theory is needed in the case of weakly magnetized plasmas. In the strong fields, most electron current comes from the electrons traveling along the magnetic field. Electron saturation is thus decreased due to the fact that the effective area of electron collection is the projection in the direction of the magnetic field instead of the probe surface. One may worry about the problem of electron depletion in the magnetic flux tube. Fortunately for triple Langmuir probes, most electrons along the magnetic fields are repelled since the probe is operated around the floating potential ϕ_f , which is sufficiently negative with respect to plasma potential ϕ_s . So the electron collection current is still governed by the thermal Boltzmann factor as before. In the case of very strongly magnetized plasmas $a_{probe} \gg \rho_{i,e}$, ion collection along the flux tube is balanced by a cross field diffusion, like electron collection. No simple analytical solution for probe characteristics exists. So the

probe dimension has to be carefully selected to avoid this situation in practical experiment. In MST probe experiment, the probe dimension a_{probe} is ~ 3 mm, ion Larmor radius $\rho_i \sim 20$ mm, and $\rho_e \sim 0.04$ mm, satisfy the strong field condition $\rho_i \gg a_{probe} \gg \rho_e$. The simple probe theory of triple probe techniques can be used with only one modification in electron collection area. Using A_- to represent electron collection area and A_+ to represent ion collection area, probe current-voltage equations are modified as followed:

$$\begin{aligned} I_- &= enA_- \sqrt{T_e / 2\pi m_e} \\ I_+ &= 0.61A_+ en \sqrt{T_e / m_i} \end{aligned} \quad , \quad 2.15$$

$$I = \begin{cases} -I_- \exp\left(\frac{\phi - \phi_s}{T_e}\right) + I_+, & \phi < \phi_s \\ -I_-, & \phi > \phi_s \end{cases} \quad , \quad 2.16$$

$$\phi_f = \phi_s - \alpha T_e \quad , \quad 2.17$$

$$\alpha = \left[\frac{1}{2} + \ln\left(\frac{A_-}{A_+} \sqrt{\frac{m_i}{2\pi m_e}}\right) \right] \quad , \quad 2.18$$

In the probe experiment of this thesis, $A_-/A_+ \sim 0.5$. Thus the value of α is around 2.3, showing a decrease of sheath potential drop due to the existence of magnetic field.

2.2.5 Error analysis of probe measurement

In this section, I discuss the error of probe measurements induced by fast electron and non-identical probe areas. Fast electrons are observed in the edge of several RFP devices [9, 10]. These fast electrons have an error effect on the interpretation of probe data if the simple probe theory is used. The errors are raised due to the involvement of the fast electrons with 5-10 times of bulk electron temperature and the emission of secondary electron in the probe I-V equations as shown below:

$$\begin{aligned}
 -I_1 &= -I_- \exp(-\phi_1/T_e) - \delta\sqrt{\beta}(1-\gamma)I_- \exp(-\phi_1/\beta T_e) + I_+ \\
 0 &= -I_- \exp(-\phi_2/T_e) - \delta\sqrt{\beta}(1-\gamma)I_- \exp(-\phi_2/\beta T_e) + I_+ \quad , \quad 2.19 \\
 I_1 &= -I_- \exp(-\phi_3/T_e) - \delta\sqrt{\beta}(1-\gamma)I_- \exp(-\phi_3/\beta T_e) + I_+
 \end{aligned}$$

In equation 2.19, we define $\delta \equiv n^f/n \ll 1$ and $\beta \equiv T_e^f/T_e > 1$, where n^f , and T_e^f are the density and temperature of fast electrons respectively, and γ is the emission coefficient of secondary electrons. All fast electron terms are led by $\delta\sqrt{\beta}(1-\gamma)$, complicating the algebra for calculation of temperature and α (in equation 2.9). Detailed discussion may be found in reference [6]. Here I provide only the summary of the results. The density and temperature of fast electrons have been

measured with electron energy analyzer (EEA) in MST [9]. Using average fast electron temperature of 5 times the edge bulk electron temperature, density 5% of the background plasma density, and 1.3 of emission coefficient of secondary electrons [14], the resulting errors of n_e and T_e estimation with triple probe model discussed in section 2.2.2 are $< 10\%$.

All discussion presented so far assumes identical probe areas. However it is difficult to construct and maintain the probe with the identical geometry and equivalent areas. The error of the measurement due to this effect can be estimated by generalizing probe I-V equations as follows:

$$\begin{aligned}
 -I_t &= -I_{1-} \exp(-\phi_1/T_e) + I_{1+} \\
 0 &= -I_{2-} \exp(-\phi_2/T_e) + I_{2+} \\
 I_t &= -I_3 \exp(-\phi_3/T_e) + I_{3+}
 \end{aligned}
 \tag{2.20}$$

The number 1, 2, and 3 represent the probe P1, P2, and P3, I_t is the total current of each probe. Let's define k_1 and k_2 as the ratios of probe areas:

$$\begin{aligned}
 k_1 &= I_1/I_3 = A_1/A_3 \\
 k_2 &= I_2/I_3 = A_2/A_3
 \end{aligned}
 \tag{2.21}$$

The k_1 and k_2 will enter equation 2.13 that provides the density and temperature calculation. Compare these modified formulas with equation 2.13 of identical

probe areas. One would be able to estimate the error of density and temperature measurement. Details of error analysis algebra may be found in reference [11]. Error of temperature as a function of error of probe area is shown in Fig. 2.5 (a), where the probe area error is defined as $\varepsilon_A = (A_1 - A_3)/A_1$. A_1 and A_3 represent the areas of positively and negatively biased probe respectively. The error of electron temperature is defined as $\varepsilon_{T_e} = (T_{e,est} - T_e)/T_e$. The subscript *est* represents the estimated quantity with identical probe area. Fig. 2.5 (b) shows error of density depends on both error of temperature and the area of negatively biased probe A_3 . Error of density and A_3 is defined as $\varepsilon_{n_e} = (n_{e,est} - n_e)/n_e$ and $\varepsilon_{A_3} = (A_{3,est} - A_3)/A_3$, respectively. If the error of probe area is within 10%, the error of density and temperature is negligible.

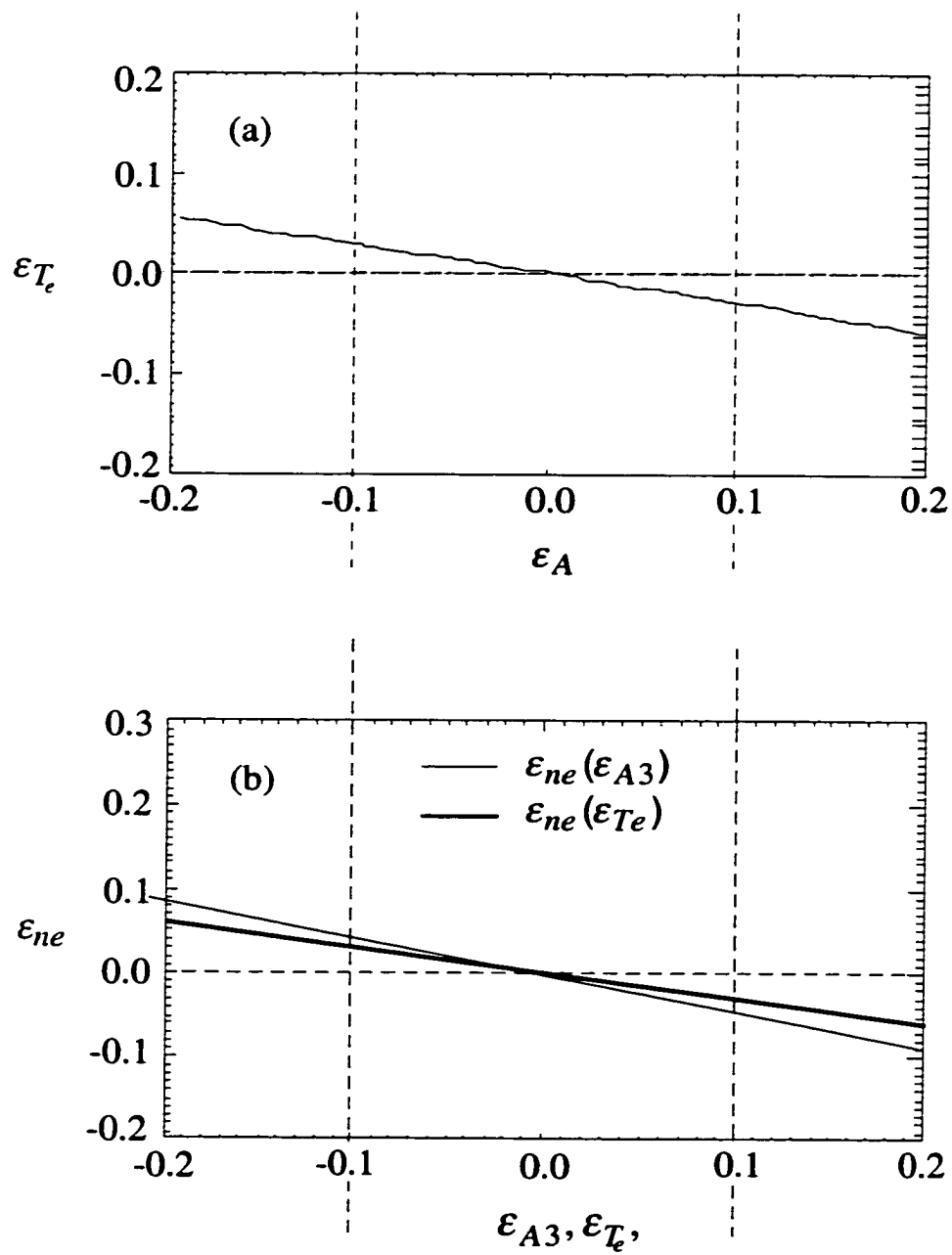


Fig. 2.5 (a) errors of temperature as a function of error of probe area, (b) error of density as a function of temperature and negatively biased probe area.

2.2.6 Probe design and construction

The probe measurements in this thesis were made at $r/a > 0.88$ (6 cm from the plasma boundary), 45 degree above the outside midplane of the MST. The electrostatic probe used for correlation and transport studies consists of an array of four probes. Three of them function as regular triple probe. The fourth tip is left floating in order to couple with the other floating tip for potential wavenumber k_ϕ measurement. The other 2 tips forming a floating pair are biased up to 200 volts [$\geq 4kT_e$] to obtain the ion saturation and temperature measurement as mentioned in previous sections of this chapter. Several factors are considered before the construction of the probe.

I) Selection of materials

Selection of proper materials is critical for the probe to survive in environment of high heat load like fusion plasmas. The probe body usually consists of two parts: metal electrodes that are exposed in plasmas to collect electrical current, and insulator probe protectors that protect the probe wiring and stainless steel body from contacting plasmas. Several criteria are considered for material selection. For metal electrodes, pure metals are better candidates since alloys usually have a

lower melting point. Iron is not good because it is not good in the magnetized environment. Metals of high atomic number (heavy metal) can minimize the sputter effect. Molybdenum and tungsten are two good candidates to satisfy these criteria. Since tungsten has lower heat capacity and is harder for machining, molybdenum becomes our choice for probe metal electrodes.

Ceramics is usually the material of the probe protector. Boron nitride is our final selection because of the following properties: easy to machine, chemically stable, high heat conductance while electrically insulating. The last property is very important for the protector to survive without cracking in an environment with large heat shock.

II) Selection of probe dimension

The physical size of probe must be chosen carefully for several reasons. First, the probe dimension has to be large enough to minimize overheating [12]. Thermionic electron emission is a strong function of probe temperature [13]. Thermionic emission at probe temperatures close to the melting point may dominate the ion current collection, then complicate the probe I-V equations and data analysis. A simple analysis with heat transfer equation shows that the probe

diameter has to be larger than 2.5 mm to keep the temperature of the probe surface much lower than the melting point.

On the other hand, the probe dimension has to be small enough to minimize perturbation on the global plasmas by probe biasing. Considering the effect of sheath expansion, the probe has to be much larger than the sheath thickness in order to keep the electron and ion collection areas as constant as possible under the condition of large fluctuating potential. Another important factor for the probe size selection is to make the non-magnetized ion current equations still valid. This criteria can be met only when condition $\rho_i \gg a_{probe} \gg \rho_e$ mentioned in section 2.2.3 is satisfied, where $\rho_i \sim 20$ mm, and $\rho_e \sim 0.4$ mm.

Fourth, considering the convenience of the probe construction, 2.5 mm diameter molybdenum rod is a typical size in stock. Except for the work of cutting the rods to the proper length, no extra complicated machining work is needed. Thus 2.5 mm diameter semi-spherical surface is chosen since this satisfies all criteria mentioned in this section.

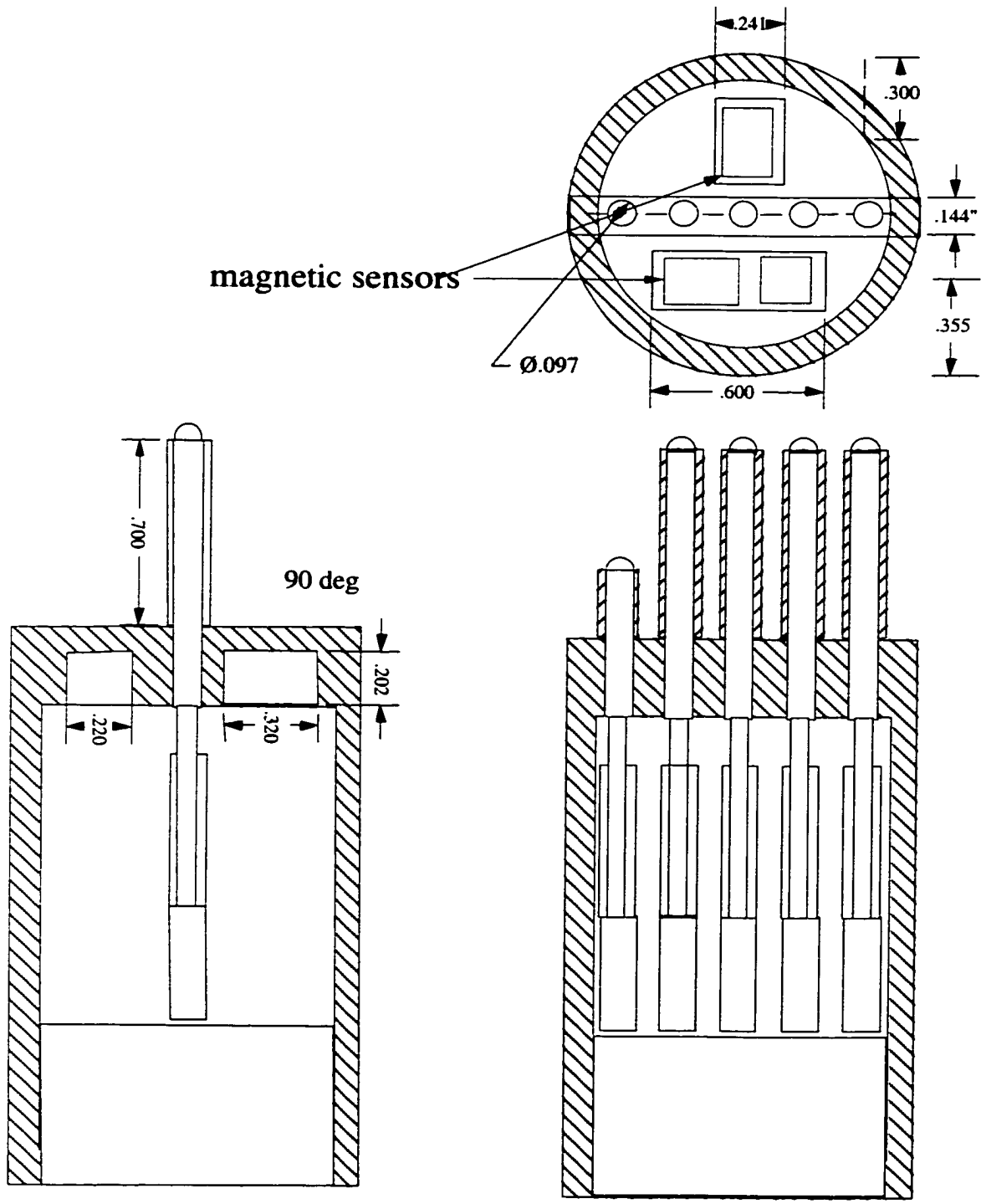


Fig. 2.6 Top view and side diagram of electrostatic probe

III) Geometry of probe

The probe geometry most widely used is tripod. The three probes are located at the three top corners of a equal lateral triangle. In magnetized plasmas, charged particles drifting along magnetic fields usually induce a shadowing effect, i.e. the probe in the upstream location shadows the probe in the downstream position. To minimize this effect, probes must be constructed as a linear array perpendicular to the local field lines. The distance between probes has to be much larger than the sheath thickness and smaller than the fluctuation correlation length.

Fig 2.6 shows one top view and two side views of probe structure diagram. All shaded parts are boron nitride probe protectors. The semicircles extending 2.5 mm from the probe protectors on the top of side view picture are tips of molybdenum rods. The diameters of these rods are also 2.5 mm. The distance between probes is ~ 2.6 mm. The four long probes are used for electrostatic transport measurement. A $10,000 \mu F$ biasing capacitor, coupled with a low resistor ($\sim 20 \Omega$), is connected between two probes for current measurement. The other two probes are left floating for measuring toroidal wavenumber of potential fluctuations. Electron temperature is measured by coupling a large resistor ($\sim 100 \text{ k}\Omega$) between the positively biased probe and one of the floating probes. Floating potential is equivalent to the potential drop across a $100 \text{ k}\Omega$ resistor coupled between the

floating probe and vacuum vessel. The short probe is designed for radial electric field measurement that is not important in this thesis. Three components (B_r , B_θ , B_z) of magnetic pickup coils are installed in the probe for local coherence measurement of electrostatic and magnetic fluctuations.

Fig. 2.7 shows the schematic diagram of the electrostatic probe system. Three voltage dividers are used to avoid the signal saturation in isolation amplifier and ADC. The resistance for the J_{sat} measurement must be selected so that the voltage drop across the resistor is much smaller than the bias voltage. The isolation amplifiers serve two purposes: (1) Since the triple Langmuir probe is a floating system, the resistors for J_{sat} and T_e measurement must be isolated from ADC ground. (2) Since both the probe body and ADC are grounded through the VCV, isolation amplifiers are used to avoid the internal ground loop.

In order to minimize the noise of the measurement of the electrostatic probe, several careful steps of hardware design are critical: (1) all the voltage dividers, isolation amplifiers, and the probe bias capacitor are enclosed in a VCV grounded stainless steel box. (2) Isolation amplifiers are powered with rechargeable batteries, which are also enclosed in the grounded box. (3) The power supply charging the probe bias capacitor must be disconnected during the discharges.

In order to minimize the signal aliasing effect due to the signal digitization, the low pass filters are connected right before the ADC to cut off the signals above the Nyquist frequency (100kHz if signals are digitized at 200kHz). The signal saturation of the ADC due to the high frequency spikes can be avoided with these low pass filters.

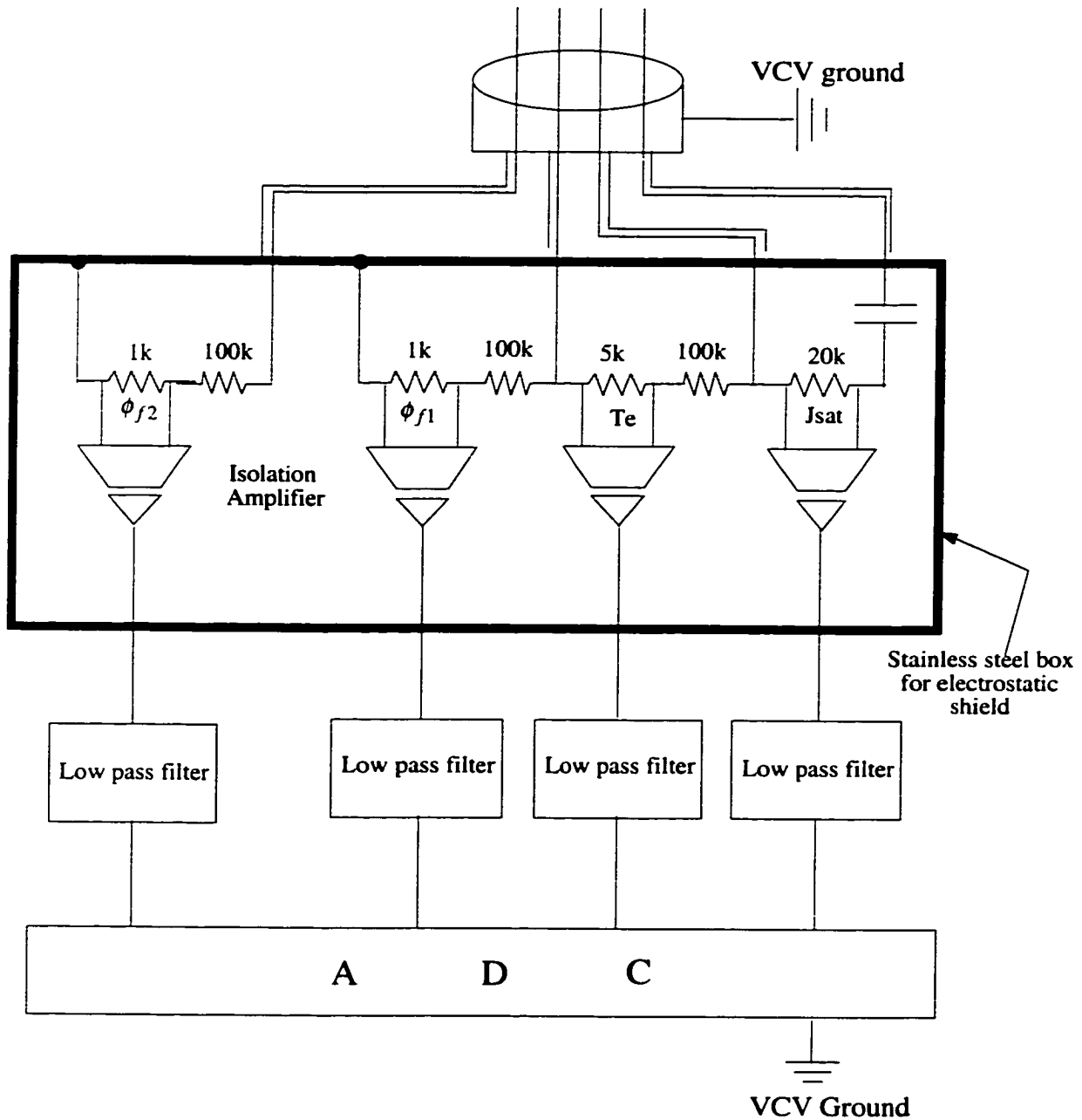


Fig. 2.7 Circuit diagram of electrostatic probe system

2.3 Magnetic pickup coils

Magnetic pickup coils are the simplest diagnostics of magnetic field measurement. Three kinds of magnetic probes are used in this thesis. First, in order to study the local correlation between electrostatic and magnetic fluctuations, magnetic pickup coils of three spatial components (B_θ , B_ϕ , and B_r) are installed in the electrostatic probe (see Fig. 2.6). All coils are mounted on small coil holder made from machinable ceramic (boron-nitride). The number of coil turns is maximized so that the signal noise ratio may be optimized.

Second, with the techniques of the 2-point method, the forked probe [15] is used for obtaining the dispersion relation and wavenumber-frequency spectrum of magnetic fluctuations. The dispersion relation reveals the phase velocity and wave propagation direction. The forked probe consists of 8 magnetic pickup coils placed in 2 stainless steel tubes with 4 coils in each one (Fig. 2.8). The magnetic pickup coils are mounted in the same way as those in electrostatic probes. The two stainless tubes are 1.7 cm apart and serve as the electrostatic shield. On the outside of the stainless steel tubes are boron-nitride tubes serving as the particle shield and heat shield of the probe.

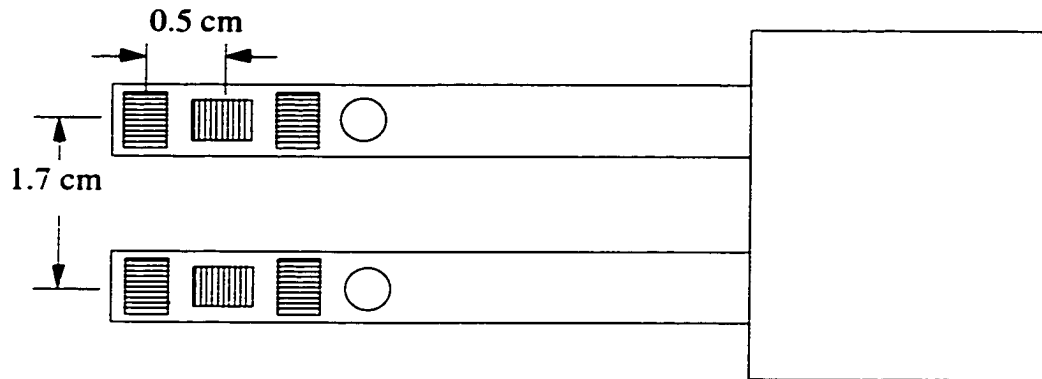


Fig. 2.8 The simplified structure of the forked probe

The third magnetic diagnostic is the 32-magnetic-coil array evenly distributed at the plasma boundary. As shown in Fig. 2.9, the coil array is mounted at the inner side circumference of the toroidal direction. Spatial Fourier decomposition of the coil array signal determines the toroidal mode number (n) spectrum and the mode phase velocities. Two-point phase analysis may also be used to statistically determine the mode-number frequency spectrum of magnetic fluctuations. Since the array coils are further apart than the forked probe, $n = 16$ is the maximum mode number that the toroidal array can provide.

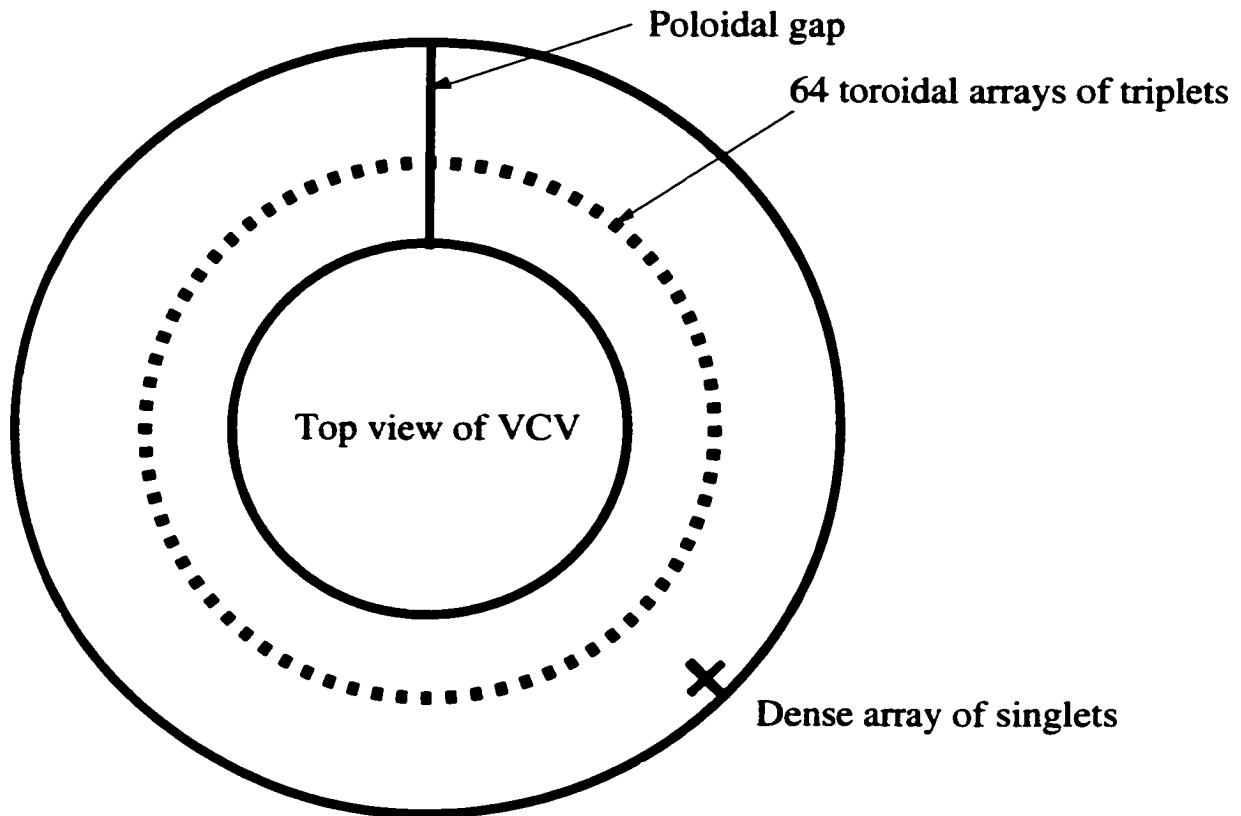


Fig. 2.9 Schematics of toroidal array

The output of each coil is proportional to the time derivative of the magnetic field, i.e.,

$$V_{out} = -A_{eff} \frac{dB}{dt} \quad 2.22$$

where A_{eff} is the effective area of the coil calibrated with Helmholtz coil set [15].

The A_{eff} of the coils falls between 1.0 and 2.0 cm².

References

1. R. Dexter, *et. al.*, *Fusion Technol.* **19**, 131 (1991)
2. A. Almagri *et. a l.*, *phys Fl. B* **4**, 4080 1992
3. F. F. Chen, in *Plasma Diagnostics Techniques*, K. H. Huddlestone and S. L. Leonard, Eds., Academic Press, (1965)
4. M.A. Lieberman & A.J. Lichtenberg, *Principles of plasma discharges and materials processing*, Wiley (1994)
5. S. L. Chen and T. Sekiguchi, *J. Appl. Phys.* **36**, 2363 (1965)
6. H. Ji, H. Toyama, K. Yamagishi, S. Shinohara, A. Fujisawa, and K. Miyamoto, *Rev. Sci. Instrum.* **62**, 2326 (1991)
7. I. Hutchinson, *Principles of plasma diagnostics* (Cambridge University, Cambridge, 1987)
8. J. Laframboise, in *Rarefied Gas Dynamics*, edited by J. H. de Leeum (Academic, New York, 1966), Vol. 2, p. 22.
9. M. Stoneking, Ph.D. Thesis University of Wisconsin - Madison (1994)
10. J.C. Ingraham, *Phys. Fluids B2*, 143 (1991)
11. M. Meier, Ph.D. Thesis, University of Texas - Austin (1998)
12. G. Fiksel, private communication, (1998)
13. Gibbons D.J., *Thermionic Emission in Handbooks of Vacuum Physics V2 Physical Electronics*, edited by Beck A.H., Pergamon, 1966
14. Gibbons D.J., *Secondary Electron Emission in Handbooks of Vacuum Physics V2 Physical Electronics*, edited by Beck A.H., Pergamon, 1966
15. WeiMin Shen, Ph.D. thesis, University of Wisconsin - Madison (1992)
16. N. Crocker, private communication

Chapter III. Data analysis techniques

The ensemble average of the cross product of two fluctuating quantities \tilde{x}_1 and \tilde{x}_2 provides very important information for the understanding of fluctuations. For example, fluctuations in density and radial velocity can induce a radial particle flux when they oscillate in a correlated way, that is

$$\Gamma(x, t) = \langle \tilde{n}(x, t) \tilde{v}_r(x, t) \rangle \quad 3.1$$

where x represents the location of the probes, t represents the time when the measurement is carried out. We consider only the electrostatic particle transport, i.e., the radial velocity fluctuations are due to $\tilde{E}_t \times B$ drifts, where \tilde{E}_t is the

transverse electric field (to the mean magnetic field) induced by the fluctuating plasma potential $\tilde{E}_t = -\nabla_t \tilde{\phi}_{pl}$. Then equation 3.1 can be rewritten as

$$\Gamma(\vec{r}) = \langle \tilde{n}(\vec{r}, t) \tilde{E}_t(\vec{r}, t) \rangle / B \quad , \quad 3.2$$

where B is the equilibrium magnetic field. In order to study the fluctuation and transport response due to improved confinement in more detail, frequency spectra of the fluctuation cross product are important quantities. Fourier spectral analysis becomes the most important technique of data analysis for this purpose.

In Sec. 3.1, I describe the criteria of ensemble selection and several signal processing techniques before spectral analysis. These manipulations assure the repetitiveness of discharges and avoid aliasing effects that introduce frequency components that do not exist in the true fluctuations. To achieve favorable statistics in turbulent plasmas, many data samples must be selected for spectral analysis. In section 3.2, I review the fundamentals of the spectral analysis. Several important quantities, such as the auto and cross power spectrum, the relative phase spectrum and the coherence spectrum are defined. In section 3.3, the concept and algebra of the wavenumber-frequency spectrum is described. From the location of the peaks and the spectrum breadth, the characteristics between fluctuations may be distinguished.

3.1 Ensemble selection and signal processing

All probe signals are digitized at a certain sampling frequency and stored as vectors along with their corresponding time vectors by MDS (Module data system) data acquisition software. The analysis of the data is then carried out using the IDL (Interactive data language) software package.

To assure favorable statistics for turbulent fluctuation data, large data ensembles are selected during the flat top of plasma current since most plasma parameters are stabilized at the flat top of plasma current. Typically several hundred of time series data records are used for an ensemble average. The data records are selected for reproducibility. Variation of plasma current and line-averaged density must be within 10%. Each ensemble for spectral analysis excludes sawtooth crash events since electrostatic probe signals exhibit large bursts at these times. For PPCD discharges, all the repetitive bursts (corresponding to $m = 0$, $n = 1$ magnetic modes) are also avoided.

Fast Fourier Transform (FFT) spectral analysis is used to obtain spectra of fluctuation power, phase, coherence, particle flux, and the modenumber-frequency spectrum. Before applying the FFT to any data records, their means and linear trends are subtracted out. If low frequency data are important for analysis, linear trends of the data records are kept. The electronic system for Langmuir probe signals is operated with a 100kHz single pole (simple RC) filter. Correction for

roll-off and phase shift of the low pass filter must be applied after applying FFT to data records. The correction for the low pass filter is given by

$$F_{RC} = (1 + i2\pi fRC) \quad 3.3$$

Fluctuation frequencies above 100kHz contribute only a negligible portion of the fluctuation power and transport. Thus the bandwidth f_B of the low pass filter mentioned above is set at 100kHz. One important function of the low pass filter is to minimize the amplifier saturation due to some unexpected high frequency noise.

Another important function of the low pass filter is for the purpose of anti-alias. According to the sampling theorem [1], the sampling frequency must be at least twice of the signal bandwidth in order to avoid the phenomena of aliasing, i.e.

$$f_{sample} \geq 2f_B \quad , \quad 3.4$$

Thus it is very important to select a high enough sampling rate so that Eq. 3.4 is satisfied. A low pass filter with roll-off frequency at f_B is able to force the signal bandwidth satisfying Eq. 3.4. Usually the frequency f_B is called the Nyquist frequency.

The other factor that may alias the signal during analysis is the finite record length. Each data record in this thesis contains 128 points and is of 0.5 ms duration. High frequency aliasing may arise due to the sharp cut-off at both ends of the finite length of each data record. A window function called the Hanning

window then is multiplied to each data record to minimize this kind of aliasing effect. The Hanning window has the shape of the cosine function:

$$W_{hanning} = \frac{1}{2} \left[1 - \cos\left(\frac{2\pi t}{T}\right) \right] , \quad 3.5$$

where T is the data record length of 0.5 ms.

3.2 Review of statistical spectral analysis

The auto correlation of a fluctuating quantity \tilde{x}_1 is defined as

$$R(\bar{r}, \tau) = \langle \tilde{x}_1(x, t) \tilde{x}_1(x, t + \tau) \rangle , \quad 3.6$$

If this fluctuation \tilde{x}_1 is propagating, it can be expressed as a summation of Fourier components,

$$\tilde{x}(\bar{r}, t) \equiv \sum_f x(f) e^{i\bar{k}(f) \cdot \bar{r} - i2\pi f t} , \quad 3.7$$

then the Fourier transform of $\tilde{x}(\bar{r}, t)$ is given by:

$$X(\bar{r}, f) \equiv x(f) e^{i\bar{k}(f) \cdot \bar{r}} = FFT[\tilde{x}(\bar{r}, t)] , \quad 3.8$$

For weakly stationary fluctuations, one can compute the auto power spectrum of a fluctuating quantity in the frequency domain:

$$S(\bar{r}, f) = \langle X_1(\bar{r}, f) X_1^*(\bar{r}, f) \rangle , \quad 3.9$$

where $S(\bar{r}, f)$, $X_1(\bar{r}, f)$ are Fourier transform of $R(\bar{r}, \tau)$, $\tilde{x}_1(\bar{r}, t)$ respectively, i.e.

$$R(\bar{r}, \tau) = \int_{-\infty}^{\infty} S(\bar{r}, f) e^{-i2\pi f \tau} df , \quad 3.10$$

$$X_1(\bar{r}, f) \equiv x_1(f)e^{i\bar{k}(f)\cdot\bar{r}} \quad , \quad 3.11$$

and the asterisk denotes a complex conjugate.

Now consider the case of $\tau = 0$. The equation 3.10 reduces to:

$$R(\bar{r}) = \int_{-\infty}^{\infty} S(\bar{r}, f)df \quad , \quad 3.12$$

where $R(\bar{r})$ denotes the mean square value of $\bar{x}_1(\bar{r}, t)$. The function $S(\bar{r}, f)$ indicates how the mean square value is distributed over frequency, i.e. a spectral density function with the unit in volts²/Hz, if \bar{x}_1 has the unit in volts. The function $S(\bar{r}, f)$ is generally referred to as the power spectrum of fluctuation $\bar{x}_1(\bar{r}, t)$.

If two fluctuating quantities $\bar{x}_1(\bar{r}, t)$ and $\bar{x}_2(\bar{r}, t)$ are considered, the cross correlation function R_{12} and the cross power spectrum S_{12} are defined as:

$$R_{12}(\bar{r}, \tau) = \langle \bar{x}_1(x, t)\bar{x}_2(x, t + \tau) \rangle \quad , \quad 3.13$$

$$S_{12}(\bar{r}, f) = \langle X_1(\bar{r}, f)X_2^*(\bar{r}, f) \rangle \quad , \quad 3.14$$

Similar to the relation between the auto correlation function and auto power spectrum, R_{12} and S_{12} are Fourier transform pairs if the fluctuations are weakly stationary:

$$R_{12}(\bar{r}, \tau) = \int_{-\infty}^{\infty} S_{12}(\bar{r}, f)e^{-i2\pi f\tau}df \quad , \quad 3.15$$

Consider the case of $\tau = 0$, Eq. 3.13 and Eq. 3.15 reduce respectively to:

$$R_{12}(\bar{r}) = \langle \bar{x}_1(x, t)\bar{x}_2(x, t) \rangle \quad , \quad 3.16$$

$$R_{12}(\bar{r}) = \int_{-\infty}^{\infty} S_{12}(\bar{r}, f)df \quad , \quad 3.17$$

The cross power spectrum $S_{12}(\vec{r}, f)$ provides two important pieces of information: the relative phase and the coherence between the two fluctuations.

The phase spectrum $\theta_{12}(f)$ is given by the real and imaginary parts of S_{12} :

$$\theta_{12}(f) = \tan^{-1} \left[\frac{\text{Im}(S_{12}(f))}{\text{Re}(S_{12}(f))} \right], \quad 3.18$$

The coherence spectrum is defined in terms of the auto and cross-power spectra:

$$\gamma_{12}(f) = \frac{|S_{12}(f)|}{[S_{11}(f)S_{22}(f)]^{1/2}} \quad 3.19$$

The phase spectrum determines how much the cross power goes to the real or imaginary part, and also determines the polarity of the real and imaginary part. For example if the phase difference between the 2 signals is 0 or π , the real part of the S_{12} is maximum, and the imaginary part is zero. Zero phase difference gives a positive maximum real part whereas the real part is negative for the phase difference of π . The opposite result is obtained if the phase difference is $\pi/2$ or $3\pi/2$. The real part is zero in this case, and the imaginary part is maximized. The polarity of the imaginary part is positive for $\pi/2$ and negative for $3\pi/2$. Relative phase may be used for derivation of the wavenumber-frequency spectrum. I will discuss this important technique in the next sections.

The coherence spectrum measures the degree of similarity between the two signals as a function of frequency. It is always real with magnitude between zero

and unity. Two signals with unity coherence are perfectly coherent and identical except for a possible phase shift and constant multiplicative factor, while the two completely unrelated signals will have zero coherence. If the same signal is simultaneously measured at two locations separated with distance d , the coherence length can be estimated with

$$L_{coher}(f) = \frac{d}{-\ln \gamma_{12}} \quad , \quad 3.20$$

3.3 Equation of electrostatic fluctuation induced particle transport

Particle transport driven by electrostatic fluctuations is given by Eq. 3.2, i.e.,

$$\Gamma(\vec{r}) = \langle \tilde{n}(\vec{r}, t) \tilde{E}_t(\vec{r}, t) \rangle / B \quad ,$$

where \tilde{E}_t is the transverse electric field induced by the fluctuating plasma potential $\tilde{E}_t = -\nabla_t \tilde{\phi}_{pl}$. From Eq. 3.8 in Sec. 3.2, the Fourier transform of any fluctuating quantity $\tilde{x}(\vec{r}, t)$ is given by:

$$X(\vec{r}, f) \equiv x(f) e^{i\vec{k}(f) \cdot \vec{r}} = FFT[\tilde{x}(\vec{r}, t)] \quad 3.8$$

Now let $N(\vec{r}, f)$ and $\Phi(\vec{r}, f)$ represent the Fourier transform of $\tilde{n}(\vec{r}, t)$ and $\tilde{\phi}_{pl}(\vec{r}, t)$ respectively. Using equation 3.8, we obtain

$$N(\vec{r}, f) \equiv n(f) e^{i\vec{k}(f) \cdot \vec{r}} \quad 3.21$$

$$\Phi(\vec{r}, f) \equiv \phi(f)e^{i\vec{k}(f)\cdot\vec{r}} \quad 3.22$$

We already know that $\vec{E}_t = -\nabla_t \vec{\phi}_{pl}$. So the electric field fluctuations in frequency domain can be represented as:

$$E_t(\vec{r}, f) = -\nabla_t \Phi(\vec{r}, f) = -ik_t \phi(f)e^{i\vec{k}(f)\cdot\vec{r}} \quad , \quad 3.23$$

Now use equation 3.9, and let X_1 represent the density spectrum and X_2 represent electric field spectrum. The particle flux spectrum $T(\vec{r}, f)$ is then given by the imaginary part of the cross product of density spectrum, wavenumber spectrum and conjugate of plasma potential spectrum divided by the equilibrium magnetic field B :

$$T(\vec{r}, f) = \frac{1}{B} \text{Re} \left\{ \left\langle N(\vec{r}, f) [-ik_t(f)\phi(\vec{r}, f)]^* \right\rangle \right\} = \frac{1}{B} \text{Re} \left\{ \left\langle ik_t(f)N(\vec{r}, f)\phi(\vec{r}, f)^* \right\rangle \right\}$$

$$T(\vec{r}, f) = \frac{1}{B} \text{Im} \left\{ \left\langle k_t(f)N(\vec{r}, f)\phi(\vec{r}, f)^* \right\rangle \right\} \quad , \quad 3.24$$

Neglecting the space coordinate, equation 3.24 can be rewritten as:

$$T(f) = \frac{1}{B} k_t(f) \langle A_N(f) \rangle \langle A_\Phi(f) \rangle \gamma_{n\phi}(f) \sin \theta_{n\phi}(f) \quad , \quad 3.25$$

where $A_N(f)$ and $A_\Phi(f)$ are the amplitude spectra of density and plasma potential fluctuations, and $\theta_{n\phi}(f)$ and $\gamma_{n\phi}(f)$ are the relative phase angle and the coherence between them. Equation 3.25 reveals that the particle flux is not only the function of fluctuation amplitudes, but also depends on the way they are correlated: the degree of coherence and the relative phase between them.

3.4 The wavenumber-frequency spectrum

In fusion plasmas, most signals in fusion plasmas are not deterministic in dispersion relation, i.e., for a given frequency f , a range of possible wavenumber k instead of a single k may be observed, and for given wavenumber k , there may exist a range of frequency f . In this situation, a two-variable statistical quantity called the wavenumber-frequency spectrum $S(k, f)$ is the best way to describe the broadened turbulent dispersion relation. The function $S(k, f)$ describes how fluctuation power is distributed in frequency and wave number. The main purpose of using this quantity in this thesis is to distinguish the characteristics of electrostatic and magnetic fluctuations. The simplest technique used for deriving $S(k, f)$ is FFT spectral analysis and the two-point method [2]. In this technique, two fixed probes separated by a distance d are operated to collect data simultaneously. It is assumed that the fluctuations consist of a superposition of sinusoidal components in time and space. The local wave number of each data record at a given frequency f is calculated from the phase spectrum between the two probes:

$$k(f) = \theta_{12}(f)/d \quad , \quad 3.18$$

where $\theta_{12}(f)$ is given by equation 3.15 and d is the probe separation.

Then the auto power spectrum $S_{II}(f)$ is used with the wavenumber spectrum $k(f)$ to infer the $S(k, f)$. For a given frequency of a data record, the power $S_{II}(f)$ is recorded in the coordinate point of (k, f) where k is given by Eq. 3.18. The $S(k, f)$ is then finalized by repeating the process for all frequency and data ensembles on the two-dimensional coordinate (k, f) . This method is similar to the estimation of probability density functions by means of a histogram.

Reference

1. E. J. Power, **Reference guide for intelligent signal analysis**, (1988)
2. J. M. Beall, Y. C. Kim, and E. J. Power, **J. Appl. Phys.** **53**, 3933 (1982)

Chapter IV Electrostatic fluctuations and particle transport in improved confinement

As I have discussed in Chapter 1, magnetic fluctuations govern the particle and energy transport in the core region of MST [1, 2], whereas the particle loss in the edge is dominated by electrostatic fluctuations [3]. Two techniques are employed to improve plasma confinement: PPCD and plasma biasing. PPCD provides transient current drive that flattens the current density profile and reduces the energy source of magnetic fluctuations [4]. Tailoring magnetic fluctuations to reduce the global transport induced by the fluctuations is the original motivation of PPCD. Although previous measurement shows that PPCD decreases magnetic

fluctuations and greatly increases energy and particle confinement time (by a factor of five and eight, respectively) [5, 6], the responses of edge electrostatic fluctuations and transport due to PPCD may not follow that of magnetic fluctuations since the causes of electrostatic fluctuations still remain unknown. On the other hand, even though plasma biasing modestly improves particle confinement, likely due to the localized flow induced by inserted electrodes, neither magnetic fluctuations are reduced nor global energy confinement is improved like PPCD [7]. Understanding of responses of electrostatic fluctuations due to current profile control and biasing induced localized flow hence becomes critical for deeper insight into improved confinement.

The results of the electrostatic probe measurement for both types of improved confinement will be presented in this chapter. Significant reduction of electrostatic particle transport is observed only in plasma biasing. The transport reduction at $r/a \geq 0.96$ in PPCD seems more likely due to the effect of an inward plasma shift. In section 4.1, I present the frequency spectrum and profile of fluctuations and transport. Based upon these, (1) several factors in electrostatic fluctuations that cause the reduction of particle transport may be then clearly identified, (2) The effects that make electrostatic particle flux profile different between PPCD and plasma biasing will be discussed. In section 4.2, I present the modenumber-frequency spectra of magnetic and electrostatic fluctuations. The

change of the propagation may be revealed with the location of the peak in the spectra. A more significant effect in the fluctuation propagation is observed in plasma biasing since the biasing imposes an external radial electric field and can induce significant local plasma flow. In PPCD, the propagation of global magnetic and local electrostatic fluctuations remains mostly the same since PPCD does not alter the plasma flow significantly. The mode number shift of the electrostatic fluctuations induced by PPCD shows the possible decelerated propagation. The different characteristics between magnetic and electrostatic fluctuations can be well identified by the location of the peak in mode number and frequency. In Section 4.3, the $m = 0$, $n = 1$ fluctuations excited by biasing electrodes is discussed. Although the fluctuation amplitudes of this mode are large, it does not contribute much to the particle flux. The measurement of equilibrium quantities will be presented in section 4.4. Changes in plasma density, electron temperature, and plasma potential due to PPCD and plasma biasing are different. I infer the diffusion coefficient using Fick's law with the measured profile of the electrostatic particle flux and density gradient. PPCD and plasma biasing show opposite effect on the diffusion coefficient.

4.1 Electrostatic particle transport in improved confinement

Figure 4.1 (a) shows the edge profile of electrostatic particle transport in the case of PPCD. A decrease of particle flux is observed only at the outermost 4% of the plasma, i.e. for $r/a \geq 0.96$ (from $\sim 10^{21}$ to $< 10^{20}$ $\text{m}^{-2}\text{sec}^{-1}$). A sharp increase in particle flux is measured when the probe moves in. At $r/a \sim 0.90$, the outward particle flux of PPCD is slightly larger than that of the standard discharge. The electrostatic fluctuation profile is shown in Fig. 4.1 (b) and (c). PPCD strongly decreases density fluctuations at the entire edge region, whereas the fluctuation profile in electric field qualitatively follows that of particle flux. Reduction of a factor of > 5 in electric field fluctuations is observed at very edge, increase of a factor of ~ 2 at $r/a = 0.90$. The measurement of electrostatic probes suggests that the current profile control doesn't significantly impact the electrostatic transport even though global particle and energy confinement are significantly improved.

One might suspect that an enhanced $E \times B$ inward motion of the plasma boundary induced by the externally applied poloidal electric field during PPCD results in the enhanced flux gradient and significantly reduced density [Fig. 4.18 (e)] at the edge. However the reduced inward radial $E \times B$ velocity does not provide support for this speculation of plasma compression (Fig. 4.2).

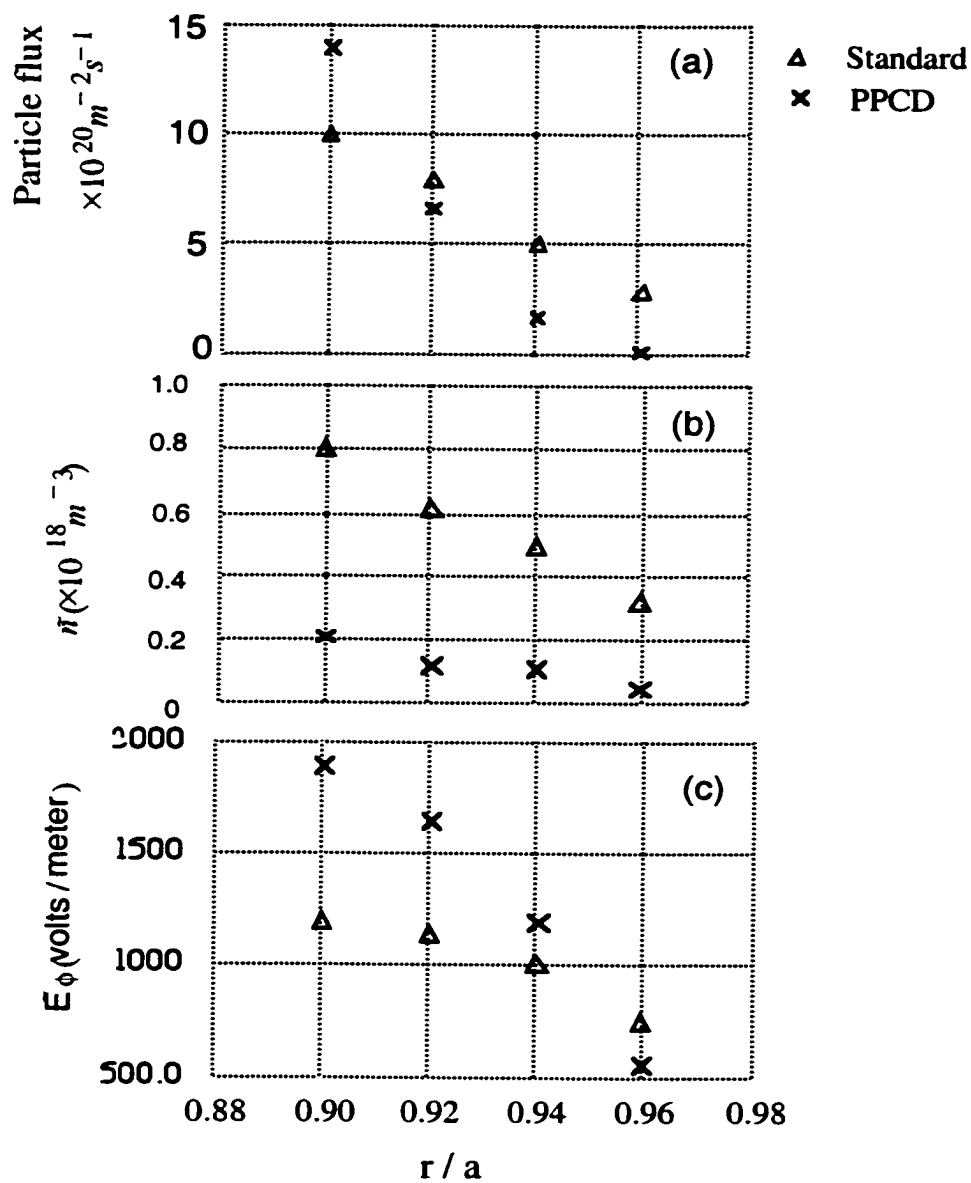


Fig. 4.1 Edge profile of (a) electrostatic particle transport, (b) density fluctuations, and (c) electric field fluctuations for standard and PPCD discharge.

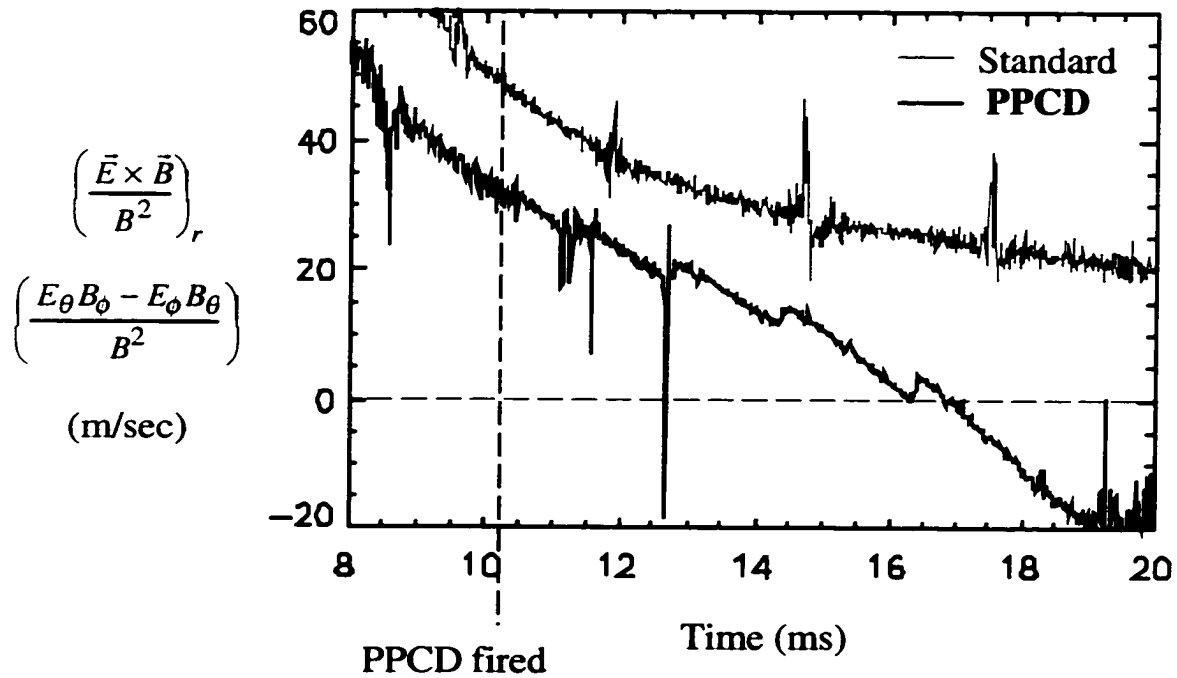


Fig. 4.2 Inward radial $E \times B$ velocity for PPCD and standard discharge

Frequency spectra shown in Fig. 4.3 clearly demonstrate what factors contribute to suppression of particle transport in PPCD at $r/a \geq 0.96$. The flux reduction arises mainly from the combined decreases of the density, potential fluctuation amplitudes, and the transverse wave number (the electric field comes from the combination of the potential fluctuation and transverse wave number $\vec{E}_r = -\nabla\bar{\phi} = -ik_r\bar{\phi}$), whereas the coherence reduction is small and the phase shows little change. Frequency spectra shown in Fig. 4.4 (measured at $r/a \sim 0.90$) demonstrate what factors contribute to the sharp increase in electrostatic particle

flux with decrease in minor radius. The combined increase of the coherence and phase, plus the larger electric field fluctuations, result in slightly larger particle flux even though the density fluctuation is greatly reduced. The larger electric field comes from the great increase of transverse wavenumber.

Paying more attention to Fig. 4.4 (c) and 4.3 (c), more potential fluctuation power with shorter wavelength [larger wavenumber in Fig. 4.4 (d)] at $f \sim 30 - 50$ kHz seems to be driven by PPCD only at $r/a = 0.90$. A consistent observation is shown in the frequency-wavenumber spectra, Fig. 4.9 (b), where a broader spectrum in wavenumber is demonstrated. It is possible that this driven turbulence in PPCD locally enhances the outward particle flux.

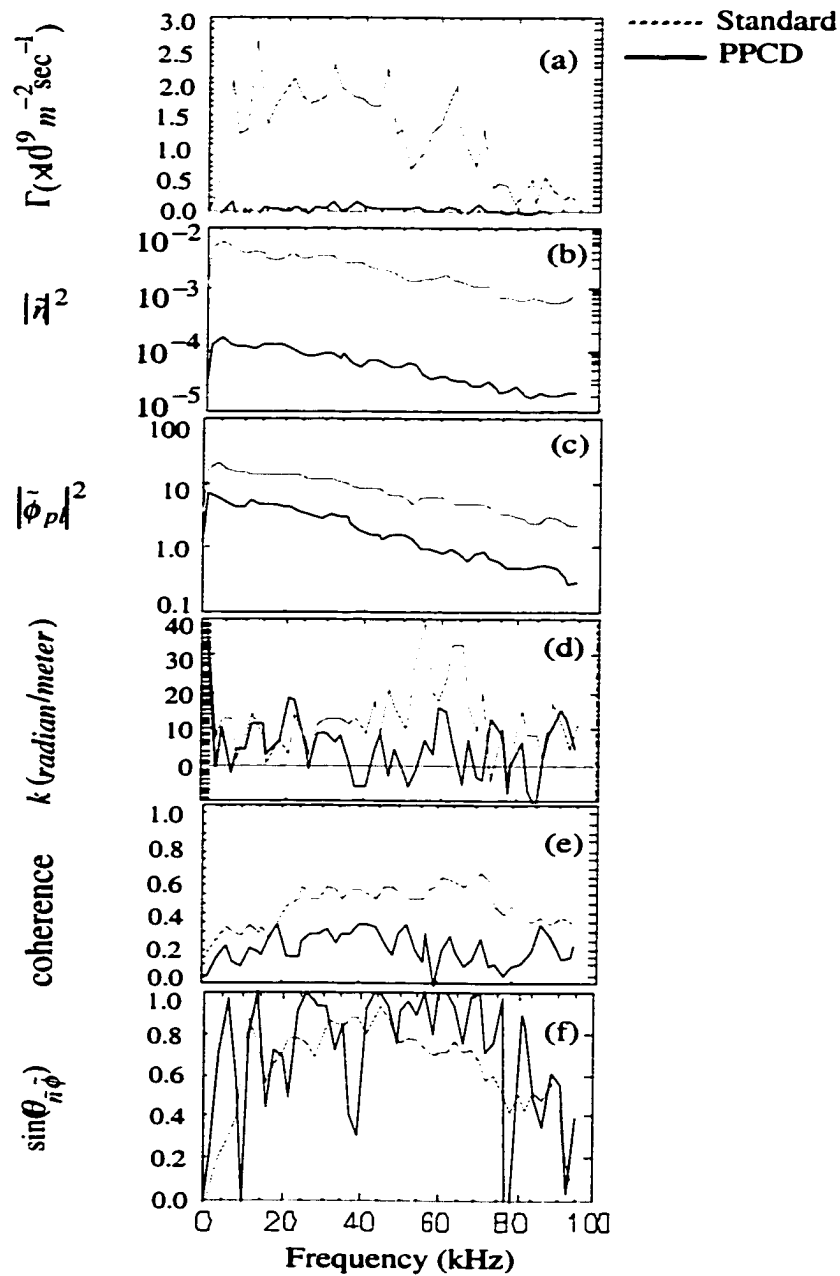


Fig. 4.3 Frequency spectrum of (a) electrostatic particle flux, (b) density fluctuations, (c) potential fluctuations, (d) potential wavenumber, (e) coherence between \bar{n} and $\bar{\phi}_{pl}$, and (f) $\sin(\theta_{\bar{n}\bar{\phi}})$ at $r/a \sim 0.96$ for standard and PPCD discharge

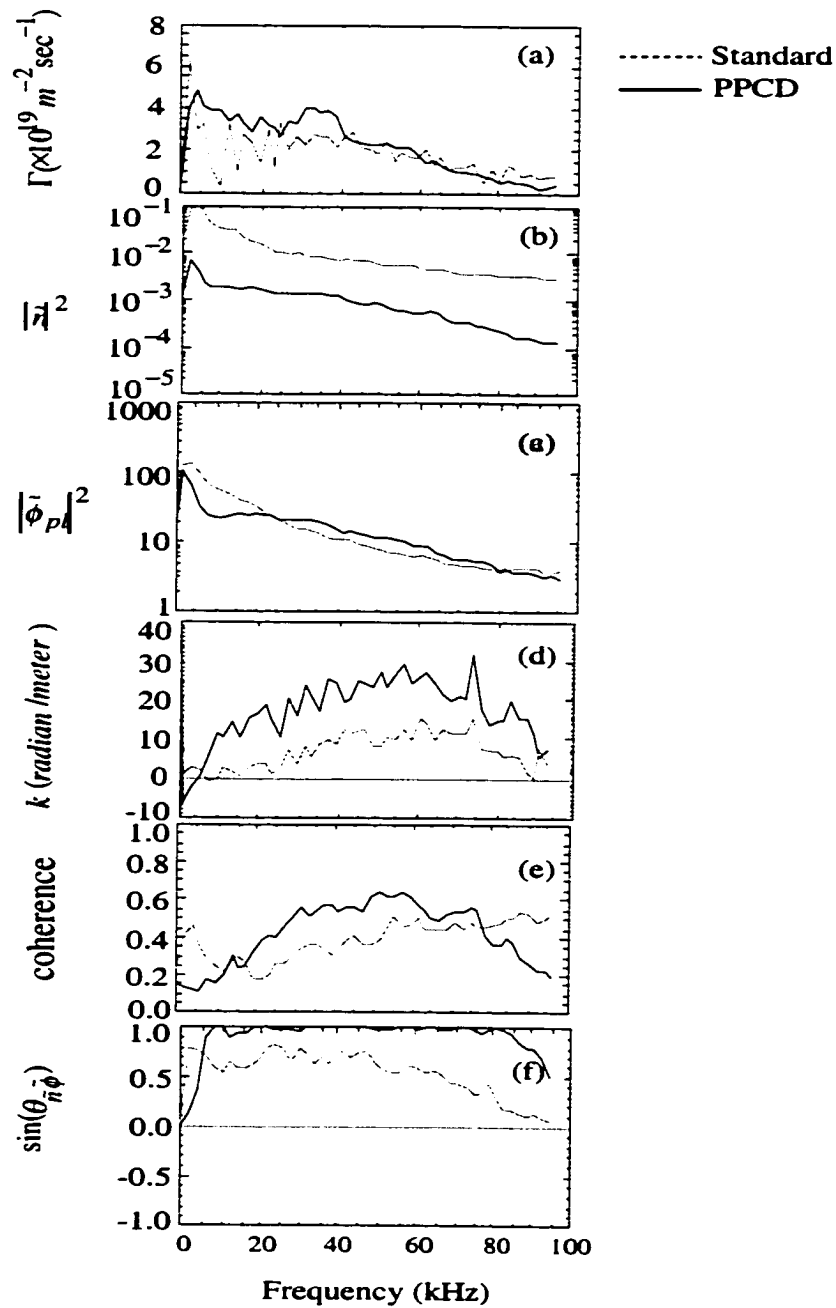


Fig. 4.4 Frequency spectrum of (a) electrostatic particle flux, (b) density fluctuations, (c) potential fluctuations, (d) potential wavenumber, (e) coherence between \tilde{n} and $\tilde{\phi}_{pl}$, and (f) $\sin(\theta_{\tilde{n}\tilde{\phi}})$ at $r/a \sim 0.90$ for standard and PPCD discharge

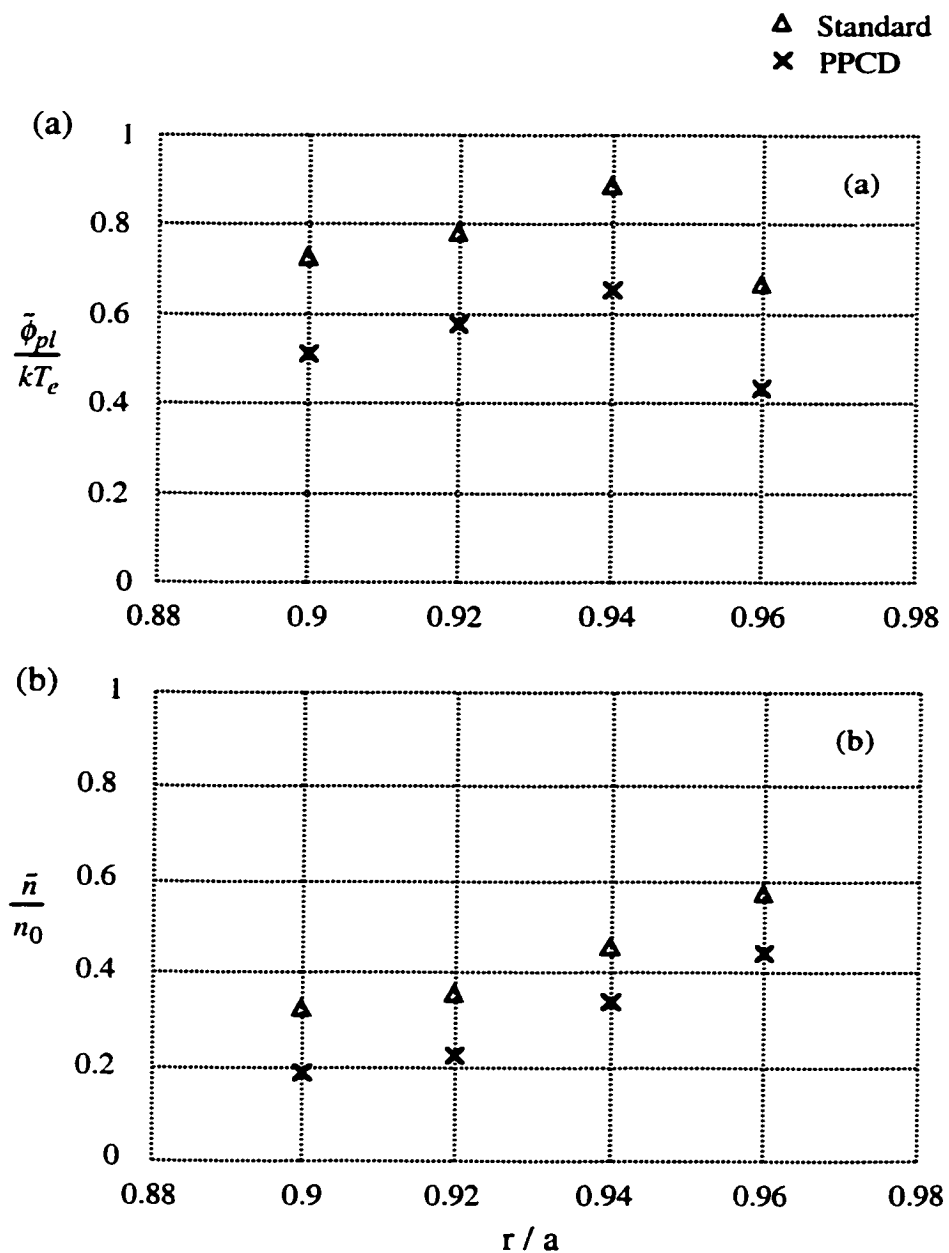


Fig. 4.5 Profile of (a) normalized potential fluctuations and (b) normalized density fluctuations

Fig. 4.5 shows the normalized fluctuation profile of density and plasma potential for standard and PPCD discharges. The shapes of the profiles are not changed due to current profile control. Generally the normalized potential fluctuations exceed the normalized density fluctuations, i.e., $\tilde{\phi}_{pl}/kT_e > \tilde{n}/n_0$, for all locations of $r/a \geq 0.9$. Observations in a tokamak device (TEXT) [8] and another RFP device (ZT-40) [9] show similar results. No significant change of the departure from $\tilde{\phi}_{pl}/kT_e = \tilde{n}/n_0$ is observed due to PPCD discharge.

Plasma biasing decreases outward particle flux more significantly. Shown in Fig. 4.6 is the edge profile of particle transport, density fluctuations and electric fluctuations. Unlike the edge profile of PPCD, no cross point is observed in the Fig. 4.6. Great suppression of particle flux and electric field fluctuation are observed at the entire $r/a > 0.90$ (decrease at least by a factor of three and four respectively), whereas the density fluctuations increase by a factor of 50% ~ 100%, depending on the minor radius. However the normalized density fluctuation in plasma biasing remains almost the same because of the local increase of the average density. Frequency spectra shown in Fig. 4.7 reveal how the particle transport is suppressed by plasma biasing. The flux reduction arises from the reductions of potential fluctuation amplitude, transverse wavenumber (both combined into the fluctuation reduction in electric field), and phase, while the

effect coming from the coherence is small, and the density fluctuation level shows an increase. The significant alteration of the phase may be attributed to the plasma flow induced by the biasing electrodes that imposes the radial electric fields. A qualitative consistency can be found in the increased gradient of the plasma potential due to the plasma biasing (Fig. 4.18 (d)). The changes of $E \times B$ flow and the flow shear due to plasma biasing will be discussed in section 4.2.

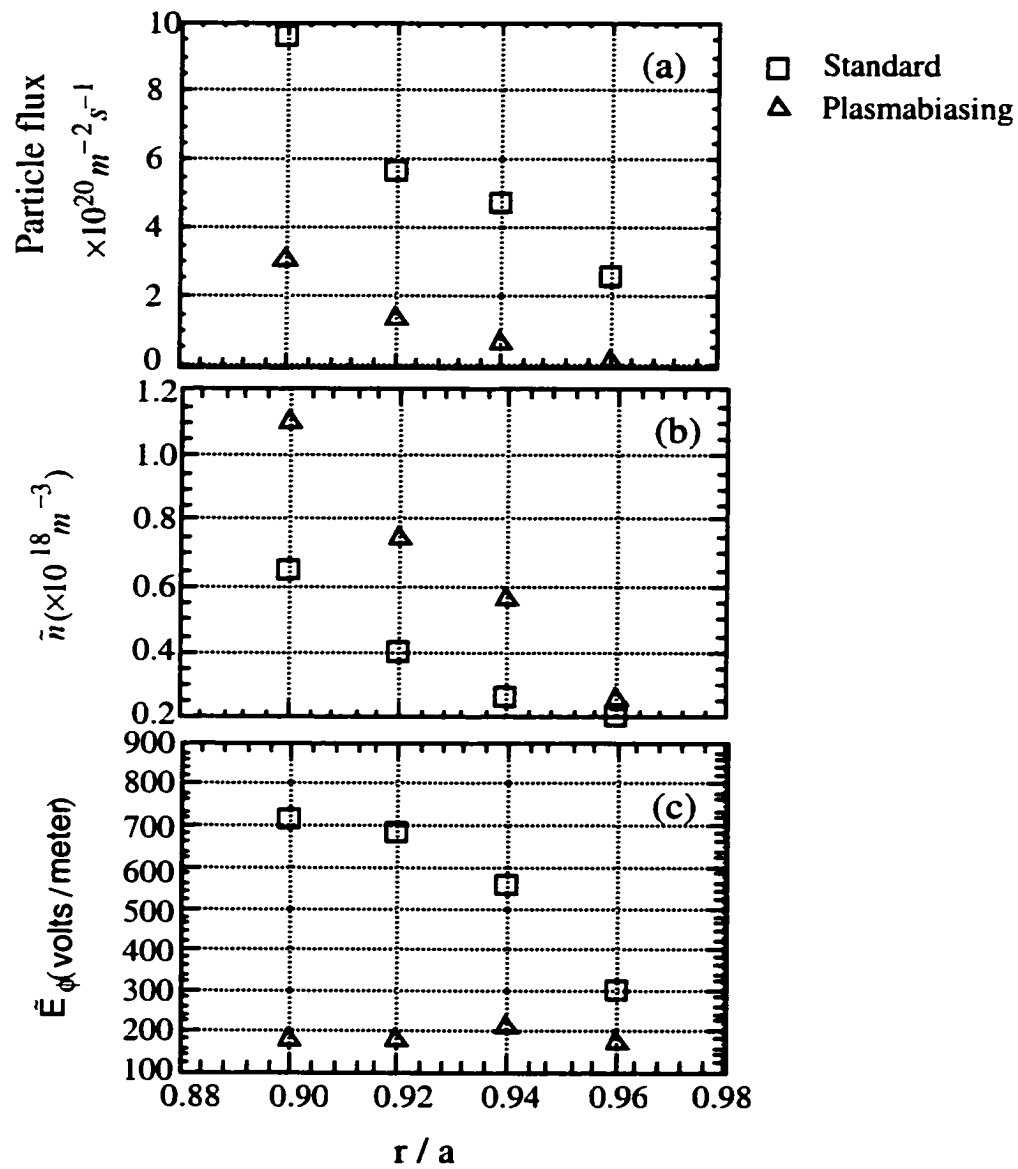


Fig. 4.6 Edge profile of (a) electrostatic particle transport, (b) density fluctuations, and (c) electric field fluctuations for standard and biased discharge.

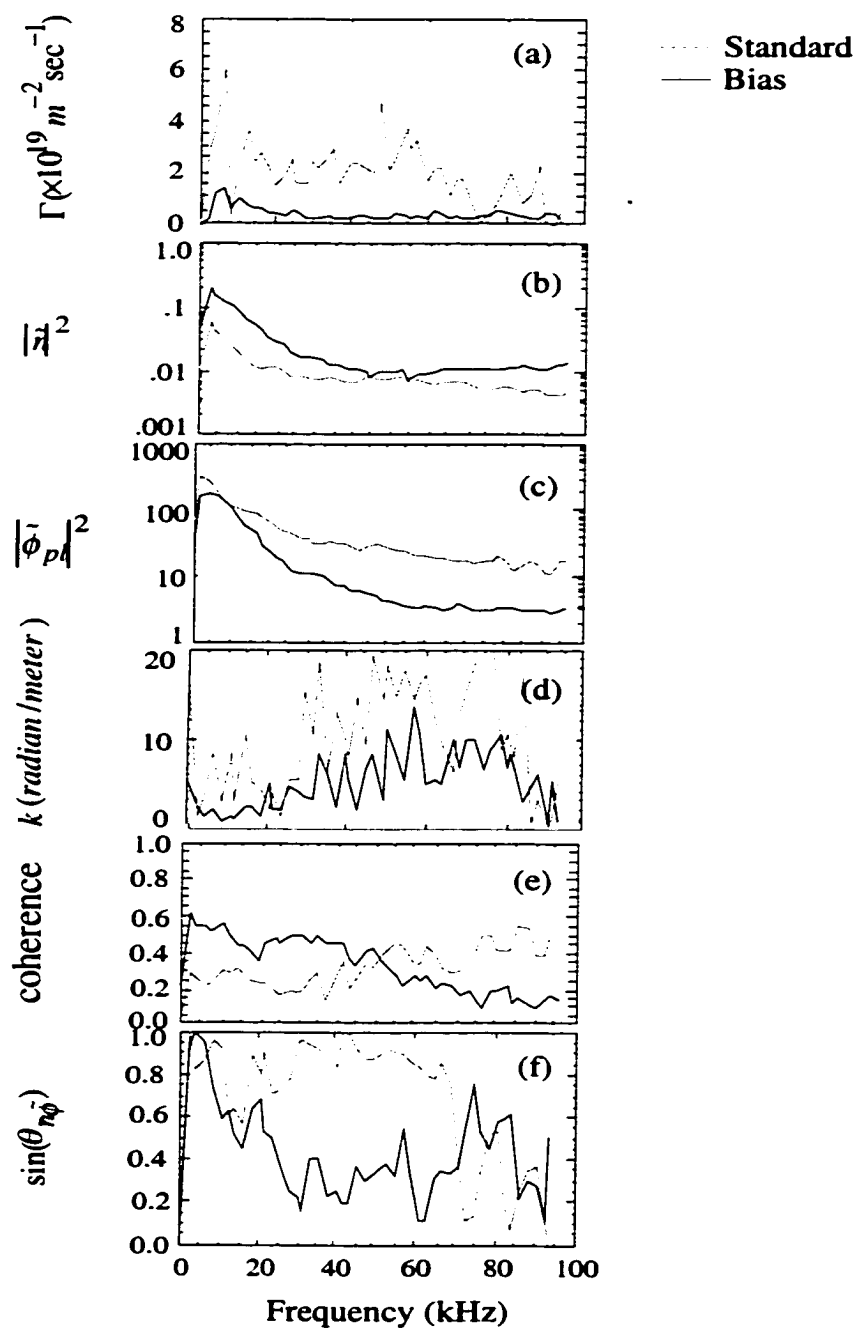


Fig. 4.7 Frequency spectrum of electrostatic fluctuations at $r/a \sim 0.90$ for plasma biasing

The particle transport driven by electrostatic fluctuations is broad band in standard discharges, spanning frequencies from 1 to 100kHz. No apparent peak is observed in the flux spectrum (contrary to the magnetic fluctuation spectrum which is peaked at around 10 ~ 20kHz). The electrostatic fluctuation power spectrum is also broadband and turbulent. Typical power spectra, shown in Fig. 4.3 and Fig. 4.7 fall monotonically with frequency. Similar results are observed in PPCD and plasma biasing. Spectra for both types of improved confinement discharges do not peak in any frequency, unlike the characteristics of magnetic fluctuation spectrum.

4.2 Modenumber-frequency spectrum and plasma rotation

Methods to derive wavenumber-frequency spectra have been discussed in the previous chapter. The wave number may be converted to toroidal or poloidal mode numbers with $n = k_\phi R$ and $m = k_\theta r$, where ϕ and θ represent toroidal and poloidal direction, and R and r represent major and minor radius of MST. In this section, I would like to present and discuss the responses of fluctuation propagation and mode spectrum width due to PPCD and plasma biasing.

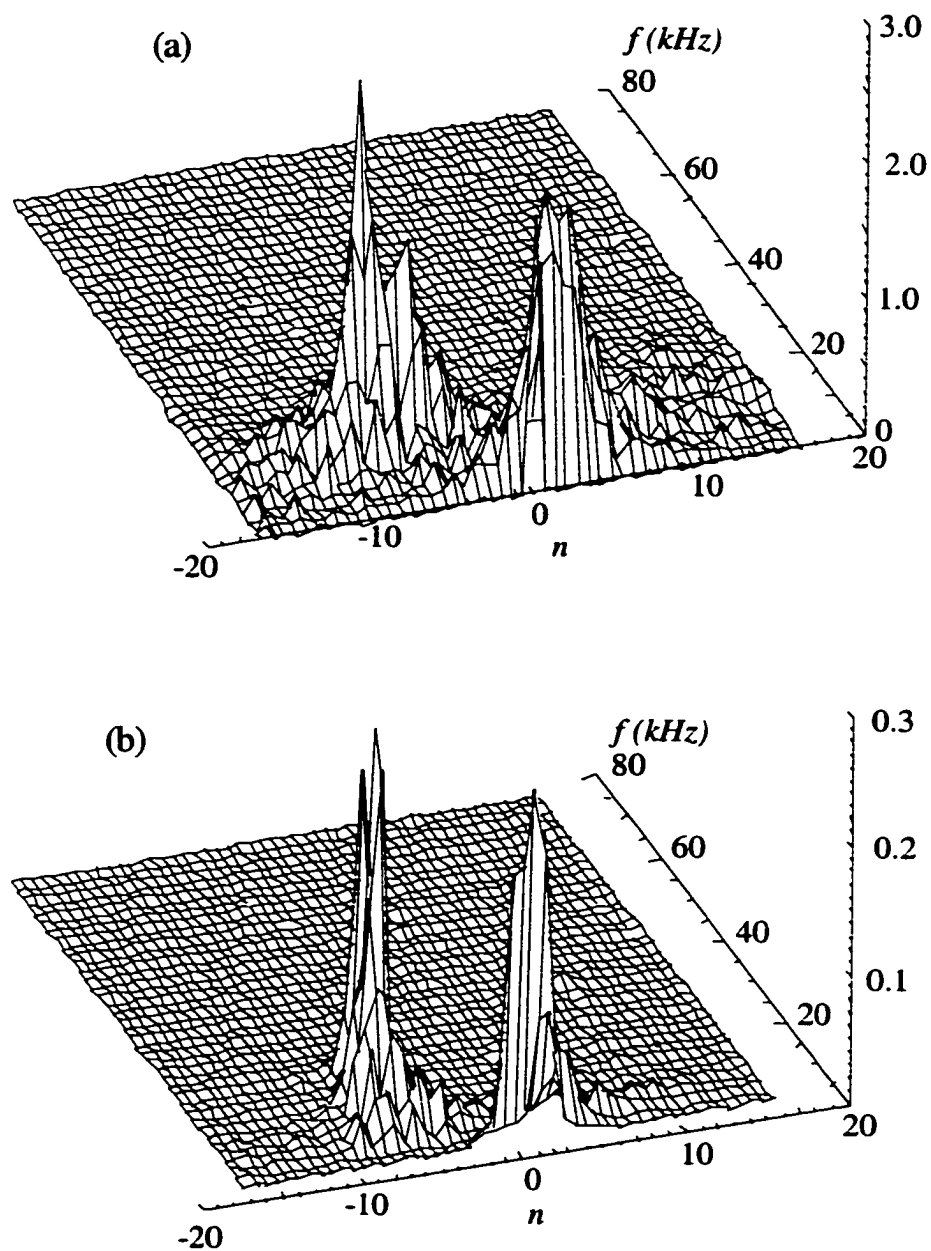


Fig. 4.8 Modenumber-frequency spectrum of \tilde{B}_r for (a) standard discharge and (b) PPCD discharge

4.2.1 Mode spectra and propagation in PPCD

Figure 4.8 shows fluctuation spectra of toroidal magnetic field for standard and PPCD discharges. Two peaks with comparable amplitudes are clearly seen in the spectra of standard discharge. One of the peaks centered around $n \sim 2R/r \sim 6$ is the expected dominant magnetic mode, while the other one peaks around $n = -1$. Measurements in other experiment show that the dominant $n \sim 6$ magnetic mode corresponds to $m = 1$ [11] and the $n \sim -1$ mode corresponds to $m = 0$ [12] that is resonant at the reversal surface. The opposite sign in n of each peak indicates that the $m = 1$ mode propagates toroidally in the opposite direction from the $m = 0$ mode. The $m = 1$ mode peaks at ~ 20 kHz, while the peak of $m = 0$ mode is located at lower frequency. This may be due to the longer wavelength (lower n) or slower rotation of $m = 0$ mode.

In the case of PPCD (shown in Fig. 4.8), no peak shift is observed, i.e. the $m = 1$ mode propagation remains in the same direction since PPCD does not alter significantly the plasma rotation. However significant changes of mode spectrum feature are clearly observed. First, spectrum broadness in toroidal mode number n is significantly narrowed, i.e. the magnetic fluctuation power is focused upon fewer spatial Fourier components (or less fluctuation helicity). The fluctuation power ratio of $n = 6$ and $n = -1$ to their neighboring modes (i.e. $n = 5, 7, 8, 9$ for $n =$

6 and $n = -2, -3, -4$ for $n = -1$) become larger in PPCD. In other words, the fluctuation reduction in other modes is relatively larger than that of $n = 6$ and $n = 1$. Second, the fluctuation amplitude is strongly suppressed by about a factor of 3. This might provide a scenario of improved confinement as follows. The reduction of magnetic fluctuation results reduction of magnetic island overlapping, thus reducing the stochasticity of magnetic fluctuations, hence significantly improving the plasma confinement.

The responses of the electrostatic fluctuation spectrum driven by PPCD are different from the responses of magnetic fluctuations. The response of ion saturation and floating potential fluctuations are very similar. Only either of these two fluctuations is shown and discussed for the remainder of this thesis. Fig. 4.9 shows the floating potential spectrum for a PPCD discharge. Unlike magnetic fluctuations, there is no $n \sim 6$ peak in the electrostatic fluctuation spectrum. Most fluctuation power is focused around $n = 0$ at low frequency. The average toroidal n number at higher frequency falls at $\sim n = 10$. For the spectrum in poloidal mode number m , the dominating m in magnetic fluctuations is $m = 1$, while the electrostatic fluctuations are dominated by $m = 0$ at both low and high frequency (Fig. 4.10). There may be two explanations for the existence of n or $m = 0$ mode: First, the oppositely propagating fluctuations may form a standing wave. Since the two-point methods can not identify the phase difference for standing waves, it

only provides the results of the $n = 0$ or $m = 0$ mode. Second, nonlinear coupling between the modes with the same mode number forms the large $n = 0$ or $m = 0$ signal. If the second explanation is true, the measured average toroidal $n \sim 10$ and $m \sim 0$ at $f \sim 40 - 60\text{kHz}$ suggest that the modes dominating the electrostatic fluctuations are resonant at the reversal surface where the safety factor $q = mB_\phi/nB_\theta = 0$.

For the spectrum at higher frequency, the enhanced shift of mode number in PPCD indicates the lower phase velocity of the electrostatic fluctuations. By comparing Fig. 4.9 (a) and Fig. 4.9 (b), the spectrum broadening due to PPCD may be clearly identified (Δn increases from ~ 100 to ~ 200). As I have discussed in the previous section, some electrostatic fluctuations are possibly driven by PPCD, resulting larger outward particle flux.

As a summary of this section, since the characteristics of the magnetic and electrostatic fluctuations and their response due to PPCD are very different, we thus obtain another support for the statement which was made in the last section - the reduction in magnetic fluctuations and improvement of particle and energy confinement induced by the current profile control does not significantly impact the electrostatic fluctuations and transport.

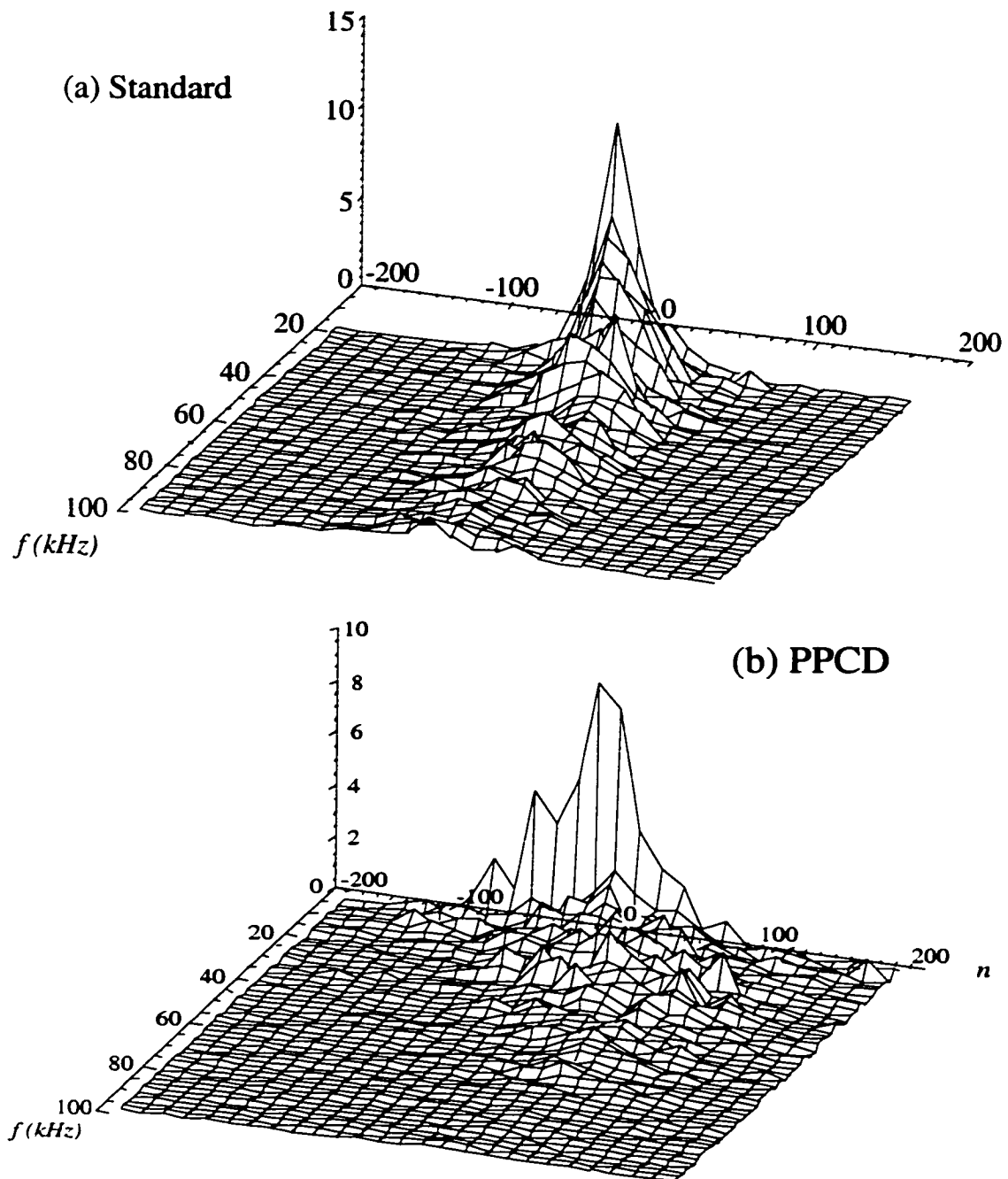


Fig. 4.9 Modenumber-frequency spectrum of potential fluctuations for (a) standard discharge, (b) PPCD

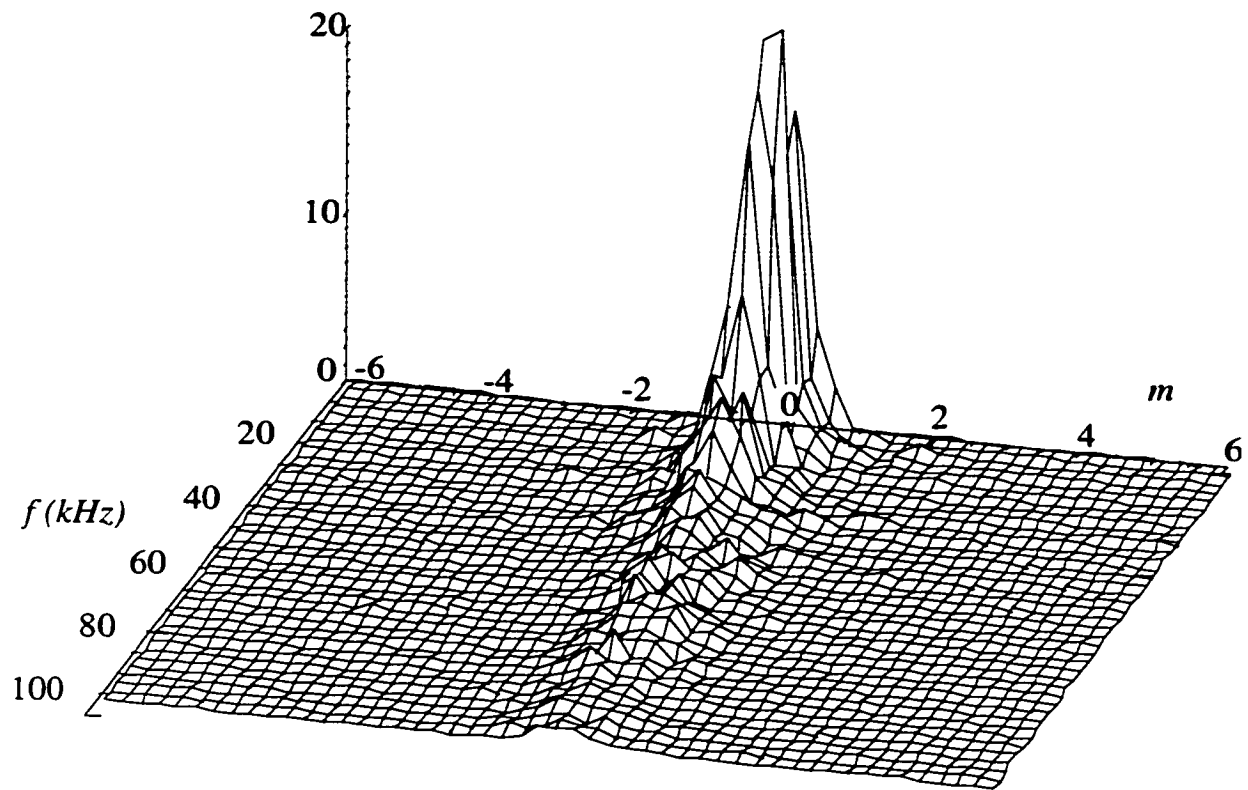


Fig. 4.10 poloidal mode number m spectrum of standard discharge

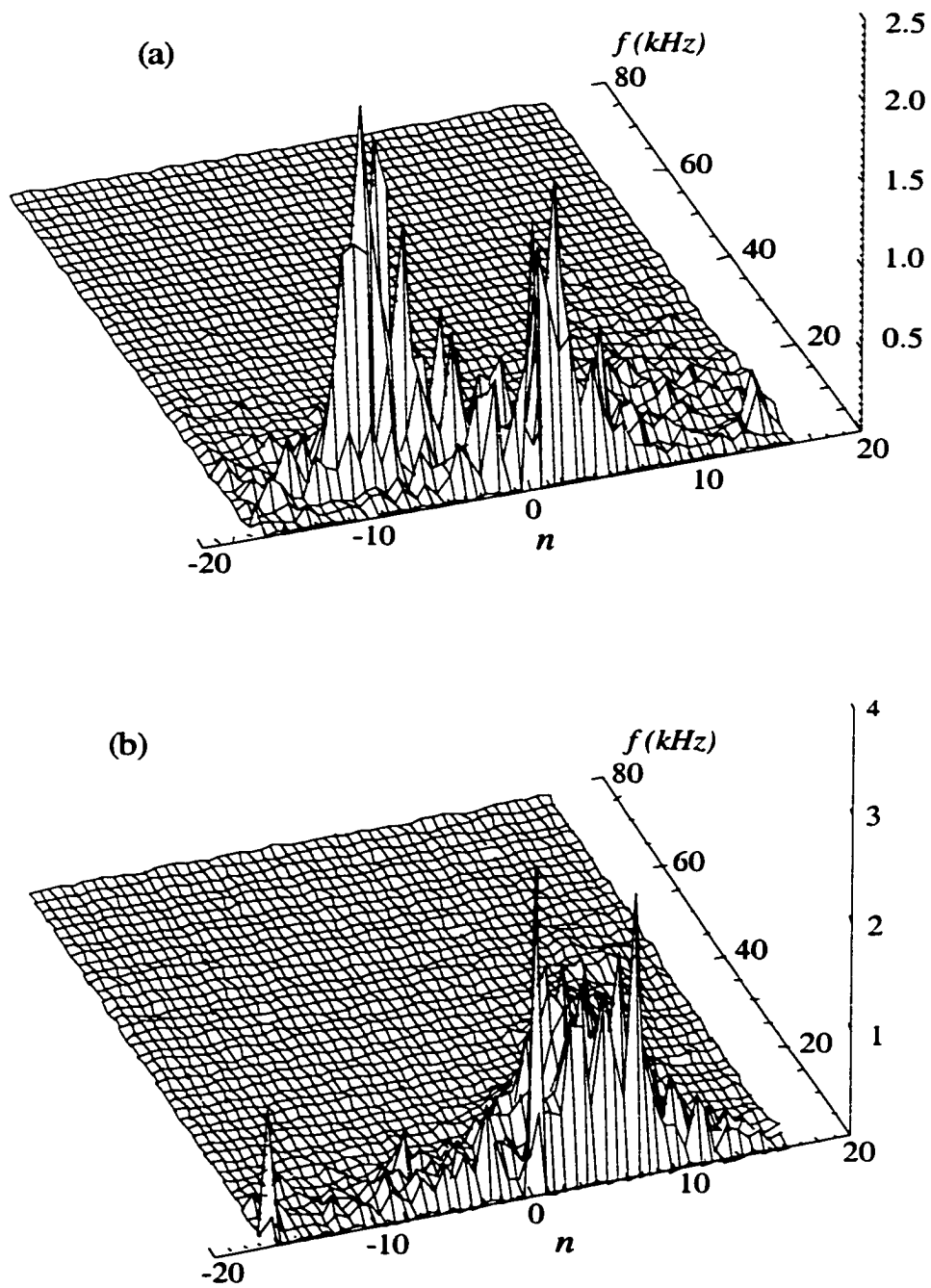


Fig. 4.11 Modenumber-frequency spectrum of \tilde{B} , for (a) standard discharge and, (b) plasma biasing

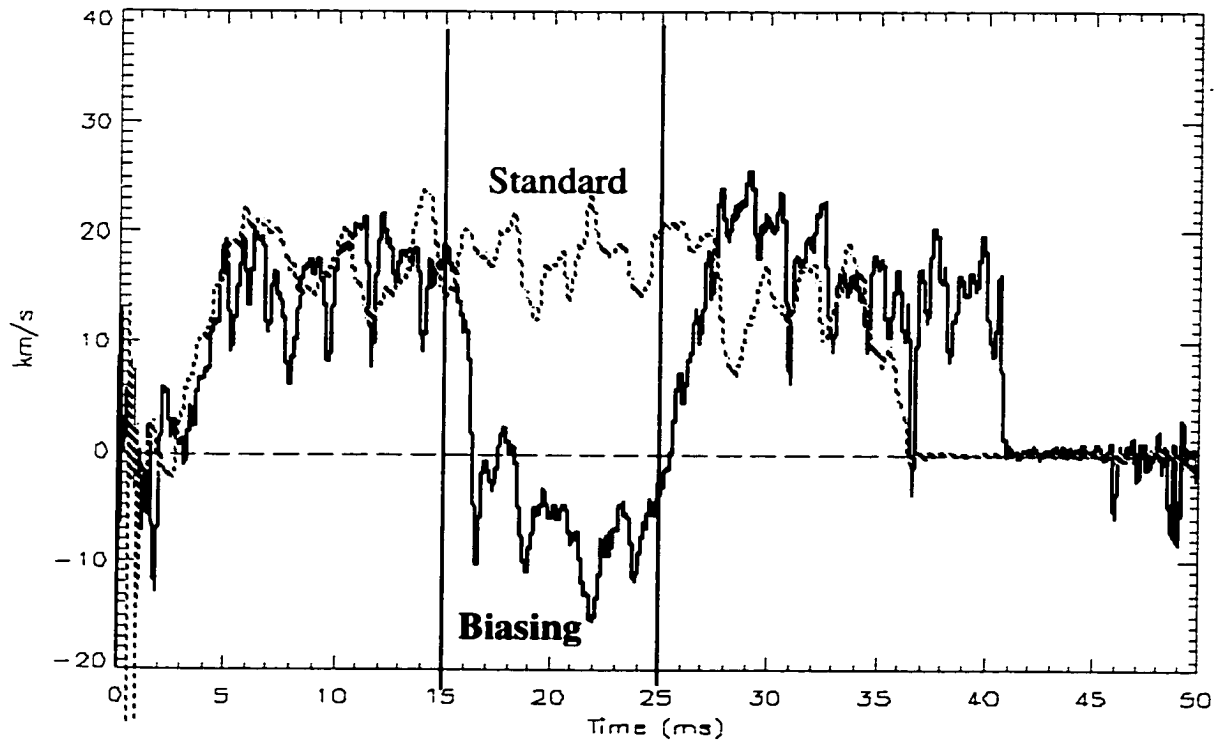


Fig. 4.12 Phase velocity of $n = 6$ magnetic perturbation for standard and biasing discharge

4.2.2 Mode spectra and propagation in plasma biasing

Fig. 4.11 shows the fluctuation spectra of toroidal magnetic fields for standard and biasing discharge. When plasma biasing is turned on, the $m = 1$ mode changes sign in n number, peaking around $n = -6$ at lower frequency. This change means that

the propagation of $m = 1$ magnetic perturbation is reversed and slowed down due to the $J \times B$ force induced by plasma biasing. The $m = 1$ mode then

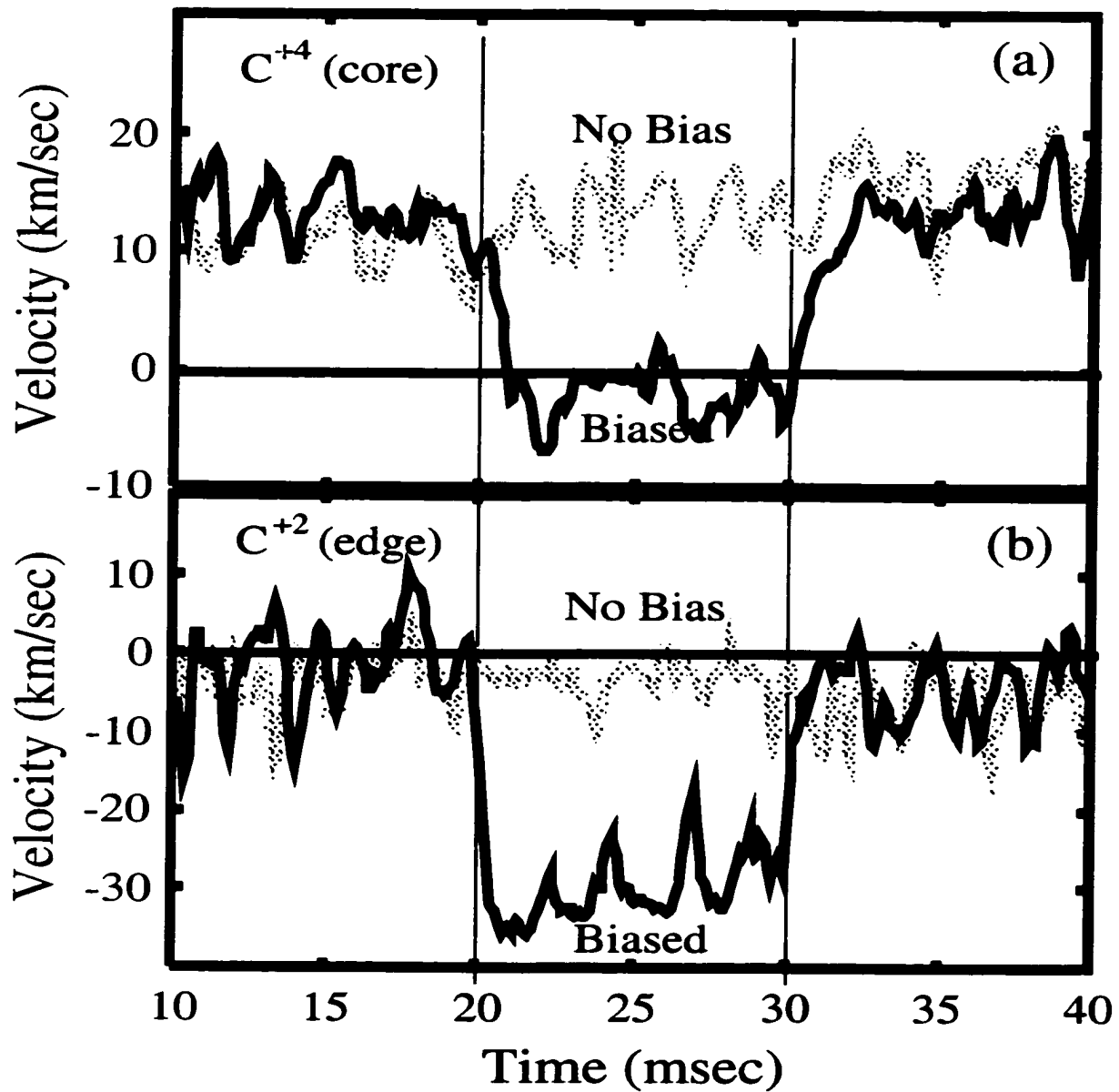


Fig. 4.13 Plasma Flow at (a) $r/a > 0.85$ (b) $r/a < 0.4$

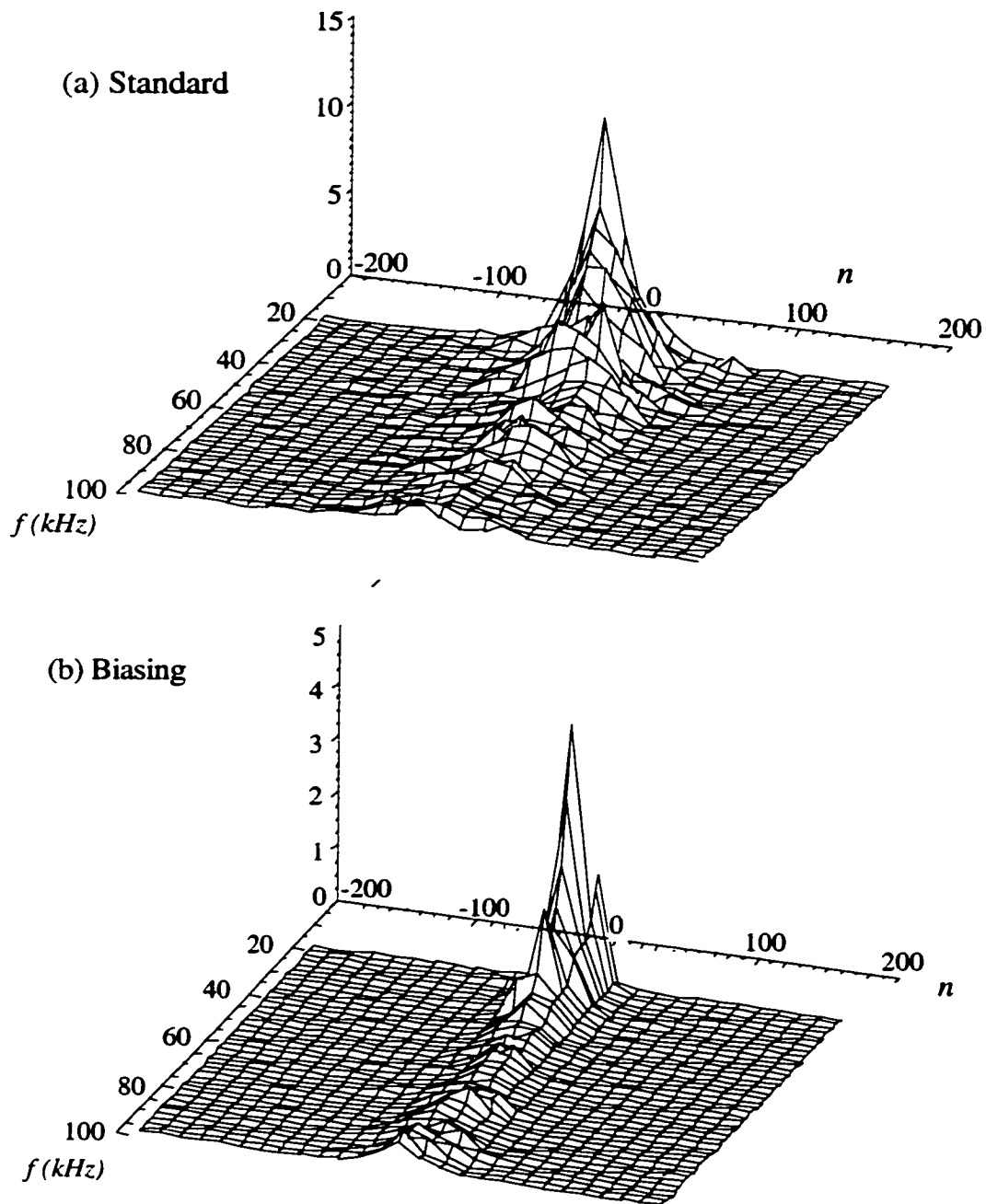


Fig. 4.14 Modenumber-frequency spectrum of potential fluctuations for (a) standard discharge, (b) plasma biasing

rotates in the same direction as the $m = 0$ mode. Analysis of phase velocity with mode analysis of spatial Fourier decomposition demonstrates consistent results (Shown in Fig. 4.12). Before biasing, the $n = 6$ mode rotates at phase velocity ~ 20 km/s. During biasing, the rotation responds quickly and move in the opposite direction with lower phase velocity. The plasma toroidal flow of the impurities is measured with a passive Doppler duo-spectrometer [10]. Doppler-shifted emission from C^{2+} ions in these plasmas is dominated by the flow of ions at $r/a < 0.4$. The evolution of plasma flow due to the plasma biasing is shown in Fig. 4.13 (a), The change of the mode rotation is qualitatively consistent with the change of the plasma rotation.

Using the dispersion relation of the edge electrostatic fluctuations in Fig. 4.7 (d) and the modenummer-frequency spectrum (Fig. 4.14), the change of the phase velocity of electrostatic fluctuations due to the plasma biasing can be identified. The electrostatic fluctuations in the MST edge propagate in the opposite direction to the core $n = 6$ magnetic mode rotation since the signs of the mode numbers are opposite. During biasing, the electrostatic fluctuations propagate in the same direction but rotate at higher phase velocity (increases from 25 km/s to 45 km/s). Figure 4.13 (b) shows the measurement of Doppler-shifted emission from C^{2+} which is dominated by the flow of ions at $r/a > 0.85$. The edge plasma

flow travels in the same direction as the edge electrostatic fluctuations. Changes of the edge $E \times B$ flow velocity and flow shear induced by plasma biasing evaluated with the measured plasma potential profile of Fig. 4.18 (d) are shown in Fig. 4.15. At $r/a = 0.90$, the $E \times B$ flow increases $\sim 50\%$ [from 40 km/s to 60 km/s at $r/a = .90$ in Fig. 4.15 (a)], and the flow shear doubles due to the effect of plasma biasing [Fig. 4.15 (b)]. Plasma biasing accelerates the edge plasma flow without flipping the flow direction, which is qualitatively consistent with the larger phase velocity of the electrostatic fluctuations and the $E \times B$ velocity.

The change of shearing rate due to plasma biasing can be calculated using the data of flow velocity gradient, wave number, radial correlation length, and the shearing rate equation derived by Biglari *et al.* [14],

$$\omega_s = k_{\perp} \Delta r_t \frac{dV_{E \times B}}{dr}$$

where k_{\perp} is the average transverse (to the edge magnetic field) wave number (Fig. 4.7 (d)), and Δr_t is the correlation length of the electrostatic fluctuations evaluated with the measurement of rake probes. No apparent change in the shearing rate is observed since the increases the $E \times B$ velocity gradient due to plasma biasing is canceled by the reduced k_{\perp} . This result may not be so surprising because the biasing electrodes are located at $r/a \sim 0.7$, while the measurement of the electrostatic probes shown in this thesis is carried out at $r/a \geq 0.9$. The biasing electrodes are too far away to provide the local effect to the shearing rate.

Unlike PPCD, the potential spectrum response due to plasma biasing becomes narrower and sharper ($\Delta\omega$ decreases from ~ 100 to ~ 50) (Fig. 4.14). Recall the response of magnetic fluctuation spectrum due to improved confinement discussed earlier. The change in magnetic fluctuations spectrum width is opposite to that of electrostatic fluctuation in both types of improved confinement discharges.

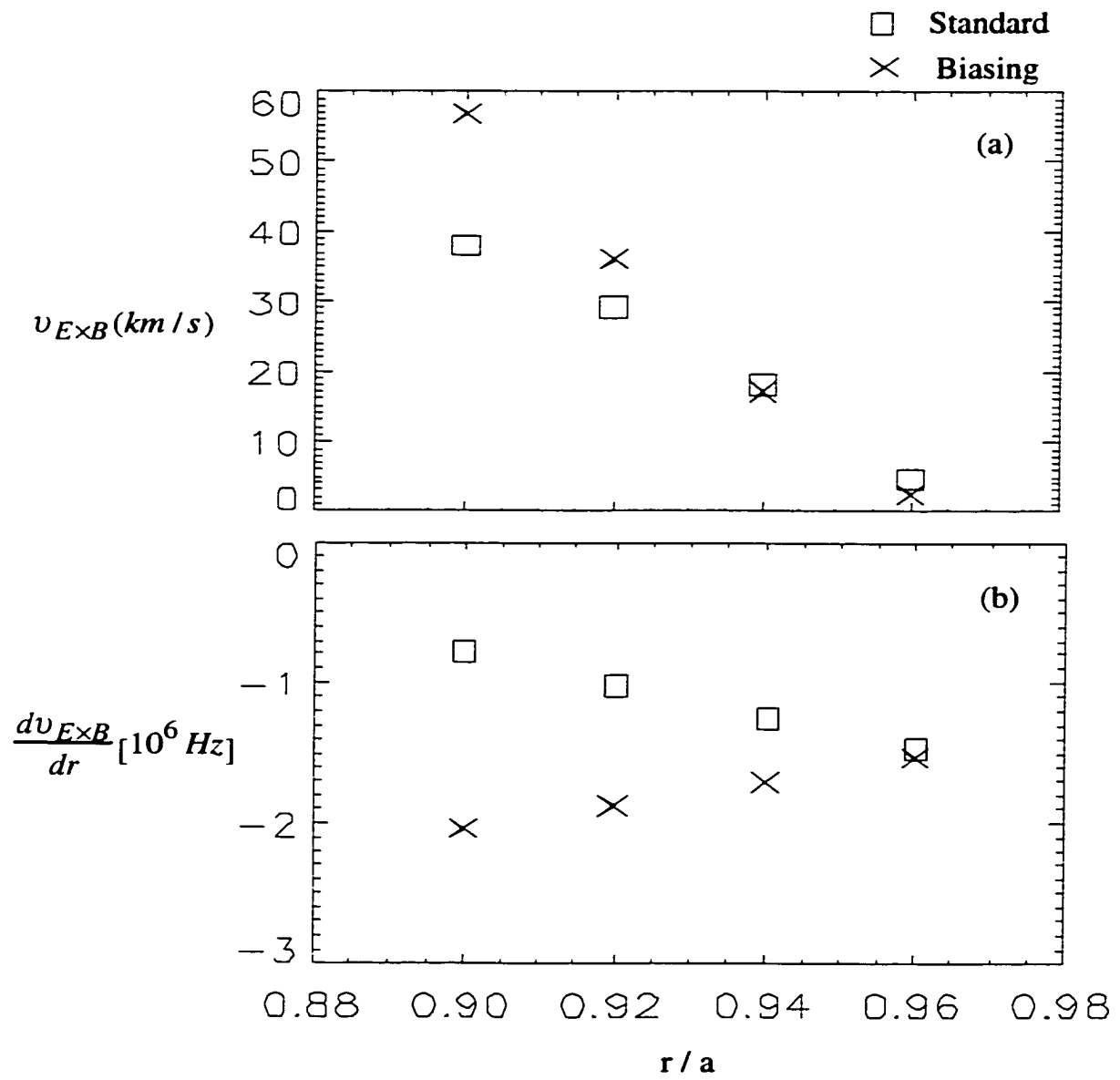


Fig. 4.15 (a) the edge $E \times B$ flow velocity and (b) the edge $E \times B$ flow shear for standard and biasing discharge

4.3 The $m = 0$, $n = 1$ fluctuations induced by plasma biasing

Another effect that is observed in plasma biasing, and not in PPCD is the excitation of low n modes of electrostatic fluctuations. This effect is clearly observed in Fig. 4.16, which shows the \bar{J}_{sat} spectrum measured with two probes separated toroidally with 30 degrees. The mode spectrum is wide and centered around $n = 0$ for standard discharge. With plasma biasing, all power in the negative side of n goes away, with a peak centered around $n = 1$ that dominates the fluctuation power. Comparing this \bar{J}_{sat} modenumber spectrum with the spectrum of magnetic fluctuations, the peaks of the $n = 1$ modes of both types of fluctuations are located in the same side of n axis, i.e. they propagate in the same direction. This low n mode electrostatic fluctuation at the edge of MST shows relatively high coherence with line-averaged FIR density fluctuations of the outermost chord, which is not observed in standard discharge [Fig. 4.17 (c)]. With the data of innermost chord FIR and core line-average CO₂ interferometer located toroidally 180 degree from FIR, this low frequency perturbation is identified as $m = 0$, $n = 1$ mode (Fig. 4.17 (a), 4.17(b)) which is resonant in the reversal surface. Although this large $m = 0$, $n = 1$ mode is excited by plasma biasing, it dose not produce large particle transport. Recall the discussion in last section [Fig. 4.7 (a)] that plasma biasing decreases the edge particle flux by a factor of larger than three.

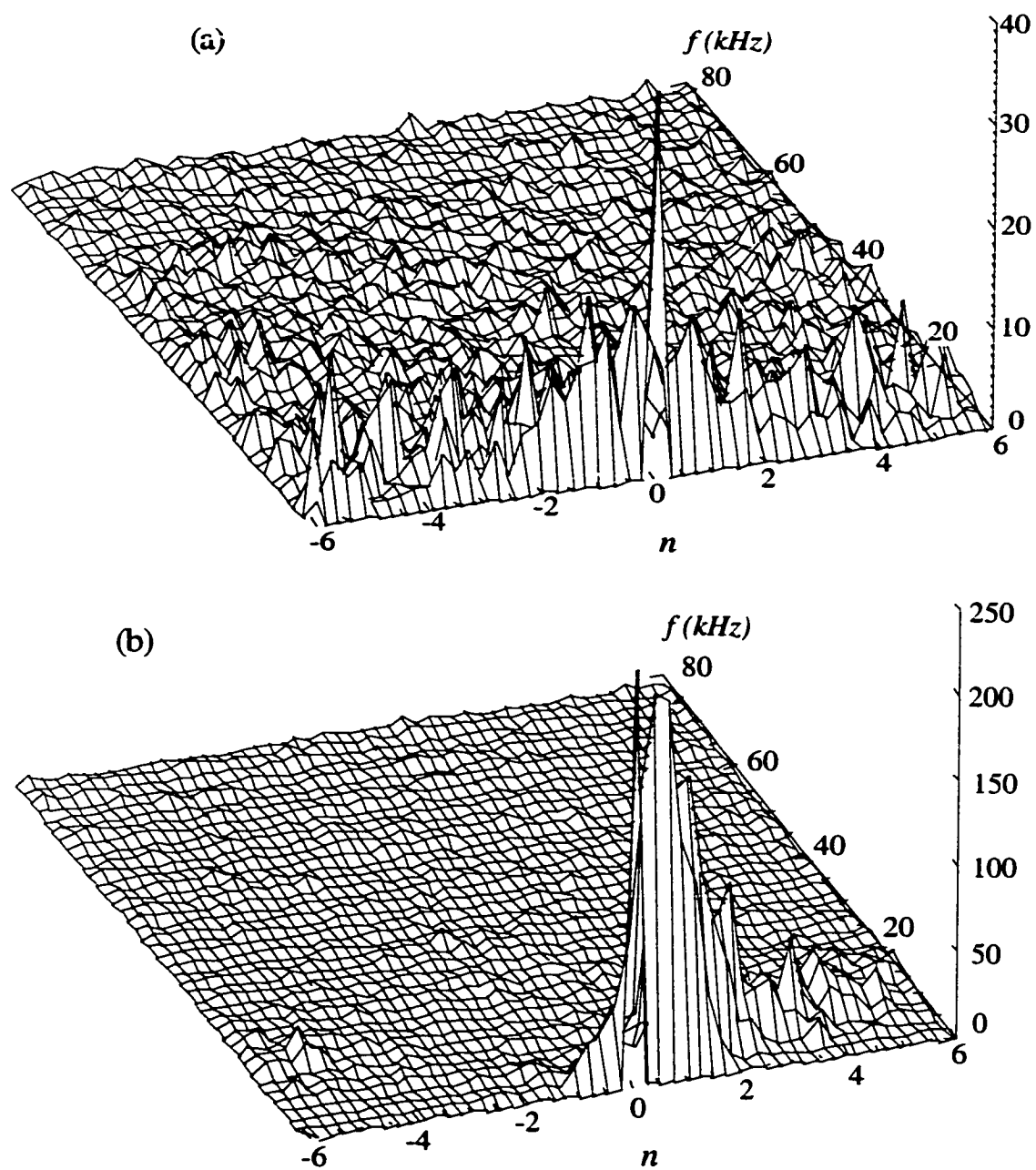


Fig. 4.16 Modenumber -frequency spectrum of ion saturation fluctuations (a) standard discharge, (b) plasma biasing

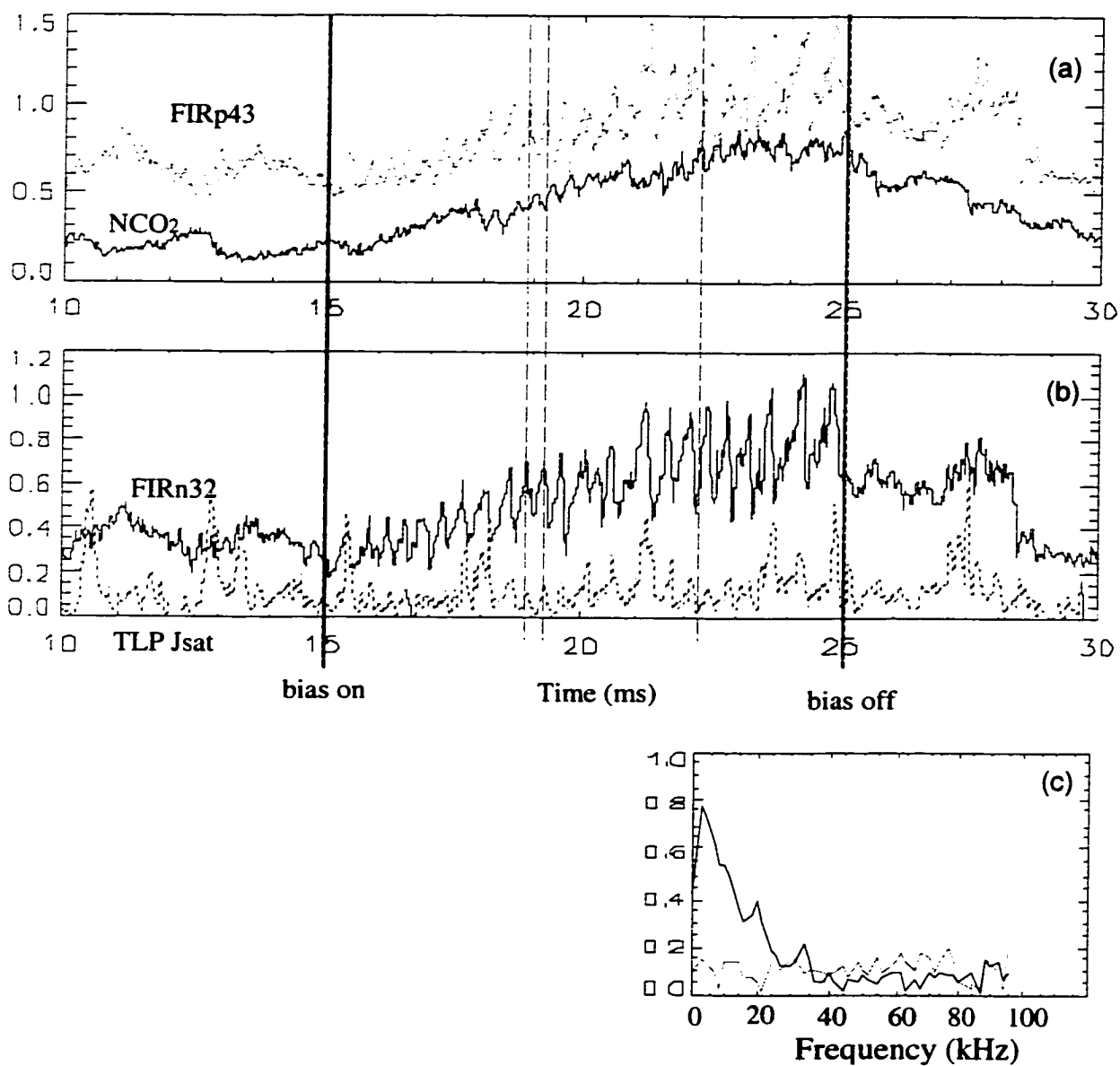


Fig. 4.17 (a) $m=0$, $n=1$ density fluctuations of (a) outermost chord FIR and CO₂, (b) innermost chord FIR and triple probe (c) coherence of FIRp43 and triple probe

4.4 Edge equilibrium profile of improved confinement

The equilibrium quantities have also been measured in the plasma edge. In Fig. 4.18, I show the edge profile of plasma density, electron temperature, and plasma potential. The electron temperature decreases in both types of improved confinement discharges [Fig. 4.18 (a), (b)]. In PPCD, the temperature change corresponds to a steepening of the overall profile. In biased plasmas both the temperature and its gradient decrease. The reduction of the edge temperature in PPCD may arise from the diminished energy transport associated with the improved energy confinement. The cause of decreased edge temperature in plasma biasing may be related to the increase of edge plasma density, which may be induced by the probe cooling effect.

Responses of the plasma potential profile induced by PPCD and plasma biasing are also different. An increased plasma potential gradient is observed in plasma biasing, while PPCD discharges exhibit flattened potential profile [Fig. 4.18 (c) and 4.18 (d)]. Changes of potential gradient (radial electric field, i.e. $E \times B$ drift velocity) and phase velocity inferred with the potential dispersion relation (wavenumber spectrum in Figs. 4.3 and 4.7) are qualitatively consistent in both types of discharges. Increased phase velocity due to plasma biasing implies a

steepened potential profile. Similarly in the case of PPCD (for $r/a < 0.92$), decreased potential gradient slows down the phase velocity.

The diffusion coefficient due to the electrostatic particle transport may be derived by Fick's law ($D = \Gamma^p / |dn/dr|$) using the measured density gradient and electrostatic particle flux. Both density and density gradient decrease in PPCD. Interestingly the diffusion coefficient inferred with Fick's law doubles in PPCD compared with standard discharge. PPCD actually degrades the particle diffusion at the edge even though the global confinement is improved. This surprising result comes from the largely decreased plasma edge density and density gradient. In plasma biasing, the outward particle flux is reduced all over the plasma edge ($r/a \geq 0.88$). Unlike PPCD, the density and density gradient at the edge increase. These two effects result in a smaller diffusion coefficient (Fig. 4.19). Plasma biasing decreases the edge particle diffusion.

Table 4.1 summarizes the edge plasma behavior responses due to PPCD and plasma basing.

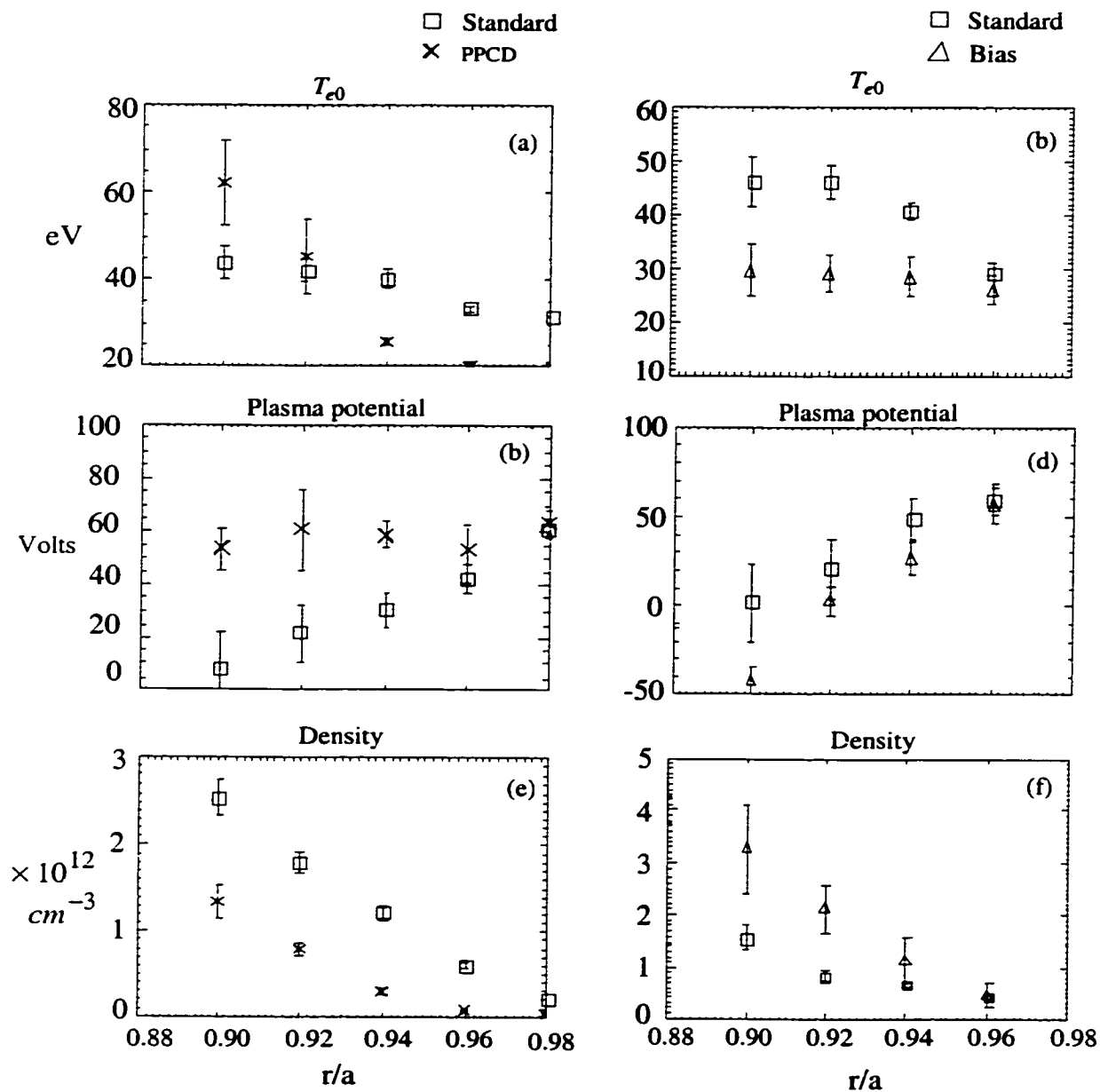


Fig. 4.18 Equilibrium profile of the edge plasmas (a), (c), and (e) for standard and PPCD, (b), (d), and (f) for standard and biasing

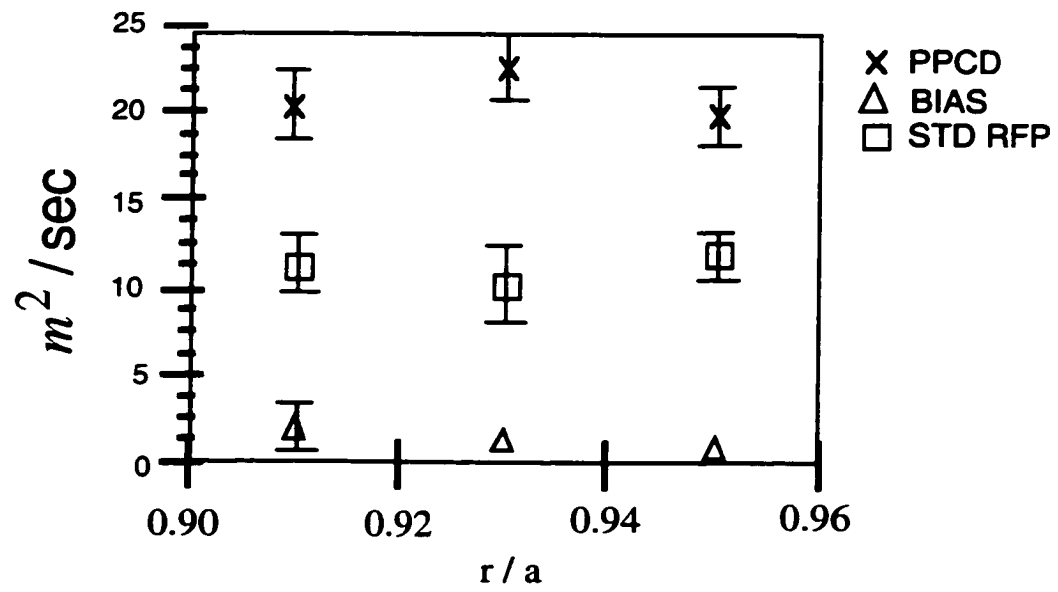


Fig. 4.19 Diffusion coefficient due to the electrostatic transport

Table 4.1 Response of plasma behavior due to 2 types of improved confinement

DISCHARGE TYPE	PPCD	PLASMA BIASING
Particle flux	Decrease only at $r/a > 0.94$	Decrease
$ \bar{n} $	decrease	Increase
$ \bar{E}_\phi $	Decrease only at $r/a > 0.94$	Decrease
Phase	No change	Decrease
Coherence	decrease	No change
Density gradient	decrease	Increase
Diffusion coefficient	increase	Decrease
Magnetic fluctuations	decrease	No change
Propagation of edge electrostatic fluctuations	decelerated	Accelerated
Propagation of $m = 1$ magnetic mode	No change	Reversed and decelerated
Propagation of $m = 0$ magnetic mode	No change	No much change
Mode-number spectrum in electrostatic fluctuations	broader	Narrower
Mode-number spectrum in magnetic fluctuations	narrower	No change or Broader

References

1. M. R. Stoneking *et al.*, Phys. Rev. Lett. **73**, 549 (1994)
2. G. Fiksel, S. C. Prager, W. Shen, and M. Stoneking, Phys. Rev. Lett. **72**, 1028 (1994)
3. T. D. Rempel *et al.*, Phys. Rev. Lett. **67**, 1438 (1991)
4. C. R. Sovinac, Ph.D. Thesis, University of Wisconsin - Madison, (1995)
5. M. R. Stoneknig *et al.*, Phys. Plasmas **4**, 1632 (1997)
6. N. Lanier, Ph.D. Thesis, University of Wisconsin - Madison, (2000)
7. D. Craig, Ph.D. thesis, University of Wisconsin - Madison, (1998)
8. A. J. Wooten *et al.* Phys. Fluids B **2**, 2879 (1990)
9. H. Y. W. Tsui *et al.*, Nuclear Fusion **31**, 2371 (1991)
10. D. Craig *et al.*, Phys. Rev. Lett. **79**, 1865 (1997)
11. W. Shen, R. N. Dexter, and S. C. Prager, Phys. Rev. Lett. **68**, 1319 (1992)
12. J. T. Chapman, Ph. D. Thesis, University of Wisconsin - Madison, (1998)
13. F. F. Chen, Plasma physics and controlled fusion Vol 1,
14. H. Biglari, P. H. Diamond, and P. W. Terry, Phys., fluids B **2**, 1 (1990)

Chapter V Summary and conclusion

Many important characteristics of the two types of improved confinement discharges - PPCD and plasma biasing - have been identified with edge probe measurement. The most important result of these studies is that the reduction of electrostatic particle transport in plasma biasing is more significant than that in PPCD. For plasma biasing, marked reduction of the electrostatic particle transport is observed at the entire edge region ($r/a \geq 0.90$), whereas PPCD decreases particle transport only at the outermost 4% of the plasmas, i.e., for $r/a \geq 0.96$.

5.1 Electrostatic transport in improved confinement

Transport over the bulk of the RFP is believed to be determined by magnetic fluctuations. PPCD is proposed to alter the current density profile so as to reduce the magnetic fluctuations. A marked improvement in global particle and energy confinement can be accomplished (up to a factor of eight and five) due to the great reduction of magnetic fluctuation driven transport. It is also known that electrostatic fluctuations dominate particle transport in the edge region.; however the cause of electrostatic fluctuations remains unknown. Hence their behavior in improved confinement discharges induced by current profile control is difficult to anticipate. Probe measurement shows a sharp increase in the electrostatic particle flux with decrease in minor radius. Particle flux is reduced only at the extreme edge, i.e., for $r/a \geq 0.94$. The measurement with electrostatic probes suggests that the current profile control does not significantly impact the electrostatic transport even though global particle and energy confinement are significantly improved. On the other hand the reduced inward radial $E \times B$ velocity induced by PPCD does not provide support for the speculation of $E \times B$ plasma compression.

In plasmas with electrical biasing, a stronger response of the electrostatic transport is observed. Although the magnetic fluctuations and energy confinement

remain the same, and only modest improvement in global particle confinement (~50%) is achieved, electrostatic particle transport is markedly reduced by a factor of larger than three at the entire outermost 10% of the plasmas. The flux reduction arises from the effect of fluctuation reduction and phase alteration. If we assume that the flux is diffusive, then the reduction in the diffusion coefficient is even greater. Although the increase in the gradient of $E \times B$ velocity due to plasma biasing is observed at $r/a \geq 0.90$, the decreased transverse wavenumber cancels this effect so that the $E \times B$ shearing rate remains the same. This unexpected result may be due to the large radial separation between the biasing electrode and the electrostatic probes for particle transport measurement. Much stronger shearing rate is suspected to exist only at the radial location closer to the biasing electrodes.

5.2 Mode spectra and propagation of fluctuations

We have used the modenumber-frequency spectra of fluctuations to study (1) the response of fluctuation propagation induced by the current profile control and plasma biasing; (2) the characteristics of magnetic and electrostatic fluctuations. The change of the propagation may be revealed with the location of the peak in the spectra. In standard discharges, the global $n \sim 6$ mode and $n \sim 1$ modes of the magnetic fluctuations rotate in opposite directions. The edge

electrostatic fluctuations travel along with the local plasma flow, and opposite to the $n \sim 6$ magnetic mode. The measurement of both the poloidal m and toroidal n modenumbers spectra suggest that the electrostatic fluctuations are resonant at the reversal surface.

In PPCD, the propagation of global magnetic and local electrostatic fluctuations remains mostly the same since PPCD does not alter the plasma flow significantly. The mode number shift of the electrostatic fluctuations induced by PPCD shows possible decelerated propagation. The propagation deceleration shows the consistency with the reduced local electric field deduced from the flattened plasma potential profile in the discharge of PPCD. The different characteristics between magnetic and electrostatic fluctuations can be well identified by the location of the peak in mode number and frequency. The modenumbers-frequency spectra of electrostatic fluctuations is broadened due to PPCD, whereas the spectra breadth of magnetic fluctuations becomes smaller. The peaks at $n = 6$ and $n = 1$ in toroidal magnetic fluctuations do not appear in the spectra of electrostatic fluctuations. Hence the techniques which reduce magnetic fluctuations (such as current density profile control) may not directly reduce electrostatic transport.

A more significant effect of fluctuation propagation is observed in biased plasmas than in PPCD since the biasing imposes an external radial electric field and can induce significant local plasma flow. The sign change of the $n \sim 6$ peak in the magnetic spectrum during plasma biasing implies that the propagation of the global magnetic fluctuations is reversed by the $J \times B$ force. This reversed mode rotation shows a qualitative consistency with the response of the plasma flow measured with the duo-Doppler spectrometer. In the edge region, the local electrostatic fluctuations propagate with a higher phase velocity and remain in the same direction during the biasing. Similar the standard discharge case, the edge electrostatic fluctuations travel with the local plasma flow.

5.3 Equilibrium profile

The response of the edge equilibrium quantities also demonstrates significant differences between PPCD and plasma biasing. In PPCD, although the line-averaged density increases, decreased edge density and density gradient are observed at $r/a \geq 0.9$. Combining the density gradient with the measurement of the electrostatic particle flux profile, PPCD increases the diffusion coefficient. The profile of plasma potential in PPCD is flattened, implying that the effect of localized flow is suppressed. These results in the equilibrium profile are consistent

with the discussion mentioned above: current profile control and plasma biasing implement different effect in reduction of electrostatic particle flux.

In plasma biasing, increase of plasma density is a global effect for plasmas with biasing electrodes. Not only the line-averaged density increases, but also a significant increase in density and density gradient is observed at $r/a \geq 0.9$. The diffusion coefficient is strongly reduced in plasma biasing due to the enhanced density gradient. Larger gradient of plasma potential for plasma biasing indicates a larger localized $E \times B$ flow induced by the biasing electrodes.